EFFECTS OF ION IRRADIATION ON THE MICROSTRUCTURE AND MECHANICAL PROPERTIES OF TITANIUM-BASED METALLIC GLASSES

By

AREZOO ZARE

Bachelor of Materials Engineering
Imam Khomeini International University
Ghazvin, Iran
2005

Master of Materials Engineering
Sharif University of Technology
Tehran, Iran
2009

Submitted to the Faculty of the
Graduate College of the
Oklahoma State University
in partial fulfillment of
the requirements for
the Degree of
DOCTOR OF PHILOSOPHY
July, 2019

EFFECTS OF ION IRRADIATION ON THE
MICROSTRUCTURE AND MECHANICAL PROPERTIES OF
TITANIUM-BASED METALLIC GLASSES

Dissertation Approved:

Don A. Lucca

Dissertation Advisor

Sandip P. Harimkar

Shuodao Wang

Pankaj Sarin

ACKNOWLEDGMENTS

First and foremost, I would like to thank my advisor, Prof. Don A. Lucca, for his invaluable support and mentorship throughout the course of this study and many others. He has taught me how to think critically, research meticulously, write efficiently, and collaborate effectively. I would also like to thank my committee members, Prof. Sandip P. Harimkar, Prof. Shuodao Wang, and Prof. Pankaj Sarin for reading my dissertation and giving me valuable comments and suggestions. I would also like to extend my gratitude to Dr. Matthew J. Klopfstein for serving on my committee at some point and also for teaching me everything I know about nanoindentation experiments.

The assistance and support of Prof. Lin Shao of Texas A&M University and Prof. Guoqiang Xie of Tohoku University in conducting ion irradiation experiments and fabricating the metallic glass specimens are gratefully acknowledged.

I am also grateful to all my current and former colleagues in the Ultraprecision Surfaces Group; particularly Dr. Seyyed Ali Shojaee who introduced me to the group in the first place, Dr. Tres Harriman who always helped me in my writing and discussion of results, and Dr. Yongli Qi who assisted me in troubleshooting nanoindentation and atomic force microscopy experiments.

This material is based upon work supported by the National Science Foundation under Grant numbers CMMI-1130606 and CMMI-1130589. Any opinions, findings, and conclusions or recommendations expressed in this material are those of the author and do not necessarily reflect the views of the National Science Foundation.

Last but not least, I would like to thank my life companion, Nima Taheri, for always standing by my side and encouraging me to be the best I can. I would also like to mention my canine companions, Roscoe and the late Zoe, for keeping me happy and sane over the years. Finally, I would like to dedicate this document to my parents Homa Jahangiry and Akbar Zare and my sister Armineh Zare for their unconditional love and support throughout my life. Without them it would have been impossible for me to follow my dream of becoming a materials scientist.

Acknowledgements reflect the views of the author and are not endorsed by committee members or Oklahoma State University.

Name: AREZOO ZARE

Date of Degree: JULY, 2019

Title of Study: EFFECTS OF ION IRRADIATION ON THE MICROSTRUCTURE AND MECHANICAL PROPERTIES OF TITANIUM-BASED METALLIC GLASSES

Major Field: MECHANICAL AND AEROSPACE ENGINEERING

Abstract: Metallic glass specimens with a nominal composition of $Ti_{40}Cu_{34-x}Pd_{14}Zr_{10}Sn_2Si_x$ (at.%), where x = 2, 3, and 5, were subjected to annealing and/or ion irradiation and their microstructure and mechanical properties were characterized by a combination of X-ray diffraction (XRD), transmission electron microscopy (TEM), nanoindentation, scanning probe microscopy (SPM), and atomic force microscopy (AFM). No evidence of crystallization was observed for the specimens that were annealed at temperatures below the glass transition temperature and those irradiated with 4 MeV Fe^{2+} ions at room temperature, regardless of the fluence used. Annealing at temperatures below the glass transition temperature resulted in an increase in hardness and higher plastic deformation energy values, which suggests a reduction in ductility. Conversely, ion irradiation at room temperature resulted in a reduction in reduced elastic modulus, hardness, and plastic deformation energy, which suggests an improvement in ductility. For the specimens irradiated with 3.5 MeV Cu^{2+} ions at elevated temperatures, it was found that there is a critical temperature below which the specimens remained amorphous. When ion irradiation was performed at temperatures higher than the critical temperature, the specimens crystallized to depths beyond the range of the implanted ions. This critical temperature was found to be equal to the glass transition temperature when ion beam heating was minimized. By subjecting a crystallized $Ti_{40}Cu_{31}Pd_{14}Zr_{10}Sn_2Si_3$ specimen to a second step irradiation with 3.5 MeV Cu^{2+} ions using a fluence of 1×10^{16} ions/cm^2 at room temperature a metallic glass-matrix composite containing discontinuous crystalline phases, 10 - 80 nm in diameter, was created. Formation of nanocrystals in the composite was seen to result in an increase in reduced elastic modulus and hardness, and to shift the deformation mechanism towards less shear localization and more homogenous plastic flow compared to the as-spun specimen. These observations confirm that formation of nanocrystals can promote initiation of a large number of shear bands and inhibit shear band propagation, which could lead to an improvement in ductility.

TABLE OF CONTENTS

Chapter **Page**

Chapter **Page**

Chapter **Page**

LIST OF TABLES

Table **Page**

LIST OF FIGURES

Figure **Page**

Figure **Page**

Figure **Page**

Figure **Page**

Figure **Page**

NOMENCLATURE

MG ..... Metallic glass

XRD ..... X-ray diffraction

TEM ..... Transmission electron microscopy

SPM ..... Scanning probe microscope

AFM ..... Atomic force microscope

BMG ..... Bulk metallic glass

ρ ..... Density

E ..... Elastic modulus

σ_y ..... Yield strength

T_g ..... Glass transition temperature

DRP ..... Dense random packing

STZ ..... Shear transformation zone

τ_y ..... Shear yield stress

σ_n ..... Stress normal to the shear displacement plane

bcc ..... Body centered cubic

R_p ..... Projected ion range

R_l ..... Lateral ion range

SRIM ..... Stopping and range of ions in matter

λ ..... Wavelength

2θ ..... Diffraction angle

FIB ..... Focused ion beam

F ..... Test force

h ..... Penetration depth/punch displacement

H ..... Hardness

c ..... Proportionality constant

h_p ..... Permanent penetration depth

h_{max} ..... Maximum penetration depth

S ..... Stiffness

E_r ..... Reduced elastic modulus

A_p ..... Projected area of the contact

ν ..... Poisson's ratio of specimen

E_i ..... Elastic modulus of indenter

ν_i ..... Poisson's ratio of indenter

F_{max} ..... Maximum force applied to the specimen

h_c ..... Contact depth

C_f ..... Load frame compliance

C_s ..... Compliance of specimen

R_i ..... Radius of indenter

PDE ..... Plastic deformation energy

W_p ..... Work done by indenter at initial displacement burst

V_p ..... Volume of material displaced during initial displacement burst

F_d ..... Force at initial displacement burst

Δh ..... Displacement of indenter during initial displacement burst

$h_{discrete}$ ..... Total amount of deformation that occurs during the displacement bursts

$\dot{\epsilon}$ ..... Indentation strain rate

t ..... Time

dpa ..... Displacements per atom

SAD ..... Selected area diffraction

fcc ..... Face centered cubic

EDS ..... Energy dispersive spectroscopy

ΔT_{max} ..... Maximum temperature rise

ϕ ..... Ion beam intensity

E ..... Ion beam energy

l ..... Width of the ion beam cross section

K ..... Thermal conductivity

AE ..... Acoustic emission

PAS ..... Positron annihilation spectroscopy

SEM ..... Scanning electron microscope

CHAPTER I

INTRODUCTION

1.1 Motivation for the Present Study

Metallic glasses (MGs) are a class of alloys that, unlike their conventional counterparts, do not exhibit long range atomic order [1–3]. Because of their amorphous structure, MGs do not possess crystalline defects (e.g., dislocations and grain boundaries) and exhibit desirable properties that make them suitable for a variety of applications. Among MG alloys, Ti-based MGs have recently received considerable attention because of their high specific strength, high elasticity, and superior wear and corrosion resistance. Such desirable properties make Ti-based MGs suitable for replacing conventional Ti alloys in aerospace applications [4–6]. Furthermore, Ti-based MGs that are free from non-biocompatible elements (e.g., Ni or Be) have the potential to be used for medical implants [6–12]. Similar to other types of MGs, the intrinsic low ductility of Ti-based MGs at room temperature limits their applications. In general, under uniaxial tension at room temperature, deformation of MGs is mostly elastic with limited macroscopic plastic strain followed by catastrophic failure [13, 14]. Rapid propagation of shear bands (regions of highly localized strain) under unconstrained conditions is the mechanism responsible for the abrupt brittle fracture of MGs [15, 16]. It has been demonstrated that shear band initiation and propagation in MGs can be influenced by the presence of discontinuous crystalline phases within the amorphous matrix [17]. Therefore, techniques such as controlled solidification, annealing, and ion irradiation may be used to modify the mechanical response of MGs by creating MG-matrix composites containing one or more discontinuous crystalline phases. Numerous reports on Ti-based MG-matrix composites created by *in situ* precipitation of crystalline phases (typically in the form of dendrites) during solidification [10,18–31] and annealing [6, 11, 32, 33] have appeared. However, investigations of such composites produced by ion irradiation

have been limited [34,35]. Additionally, details of the crystallization mechanisms and the subsequent effects on mechanical properties have remained poorly understood to this date.

1.2 Objectives

The present study is a part of a collaborative research project between Oklahoma State University (OSU) and Texas A&M University (TAMU), and has been supported by the National Science Foundation (NSF) through grant numbers CMMI-1130606 (OSU) and CMMI-1130589 (TAMU). The goal of this research is to shed light on the details of ion irradiation-induced crystallization in MGs and to investigate the changes in mechanical properties due to nanocrystal formation. The principal objectives of the study are to (1) determine the response of MGs to ion irradiation by investigating the microstructural evolution, (2) identify the details of the crystallization process, and (3) determine the influence of ion irradiation on mechanical properties by measuring and comparing the mechanical response of as-received and irradiated specimens.

A variety of characterization techniques has been utilized to achieve these objectives. In order to determine microstructural evolution after irradiation, X-ray diffraction (XRD) and transmission electron microscopy (TEM) have been used. Effects of ion irradiation on mechanical response have been studied by nanoindentation experiments using two indenter geometries: spherical and pyramidal with a triangular base (Berkovich). The spherical indenter is used to study serrated plastic flow during loading and evaluate the potential energy barrier for shear band initiation, and the Berkovich indenter is used to obtain elastic modulus and hardness. To better understand the deformation mechanisms and observe evidence of shear band activity after nanoindentation experiments, the area around the impressions made by the Berkovich indenter was studied by an *in situ* scanning probe microscope (SPM) and/or an ex situ atomic force microscope (AFM).

By providing a better understanding of the mechanisms responsible for crystallization and determining the effects of irradiation-induced crystallization on mechanical response, this study seeks to expand the application of MGs and provide a reliable method to produce ductile MGs specimens. Additionally, understanding the irradiation response of MGs is beneficial for developing materials that need to withstand irradiation under harsh conditions.

CHAPTER II

BACKGROUND

2.1 History and Development

Prior to 1960, except for thin films deposited at very low temperatures [36,37], there had been no reports on fabrication of metals or alloys in an amorphous state. The first MG was synthesized in 1960 by rapid quenching of a Au-Si alloy from ∼1300 °C to room temperature [38]. Since the synthesis of the first MG, there has been considerable effort to decrease the critical cooling rate required to bypass crystallization and thus increase the critical casting thickness/diameter of these materials [39]. In 1969, Chen and Turnbull developed MGs with thicknesses greater than 1 mm from Pd-Au-Si, Pd-Ag-Si, and Pd-Cu-Si ternary systems [40]. In 1974, systematic investigations of Chen on Pd-Si-, Pd-P-, and Pt-P-based MGs led to the fabrication of spheres with diameters of 1 - 3 mm [41]. Turnbull et al. [42, 43] produced glassy spheres of Pd-Ni-P MG with diameters of 5 and 10 mm in 1982 and 1984, respectively, which are considered by many as the first bulk metallic glasses (BMG) to be developed. In 1993, Peker and Johnson developed a $Zr_{41.2}Ti_{13.8}Cu_{12.5}Ni_{10.0}Be_{22.5}$ rod specimen with a diameter of 14 mm and a critical cooling rate of the order of 10 K/s [44], which was known as Vitreloy 1 and was the first commercial BMG. Fabrication of Vitreloy 1 along with the works of Inoue's group, which discovered new MGs with thicknesses of up to 80 mm [45, 46], are considered as the starting point for using MGs in structural applications. Additive manufacturing has recently received attention as a versatile processing technique that enables fabrication of freeform and large MG components [47–49]. The availability of bulk specimens has facilitated the ability to measure various physical and mechanical properties that were previously impossible and has revived interest in this class of materials.

2.2 Properties and Applications

Because of their amorphous structure and lack of microstructural defects such as dislocations and grain boundaries, MGs offer desirable properties including high resistance to corrosion, oxidation, and wear, high yield strength, large yield strains, and high hardness. Such desirable properties make MGs suitable for replacing conventional alloys in various applications, some of which are discussed below.

Compared to crystalline alloys with similar compositions, MGs have slightly lower densities (ρ), similar elastic moduli (E), larger yield strains ($\sim$2%), and higher yield strengths (σ_y) at room temperature [17]. As a result, they posses superior specific strength (σ_y/ρ) and modulus of resilience (${\sigma_y}^2/2E$). A combination of desirable mechanical properties and high hardness make MGs suitable for spring materials, golf club heads, tennis racket frames, spacecraft debris shields, and shot-peening balls [39,50,51]. MGs have also found applications as pressure sensors because of their desirable mechanical properties and high corrosion resistance [52]. In addition to their desirable properties, MGs have excellent formability on micron scales and can be used for fabrication of microgears with applications in micropumps, micromotors, and robotics [53–55]. Parts made from MGs can be molded with an excellent surface finish without machining. This makes MGs suitable for low cost mirrors or mirror assemblies [56]. Certain types of MGs (Fe- and Co-based) exhibit desirable soft magnetic properties and can be used as soft magnets and magnetic cores [13,51,57]. MGs can also be used for tools/tool coatings because of their low coefficient of friction, high hardness, and high corrosion and wear resistance [51]. Ti-based MGs, which are investigated in this study, are suitable for aerospace applications and biomedical components such as prosthetic implants and surgical instruments [8]. Other applications of MGs include data storage media, cellphone cases, printer parts, accelerator radio-frequency cavities, and micro-electro-mechanical systems (MEMS) [11,13,51,58]. Despite many existing and potential applications, the widespread use of MGs has been hindered mainly because of their tendency for shear localization and brittle fracture at room temperature. Exploring techniques to improve the ductility of MGs, requires an understanding of their atomic structure and deformation mechanisms. These concepts are discussed in the following sections.

2.3 Atomic Structure

If a liquid cools down faster than a critical cooling rate, crystallization is suppressed and the liquid continues to remain in the liquid state (a supercooled liquid) even below its melting temperature.

Atomic movements in a liquid strongly depend on temperature; atoms move rapidly at high temperatures and become slower as the temperature decreases. Below a certain temperature, atomic movements become so sluggish that the structure appears to be frozen, i.e., kinetic arrest occurs. This temperature is known as the glass transition temperature (T_g) and the product is an amorphous phase with higher volume (implying a lower density), viscosity, energy, and entropy compared to the crystalline phase [13, 59]. If the amorphous phase is annealed at a temperature below the glass transition temperature, structural relaxation occurs and the volume decreases [13].

Due to the amorphous structure of MGs, traditional concepts describing the structure of crystalline materials are no longer applicable and new concepts must be used instead. The most frequently used concept in describing the structure of MGs is free volume, defined as the space between atoms. The success of Cohen and Turnbull in quantifying free volume [59–61] made the concept widely popular and it was later used to explain various properties of MGs including atomic transport and deformation [13, 17, 62–64]. Free volume originated from the model of dense random packing (DRP) of hard spheres [65]. According to the DRP model, an amorphous structure is considered as a random arrangement of atoms modeled as hard spheres [62, 66]. Packing limitations caused by geometrical constraints lead to formation of free volume inside the material [64]. In this structure, each atom is confined within a cage of neighboring atoms and is unable to move unless free volume happens to exist next to it, as shown schematically in Fig. 2.1 [13].

The DRP model provides a reasonable description of monoatomic glasses and there has been considerable effort to propose a modified version of it that holds for polyatomic glasses [67–69]. Despite these efforts, many details of the structure of MGs still cannot be explained by DRP-based models. The most important reason is that metallic atoms can be squeezed together at some energy cost and thus cannot be considered as ideal hard spheres. As a result, the validity of the free volume concept for MGs was questioned from the beginning. Other concepts (e.g., local topological fluctuations) have also been proposed and applied to explain the structure of MGs. However, none of these concepts are as popular as free volume and the problem of precisely describing the structure of MGs is still an ongoing discussion [13].

2.4 Deformation Mechanisms

Although the exact nature of atomic structure in MGs is not fully resolved, it has been widely accepted that the fundamental process underlying the deformation must be a local rearrangement of atoms to accommodate shear strain [13, 17, 62, 70, 71]. At the atomic level, a local rearrangement in

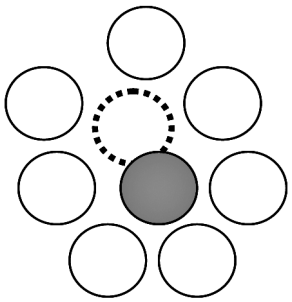

Figure 2.1: Schematic illustration of free volume [13].

neighboring atoms can take place through disruption and formation of local atomic bonds. Since the atomic bonds of MGs are metallic, there is no concern about the rigidity of the bond angles or the balance of charges [17]. The local rearrangement of atoms is usually described by two mechanisms: diffusive atomic jump and shear transformation zone (STZ).

The diffusive atomic jump mechanism is based on the free volume concept and was applied to the deformation of MGs by Spaepen [72]. According to this mechanism, deformation is described as a series of discrete diffusion-like atomic jumps into neighboring free volume, as shown schematically in Fig. 2.2. It is evident that the atomic jumps are more likely to take place near regions of high free volume. Spaepen assumed that atoms are in positions of relative stability, i.e., local free energy minima, before and after the jump and some activation energy of motion must be supplied for the atomic jump to take place. In the absence of external forces, the activation energy is supplied by thermal fluctuations of atoms and the number of jumps across the activation barrier is the same in forward and backward directions. When external forces are present, e.g., a shear stress is applied, the atomic jumps are biased in the direction of the applied force. In this scenario, the number of forward jumps across the activation barrier is larger than the number of backward jumps, which results in a net forward flux of atoms and forms the basic mechanism for flow [72].

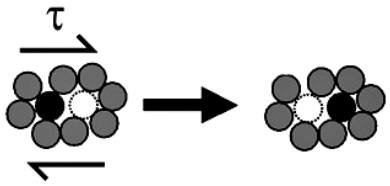

Figure 2.2: Schematic illustration of a diffusive atomic jump [17].

Shortly after the introduction of the diffusive atomic jump mechanism, Argon [73] proposed the STZ mechanism for deformation of MGs. The STZs, shown schematically in Fig. 2.3(a), are narrow disk shaped clusters of closely packed atoms that undergo shear distortion to accommodate the

applied shear strain. As shown in Fig. 2.3(b), deformation through STZs can also be envisioned by treating the amorphous structure as an elastic continuum, where atoms are substituted by a continuum mesh [70]. Similar to the diffusive atomic jumps, formation of STZs requires atoms to cross a state of atomic configuration with high energy in order to transport from one relatively low energy atomic configuration to another [17, 62]. Therefore, STZs are transient states of atomic configurations and cannot be considered as structural defects in the way that a dislocation is a crystal defect. However, operation of STZs is strongly influenced by local atomic arrangements, where regions of relatively loosely packed atoms (i.e., regions with higher free volume) would more readily accommodate local shear strain. Computational simulations predicted that STZs are composed of a few to ∼100 atoms and also suggested that STZs are common to the deformation of all MGs [17]. Once STZs are formed, they produce a localized distortion in the surrounding material which leads to the formation of larger planar bands of STZs having a width of 10 - 20 nm, known as shear bands [13].

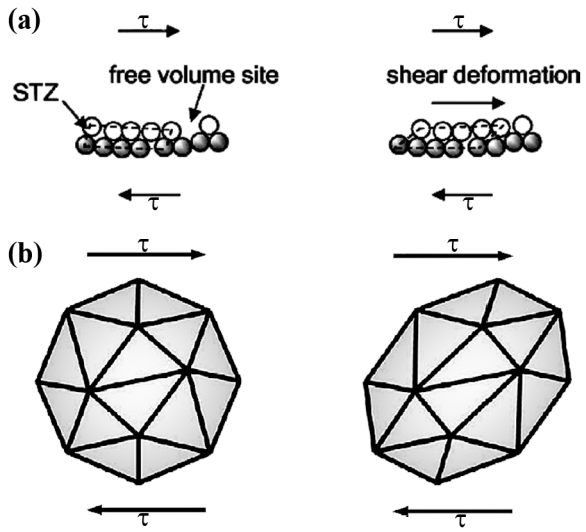

Figure 2.3: Schematic illustration of deformation via an STZ (left) before and (right) after shear deformation [70, 74].

Deformation of MGs at the atomic level is better modeled by the STZ mechanism than diffusive atomic jump [70]. However, both mechanisms are thermally activated and a transient state of dilatation is necessary for their operation. In addition, both mechanisms are typically accompanied by a semi-permanent increase in free volume after operation (flow dilatation). Since more atoms are redistributed during formation of STZs, the activation energy for operation of an STZ (20 - $120kT_g$, where k is the Boltzmann constant) is higher than that required for an atomic jump into

the neighboring free volume (15 - 25kT_g) [17]. Both mechanisms introduce state variables, such as stress, temperature, and local structural parameters (free volume), to the problem of deformation of MGs and allow constitutive laws to be developed, for example on the basis of competition between creation and annihilation of free volume [17, 70].

Unlike crystalline metals, in MGs only a single mechanism is sufficient to explain various deformation modes. At high temperatures (0.6T_g - T_g), MGs deform homogeneously with significant plasticity. As the temperature decreases, MGs exhibit inhomogeneous deformation that is accompanied by very limited ductility and sudden fracture. The temperature at which the deformation behavior changes from homogeneous to inhomogeneous (ductile to brittle transition) is strongly dependent on the applied strain rate [13, 62]. Although the macroscopic response of MGs is quite different during homogeneous and inhomogeneous deformation, a single mechanism (either the diffusive atomic jump or STZ) can be used to explain the deformation behavior. Homogeneous deformation is the result of the occurrence of diffusive atomic jumps and/or STZs throughout the entire volume of the material. Whereas, during inhomogeneous deformation atomic rearrangements are limited to localized volume elements of the material [17].

2.5 Elastic Deformation

The bulk modulus and shear modulus of MGs are typically smaller than crystalline alloys of similar compositions. For crystalline alloys, the bulk modulus decreases with increasing equilibrium separation between atoms [75]. MGs are 0.5 - 2.0% less dense than their crystalline counterparts. Therefore, on average the interatomic spacings in MGs are larger than crystalline alloys. Assuming a similar short-range order and cohesive forces for the amorphous and crystalline structures, the difference in interatomic spacing adequately explains the difference in bulk modulus. Differences in the shear modulus of MGs and crystalline alloys are too large (25 - 30%) to be explained on the basis of larger interatomic spacings alone. The discrepancy is believed to be a result of anisotropy on the atomic scale. Although MGs are macroscopically considered to be isotropic, local topology of their atomic bonds is not identical in every atomic environment and it is probable to find regions with unstable local topology. As a result, shear stress may lead to not only elastic atomic displacements but also to a local reshuffling of atoms via an exchange of the atomic bonds, shown schematically in Fig. 2.4. The atomic bond exchange, which is also known as anelastic operation of STZs, becomes activated even at small shear strains and as a result shear deformation of MGs is inherently anelastic at any stress level, even if the macroscopic response appears to be elastic [13, 17, 64].

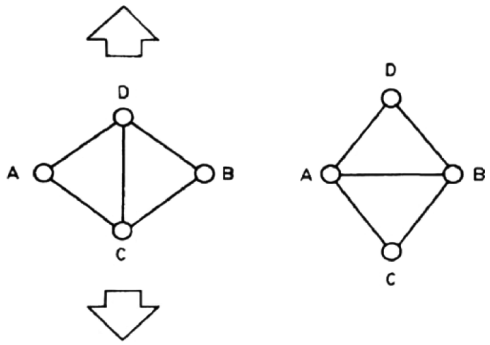

Figure 2.4: Schematic illustration of an atomic bond exchange where in (left) the bond D-C breaks and in (right) the bond A-B is formed [13].

2.6 Yield Criterion

An important characteristic of the yield criteria of ductile crystalline alloys is their symmetry, predicting yield stresses of equal magnitude in tension and compression. In contrast, MGs have demonstrated asymmetric yield behavior in several studies. For example, Mukai et al. [76] reported different shear-off angles for a $Pd_{40}Ni_{40}P_{20}$ MG under tension and compression (see Fig. 2.5). In another study, Zhang et al. [77] also reported a different shear-off angle as well as different yield stresses for a $Zr_{59}Cu_{20}Al_{10}Ni_8Ti_3$ MG under tension and compression. Donovan [78] suggested that MGs obey the Mohr-Coulomb yield criterion, where shear yield stress (τ_y) depends not only on the applied shear stress, but also on the stress normal to the shear displacement plane (σ_n):

$$\tau_y = \tau_0 + \alpha\sigma_n \tag{II.1}$$

where α is a system-specific coefficient that controls the strength of the normal stress effect [13,64,78]. This was further confirmed by the atomistic calculations of Schuh and Lund [79].

2.7 Plastic Deformation

Macroscopic plastic deformation of MGs is a biased accumulation of local strains accommodated through the operation of diffusive atomic jumps and/or STZs and the redistribution of free volume. Depending on the temperature and the applied strain rate, local atomic rearrangements can be distributed homogeneously or inhomogeneously [17]. Homogeneous plastic flow of MGs is described as viscous flow of a supercooled liquid, and is typically observed at elevated temperatures. Homogenous flow is accommodated via structural disordering and reordering events, where local diffusive

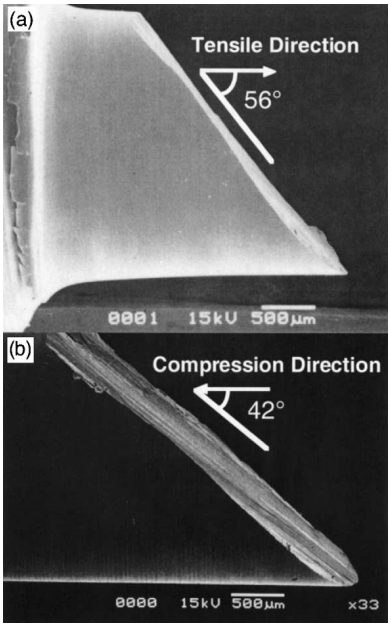

Figure 2.5: A side view of the $Pd_{40}Ni_{40}P_{20}$ MG fractured in (a) tension and (b) compression [76].

atomic jumps and/or STZs lead to flow dilatation and creation of free volume and the relaxation process leads to annihilation of free volume. If the creation and annihilation of free volume reach a balance, steady-state homogeneous flow will be observed. Otherwise, the net gain or loss of free volume would not be zero and homogenous flow would no longer be steady-state [17].

Inhomogeneous deformation of MGs is described via the localized flow of the material within shear bands [17, 64], and is typically observed at lower temperatures. Shear band formation is generally recognized as a consequence of strain softening due to the local creation of free volume (flow dilatation) and heat generation inside the shear bands [17]. Yang et al. [80] reported that the temperature inside the shear bands is close to the glass transition temperature of the MG. It is known that the viscosity of MGs decreases rapidly once the temperature is near the glass transition temperature. As a result, the material within a shear band behaves like a liquid layer of reduced viscosity and its strain rate becomes much higher than the surrounding matrix. Therefore, the strain in the shear band increases rapidly, which leads to rapid propagation of the shear band and abrupt failure [13, 17, 62].

2.8 Pursuit of Ductility

It is commonly believed that fracture initiates when the shear strain on a particular shear band reaches a critical value, which depends on the composition and loading condition. If shear band propagation is not constrained in some manner, plastic strain accumulates on one dominant shear band and reaches the critical value, while the strain on any other shear band is still relatively small. Therefore, fracture occurs with limited macroscopic plastic strain and the ductility of MGs is essentially zero. However, if it were possible to distribute the applied strain over many shear bands, instead of a few dominant ones, and limit shear band propagation, the onset of fracture might be delayed and significant macroscopic plastic strain could be realized.

One approach to constrain shear band propagation is to introduce one or more discontinuous crystalline phases inside the amorphous matrix of the MG [17]. Several groups have reported improvements in mechanical properties of MG-matrix composites compared to fully amorphous MGs. For example, a Ti-Zr-based MG-matrix composite with a tensile ductility of about 10% and yield strength of 1.2 - 1.5 GPa at room temperature was produced by Hofmann et al. [14] via formation of a body centered cubic (bcc) crystalline phase inside the amorphous matrix. In another study, the Charpy fracture toughness of Vitreloy 1 was improved by a factor of 2.5 after introduction of bcc Zr-Ti dendrites into the amorphous matrix. A fracture strain of 8.3% in compression and 5.5% in tension was also reported for the MG-matrix composite in the same study [81]. Fan et al. [82] also reported a 1.1% increase in plastic strain during compression experiments on a Zr-based MG containing 2.0 - 2.5 nm diameter nanocrystals. A number of recent studies reported enhancements in the fracture strength and strain of Ti-based MG-matrix composites containing *in situ* bcc dendrites under quasi-static and dynamic compressive loads [18, 19, 21]. Stress-induced martensitic transformation of the dendrites from bcc to an orthorhombic crystalline phase was reported to further improve the mechanical properties and lead to significant strain hardening of the Ti-based MG-matrix composites [21].

2.8.1 Partial Crystallization by Ion Irradiation

The two goals of making a MG-matrix composite are to promote initiation of a large number of shear bands (to distribute the macroscopic plastic strain over as large a volume as possible) and to inhibit shear band propagation (to reduce the shear strain on any one band and thus delay fracture) [17]. Enhancement in the mechanical properties of MG-matrix composites is dependent on the size, distribution, and strength of the crystalline phase [13, 83]. Therefore, it is necessary

to determine and control the mechanisms governing the nucleation and growth of the nanocrystals. Ion irradiation has been one of the techniques used for the production of partially crystallized MG-matrix composites since it has the ability to enable the nucleation of crystals but minimize their growth [84–89].

During ion irradiation, the energy of the ions is transferred to the electrons and nuclei of target atoms (i.e., electronic and nuclear collisions). This transfer of energy results in a number of different processes shown schematically in Fig. 2.6. Collision of energetic ions with electrons results in ionization, emission of electrons, and electromagnetic radiation. Upon nuclear collisions, target atoms will be knocked out of their original sites if the transferred energy is larger than a critical value, known as the displacement energy. If the primary knock-on atoms have sufficient energy, they in turn displace more target atoms. Continuation of this process leads to the formation of a localized region with a high density of displaced atoms and excess free volume, referred to as a damage cascade. At some point, moving atoms do not have enough energy to create further displacements and the remaining energy is lost via lattice vibrations and localized heating. This period of lattice heating is referred to as a thermal spike and may exist for several picoseconds before quenching to room temperature [90, 91]. Nuclear collisions are the predominant mechanism of energy deposition when the target is bombarded with low energy ions possessing high atomic number. Whereas, electronic collisions are more likely for a high energy ion with low atomic number [90].

The buildup of irradiation-induced defects is capable of raising the free energy of the system to a point where transformation to another phase is thermodynamically favorable [90]. In the case of MGs, the creation of excess free volume leads to enhanced atomic mobility inside the damage cascades and may induce crystallization [85, 86]. Despite the fact that the temperature rise (inside the cascades) is high enough to cause localized melting, the quenching process occurs much faster than the critical cooling rate required for the formation of MGs. Therefore, irradiation-induced crystallization is not a direct consequence of localized heating [86,92]. However, the local temperature rise may still lead to structural relaxations [86].

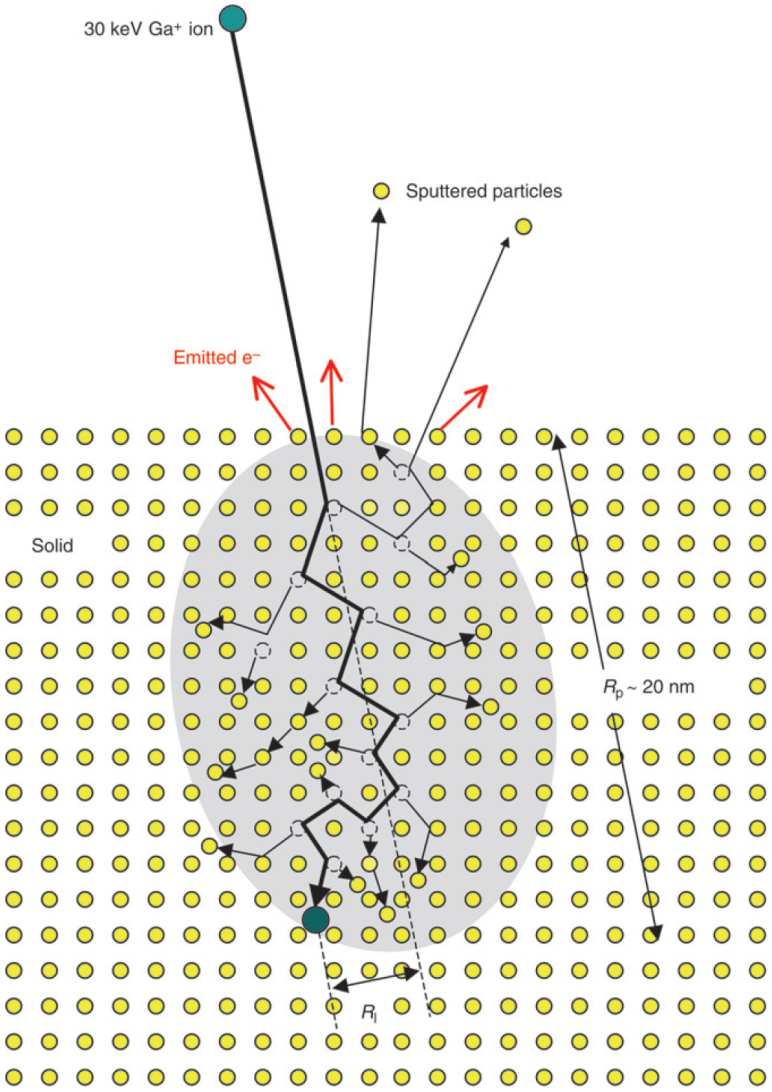

Figure 2.6: Schematic illustration of a damage cascade generated by a 30 keV Ga^+ ion incident on a crystal lattice, showing the damage created in a volume with the projected ion range of R_p and lateral range of R_l [91].

CHAPTER III

EXPERIMENTAL DETAILS

3.1 Fabrication of Specimens

Ti-based MG specimens with a nominal composition of $Ti_{40}Cu_{34-x}Pd_{14}Zr_{10}Sn_2Si_x$ (at.%), where x = 2, 3, and 5, were used in this study. The specimens, in the shape of ribbons with a thickness of ∼30 μm and a width of ∼2 mm, were fabricated at Tohoku University in Japan. To prepare the master ingots, a mixture of Ti, Cu, Pd, Zr, Sn, and Si with purities of 99.9% or more by mass was melted in an argon atmosphere purified using a titanium getter. Rapidly solidified ribbons were then fabricated by the melt spinning process, shown schematically in Fig. 3.1, where the master ingots were remelted in quartz tubes and then ejected with an over pressure of 35 kPa through a nozzle onto a rotating copper roll in an argon atmosphere. The copper wheel was cooled internally and rotated with a surface velocity of 40 m/s to provide the cooling rate required for fabrication of amorphous specimens.

3.2 Annealing

According to the potential energy landscape model, transition of a supercooled liquid to a glass corresponds to trapping the structural configuration in a local minimum state of potential energy [94]. An ideal glass represents a metastable state with the lowest potential energy for the amorphous phase, whereas the crystalline state represents the stable equilibrium state. Physical properties of an ideal glass are the same as those of the supercooled liquid extrapolated to the working temperature. In practice, the potential energy of a glass deviates from that of an ideal glass by a certain degree that depends on thermal history. Annealing a glass at a temperature high enough for atomic motion, but

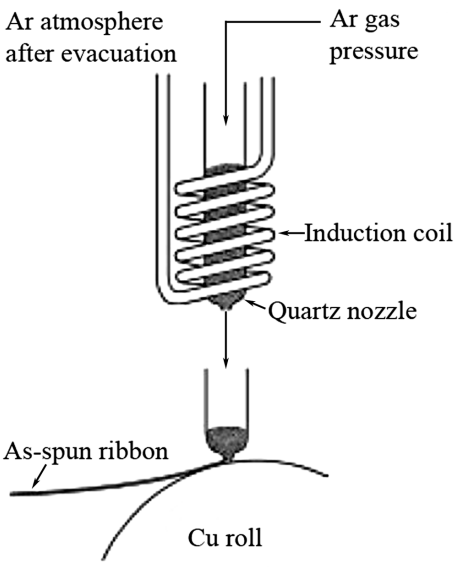

Figure 3.1: Schematic illustration of the melt spinning process [93].

insufficient for crystallization (below the glass transition temperature) results in traversing a series of lower energy states within the potential energy landscape. This process allows a transition towards the ideal glass at a constant temperature and is commonly referred to as structural relaxation [17]. Annealing-induced structural relaxation is accompanied by variations in free volume content and short/medium range atomic order and thus may alter the physical and mechanical properties of MGs [13, 94–96].

To study the effects of annealing, two as-spun $Ti_{40}Cu_{32}Pd_{14}Zr_{10}Sn_2Si_2$ specimens were isothermally annealed inside a vacuum chamber at TAMU. A glass transition temperature of 430 °C and onset of crystallization temperature of 510 °C have been reported for this alloy [97]. One specimen was annealed at 300 °C ($\sim 0.70T_g$) and the other at 400 °C ($\sim 0.93T_g$), for 4 h. The vacuum pressure remained below 1×10^{-6} Torr during annealing except for ∼10 min during the initial heating, when outgassing raised the vacuum pressure to 1×10^{-5} Torr. A single cartridge heater was used as the heating source and the power was controlled through a variable transformer. A thermocouple was used to monitor the temperature and ensure that it stayed within ± 5 °C of the desired temperature during the annealing process. After annealing, the specimens remained under vacuum for ∼3 h to cool down to room temperature.

3.3 Ion Irradiation

Ion irradiation was performed at TAMU using a 1.7 MV General Ionex Tandem accelerator. A set of magnetic scanning coils was used to raster scan the ion beam over the specimen to ensure a uniform irradiated area. Three studies were performed to investigate the effects of irradiation fluence and temperature on the structure and mechanical response of the specimens. In the first study, irradiation was performed at room temperature over a range of fluences to study the effects of irradiation fluence. For the second study, irradiation was performed at elevated temperatures to study the effects of concurrent annealing and irradiation. Finally, the findings of the first two studies were used to design a two-step irradiation process in an attempt to achieve a controllable crystallization behavior. Details of the irradiations performed in each study are described in Sections 3.3.1 - 3.3.5. For each study, the simulated depth profiles of implanted ion concentration and irradiation damage were calculated with Stopping and Range of Ions in Matter (SRIM)-2008 using the ion distribution and quick calculation of damage option [98]. Considering that SRIM only takes into account ion-solid collisions, thermal effects (e.g., annealing-induced atomic diffusion or free volume annihilation) do not have any influence on the simulated depth profiles of implanted ion concentration and irradiation damage [98].

3.3.1 Ion Irradiation at Room Temperature

Ion irradiation leads to the formation of damage cascades (i.e., localized regions with a high density of displaced atoms) inside which a majority of atoms are in temporary motion. At lower fluences, the damage cascades are spatially separated from each other, as shown in Fig. 3.2(a). Therefore, the volume of the disordered region is determined primarily by the stopping point of the ion and the range of the displaced atoms (see Fig. 3.2(b)). As irradiation fluence increases, damage cascades overlap and form a continuous region of displaced atoms (see Fig. 3.2(c)). In other words, at higher fluences volume of the disordered region becomes larger. Such high volume of disordered atoms along with localized heating caused by lattice vibrations may raise the free energy of the system to a point where transformation to another phase is thermodynamically favorable [90]. To investigate the effects of fluence on the structure and mechanical response of MGs, as-spun $Ti_{40}Cu_{32}Pd_{14}Zr_{10}Sn_2Si_2$ specimens were irradiated with 4 MeV Fe^{2+} ions at 25 °C using a fluence of 1×10^{12}, 1×10^{13}, 1×10^{14}, and 1×10^{15} ions/cm^2. The Fe^{2+} ion beam is one of the most commonly used beams in the Tandem accelerator. An ion energy of 4 MeV was selected to minimize the near-surface doping effects and to ensure that the irradiation-induced damaged layer can be conveniently probed during

the characterization of microstructure and mechanical properties.

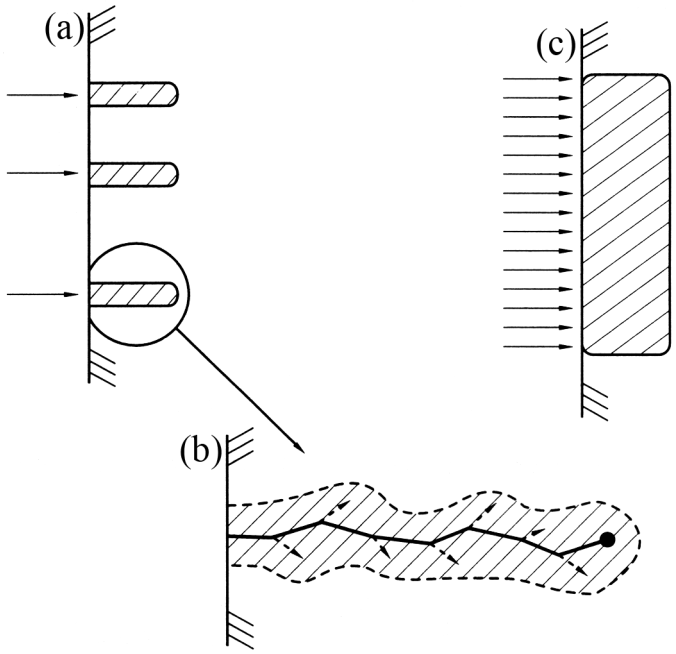

Figure 3.2: Schematic illustration of the disorder produced during room temperature ion irradiation using (a) and (b) low and (c) high fluences [90].

3.3.2 Ion Irradiation at Elevated Temperature - Below the Glass Transition Temperature

To investigate the effects of concurrent annealing and irradiation, as-spun $Ti_{40}Cu_{32}Pd_{14}Zr_{10}Sn_2Si_2$ specimens were irradiated with 4 MeV Fe^{2+} ions at 25, 100, 200, and 300 °C using a fluence of 1×10^{13} ions/cm^2. A glass transition temperature of 430 °C and onset of crystallization temperature of 510 °C have been reported for this alloy [99]. During irradiation, the specimens were glued from both ends to a filament-heated stage, to which a thermocouple was mechanically attached for temperature monitoring. The temperature readings were used to adjust the filament current for automatic temperature control.

3.3.3 Ion Irradiation at Elevated Temperature - Below and Above the Glass Transition Temperature

Studies performed in Section 3.3.2 showed no evidence of crystallization when ion irradiation was performed below the glass transition temperature. To further investigate the possibility of creating a

MG-matrix composite through concurrent annealing and irradiation, as-spun $Ti_{40}Cu_{31}Pd_{14}Zr_{10}Sn_2Si_3$ specimens were irradiated with 3.5 MeV Cu^{2+} ions at 100, 200, 250, 300, 390, and 480 °C using a fluence of 1×10^{16} ions/cm^2. A glass transition temperature of 440 °C and onset of crystallization temperature of 490 °C have been reported for this alloy [99]. Irradiations were performed under vacuum at a pressure of 10^{-6} Torr and the temperature was monitored in the same manner explained in Section 3.3.2. The Cu^{2+} ion beam was selected for this study (instead of the Fe^{2+} ion beam used in previous studies to minimize changes in chemical composition caused by ion implantation. All future irradiations were also performed using the Cu^{2+} ion beam.

3.3.4 Ion Irradiation at Elevated Temperature Followed by Ion Irradiation at Room Temperature

Studies performed in Sections 3.3.1 - 3.3.3 demonstrated the difficulty of achieving a controllable crystallization behavior through a single step irradiation. No crystallization was observed when specimens were subjected to ion irradiation at room temperature (regardless of the fluence used). For specimens irradiated at elevated temperature it was found that there is a critical temperature below which the specimens remained amorphous. When irradiation was performed at temperatures higher than the critical temperature, the specimens crystallized to depths beyond the range of the implanted ions. Several studies have reported the possibility of amorphization of a crystalline structure by means of ion or electron irradiation [100–105]. More importantly, electron-induced crystallization and re-amorphization has been reported as a viable path for achieving a controllable crystallization behavior [106, 107]. Therefore, a two-step irradiation was designed to investigate the possibility of achieving a controllable crystallization behavior through crystallization and re-amorphization. For this study, as-spun $Ti_{40}Cu_{31}Pd_{14}Zr_{10}Sn_2Si_3$ specimens were irradiated with 3.5 MeV Cu^{2+} ions at 300 °C using a fluence of 1×10^{16} ions/cm^2 to induce crystallization. Subsequently, the crystallized specimen was irradiated again with 3.5 MeV Cu^{2+} ions at 25 °C using a fluence of 1×10^{14}, 1×10^{15}, and 1×10^{16} ions/cm^2. A glass transition temperature of 440 °C and onset of crystallization temperature of 490 °C have been reported for this alloy [99].

3.3.5 Additional Ion Irradiation at Elevated Temperature

Studies performed in Sections 3.3.3 and 3.3.4 suggested that the microstructure of the specimens irradiated at elevated temperature was affected by ion beam heating. This was further investigated by performing additional irradiations at elevated temperatures. For this study, as-spun

$Ti_{40}Cu_{29}Pd_{14}Zr_{10}Sn_2Si_5$ specimens were irradiated with 3.5 MeV Cu^{2+} ions at 325, 385, 400, 440, 450, 460, and 480 °C using a fluence of 1×10^{16} ions/cm^2. A glass transition temperature of 450 °C and onset of crystallization temperature of 508 °C have been reported for this alloy [99]. Irradiations were performed under vacuum at a pressure of 10^{-8} Torr using an average beam intensity of 5×10^{11} ions/cm^{2}s. The ion beam had a rectangular shape of 12×6.5 mm^2 and its current was kept below 125 nA to minimize the beam heating.

3.4 Characterization Techniques

3.4.1 X-Ray Diffraction

A Bruker-D8 Discover X-ray diffractometer (XRD) with Cu K_α radiation (λ=0.1540562 nm) was used to characterize the crystallographic structure of the specimens. The XRD patterns were collected using the conventional $\theta/2\theta$ scanning method. Although XRD is a non-destructive and relatively convenient method for studying atomic structure, the signal to noise ratio of crystalline phases embedded in an amorphous matrix could be low especially when the dimensions and concentrations of crystalline phases are smaller than a few nanometers and a few percentage by mass, respectively [108, 109]. For example, Luo et al. [85] did not observe any evidence of crystallization in the XRD patterns of Zr-based MG specimens subjected to irradiation using 300 keV Ga^+ ions. However, selected area diffraction (SAD) patterns of the same specimens, obtained from transmission electron microscopy, revealed formation of a face centered cubic (fcc) crystalline phase with an average diameter of 5 nm after ion irradiation. The discrepancy between the XRD and SAD results have been attributed to the low concentration of the crystalline phases.

3.4.2 Transmission Electron Microscopy

The microstructure of the specimens was examined by a 200 kV Technai F20 transmission electron microscope (TEM). Cross-sectional TEM specimens were prepared using a Tescan LYRA-3 focused-ion-beam (FIB). A 30 keV Ga beam was first used to thin the specimens to a few microns and then a 5 keV Ga beam was used to further reduce the thickness to 100 nm. Finally, the specimens were polished using a 2 keV Ga beam to remove beam damage.

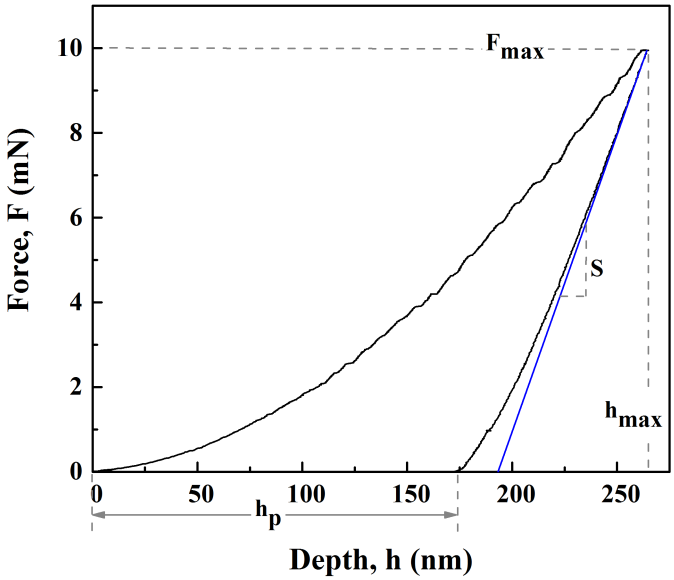

Figure 3.3: A typical force vs. penetration depth curve obtained for the as-spun $Ti_{40}Cu_{32}Pd_{14}Zr_{10}Sn_2Si_2$ specimen using a Berkovich indenter.

3.4.3 Nanoindentation

Mechanical response of the specimens was studied by nanoindentation experiments performed with a force-controlled Hysitron nanoindenter. The specimens were mounted on glass slides using instant adhesive to provide a flat surface required for nanoindentation. During nanoindentation experiments, the applied force and the resulting penetration depth of an indenter throughout a complete loading-unloading cycle are continuously recorded. The recorded data is then plotted as a test force (F) vs. penetration depth (h) curve, which is used to obtain the elastic modulus (E) and hardness (H) of the specimens, without the need to measure the size of the residual impressions. Elastic modulus of a material is a measure of the strength of its atomic bonds. For crystalline and inorganic amorphous materials, elastic modulus is related to the external force required to elastically compress or extend the interatomic spacings in opposition to the internal forces that seek to maintain an equilibrium (undistorted) interatomic spacing [75]. Hardness of a material is generally defined as its resistance to plastic deformation in the form of indentation, scratch, or wear. Hardness is not a fundamental material property because, for example, resistance to indentation depends on the shape of the indenter and the applied force. However, hardness testing is equivalent to performing a compression test on a small volume of a material. According to Tabor's relationship, hardness of a material is proportional to its yield strength (σ_y) by:

$$H \approx c\sigma_y \tag{III.1}$$

where c is a proportionality constant. Theoretical studies, based on plane strain slip-line analysis of a smooth flat punch indenter penetrating into the surface of a semi-infinite body, have shown that for a perfectly plastic material the magnitude of c is $\sim$3 [110, 111]. Experimental data have demonstrated that this is a reasonable approximation for MGs as well [112].

Figure 3.3 shows a typical force vs. penetration depth curve obtained for the as-spun $Ti_{40}Cu_{32}Pd_{14}Zr_{10}Sn_2Si_2$ specimen at a maximum force of 10 mN using a Berkovich indenter. According to the method of Oliver and Pharr [113], the unloading data can be described by a power law relation shown below:

$$F = K(h - h_p)^m \tag{III.2}$$

where h_p is the permanent penetration depth after the removal of the test force. The constants K, m, and h_p are all determined by a least square fitting procedure. The initial unloading slope is then found by analytically differentiating Eq. III.2 with respect to h and evaluating the derivative at the maximum penetration depth (h_{max}):

$$S = \left.\frac{dF}{dh}\right|_{h=h_{max}} \tag{III.3}$$

where S is the stiffness. Measuring the stiffness allows for the determination of reduced elastic modulus (E_r) by:

$$E_r = \frac{\sqrt{\pi}}{2}\frac{S}{\sqrt{A_p}} \tag{III.4}$$

where A_p is the projected area of the contact (i.e., contact area) between the indenter and the specimen. The reduced elastic modulus, defined by $1/E_r = [(1-\nu^2)/E] + [(1-\nu_i^2)/E_i]$, takes into account the fact that elastic deformation occurs in both the specimen, with elastic modulus of E and Poissons ratio of ν, and the indenter, with elastic constants of E_i and ν_i. Hardness of the specimen can also be determined through the knowledge of the projected area of the contact and the maximum force applied to the specimen (F_{max}) using the following equation:

$$H = \frac{F_{max}}{A_p} \tag{III.5}$$

To obtain hardness and reduced elastic modulus, it is necessary to determine the projected area of the contact between the indenter and the specimen. The projected area of contact, shown

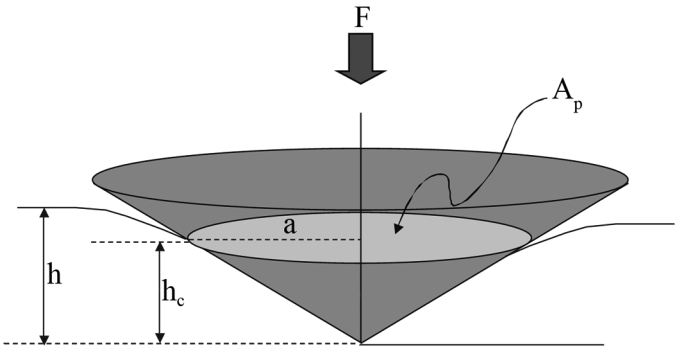

Figure 3.4: Schematic illustration of the projected area of contact for a conical indenter [114].

schematically in Fig. 3.4 for a conical indenter, is determined through knowledge of the area function of the indenter and the depth over which the indenter and specimen are in contact (i.e., contact depth, h_c). For pyramidal, conical, and spherical indenters, the contact depth is calculated by:

$$h_c = h_{max} - 0.75\frac{F_{max}}{S} \tag{III.6}$$

The area function of the indenter is a function that relates its cross-sectional area to the distance from its tip:

$$A_p = f(h_c) = C_1 h_c^2 + C_2 h_c + C_3 h_c^{1/2} + C_4 h_c^{1/4} + C_1 h_c^{1/8} \tag{III.7}$$

where C_1, C_2, ... , and C_5 are constants obtained from calibration. The lead term in Eq. III.7 describes a perfect indenter geometry and the remainder of the terms describe deviations from the ideal geometry due to rounding or blunting at the apex of the tip. It should also be noted that raw penetration depths recorded during the test are the sum of the displacements in the specimen and the load frame. Therefore, it is essential to account for the load frame compliance (C_f). Using the method suggested by Oliver and Pharr [113], both the area function of the indenter and load frame compliance can be simultaneously determined by making a series of indentations in two materials with known mechanical properties (usually fused silica and tungsten). According to this method, the load frame and specimen are considered as two springs in series. Therefore, the total measured compliance is the sum of the compliance of the specimen (C_s) and load frame:

$$C = C_s + C_f \tag{III.8}$$

Since the compliance of the specimen during an elastic contact is given by the inverse of the contact

stiffness, Eqs. III.4 and III.8 combine to yield:

$$C = \frac{\sqrt{\pi}}{2E_r}\frac{1}{\sqrt{A_p}} + C_f \tag{III.9}$$

According to Eq. III.9, a plot of C vs. $1/\sqrt{A_p}$ is linear for a given material and the y-intercept is a direct measure of the load frame compliance. Once the load frame compliance is determined, contact area is computed for all the indentations performed in the reference specimen by using the following equation:

$$A_p = \frac{\pi}{4}\frac{1}{E_r^2}\frac{1}{(C - C_f)^2} \tag{III.10}$$

The projected areas of contact obtained from Eq. III.10 are then plotted as a function of contact depth. The area function, in the form of Eq. III.7, is then determined by fitting the projected area of contact vs. contact depth plot.

To measure the reduced elastic modulus and hardness of the specimens, a diamond Berkovich indenter was used for the indentations. The force vs. penetration depth curves of MGs typically show multiple serrations during the loading portion of the curve, similar to those visible in Fig. 3.3. Each serration represents a sudden increase in the penetration depth of the indenter at a relatively constant force. These serrations, also known as displacement bursts or pop-ins, have been attributed to activation of individual shear bands during deformation [13,17,62]. Therefore, the initial displacement burst has been associated with the onset of plastic deformation in MGs [115, 116]. To study the initial displacement burst, a clear transition between the elastic and plastic regions of the force vs. penetration depth curves is required. Although displacement bursts were observed in the force vs. penetration depth curves obtained from indentations with a Berkovich indenter, most were not sharp and horizontal, i.e., not clearly defined. This is mainly due to the rapid stress rise under the relatively sharp Berkovich indenter, which leads to plastic deformation even at shallow penetration depths. However, if a spherical indenter is used for indentations, the stress rise under the indenter is more gradual and as a result the elastic deformation region extends to a greater penetration depth [116]. Moreover, it has been reported that a slower loading rate can accentuate the displacement bursts [17, 117]. Therefore, another set of nanoindentation experiments was performed on the specimens using a spherical indenter with an estimated radius (R_i) of $\sim$1 μm and a loading rate slower than that used for the Berkovich indentations. Details of the loading sequence used for each set of indentations are described in Chapter IV.

The ability of MGs to form shear bands can also be studied from the energetic point of view,

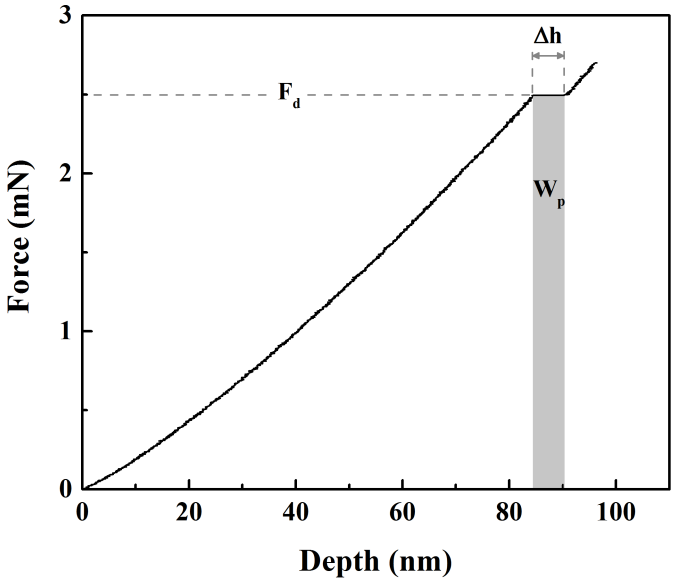

Figure 3.5: The initial portion of a force vs. penetration depth curve obtained for the as-spun $Ti_{40}Cu_{32}Pd_{14}Zr_{10}Sn_2Si_2$ specimen using a spherical indenter.

where the onset of plastic deformation corresponds to a critical point at which the effective potential energy barrier for shear band initiation is equal to the energy input by the applied force. Thus, the deformation ability of MGs is associated with the potential energy barriers for shear band initiation, where high-energy barriers are expected to hinder the initiation of shear bands and thus lower the ductility. The potential-energy barrier for the formation of shear bands can be experimentally determined by nanoindentation experiments through the concept of plastic deformation energy (PDE), which is defined as the ratio of plastic work done by the indenter at the initial displacement burst (W_p) to the volume of material displaced during the initial displacement burst (V_p). It has been reported that MGs with higher ductility have lower values of PDE [118]. Figure 3.5 shows the initial portion of a force vs. penetration depth curve for the as-spun $Ti_{40}Cu_{32}Pd_{14}Zr_{10}Sn_2Si_2$ specimen, where F_d is force at initial displacement burst and Δh is the displacement of the indenter during the initial displacement burst. To find the PDE values, the area under the initial displacement burst was considered as W_p and the calibrated area function of the spherical indenter and the average contact depth of the indenter at the initial displacement burst were used to calculate V_p. The obtained PDE values were used to compare the ductility of the specimens.

In addition to the PDE values, contribution of shear bands to plastic deformation can be assessed by comparing the total amount of deformation that occurs during the displacement bursts ($h_{discrete}$) to residual penetration depth of the indenter after the removal of the test force (h_p). If indentations

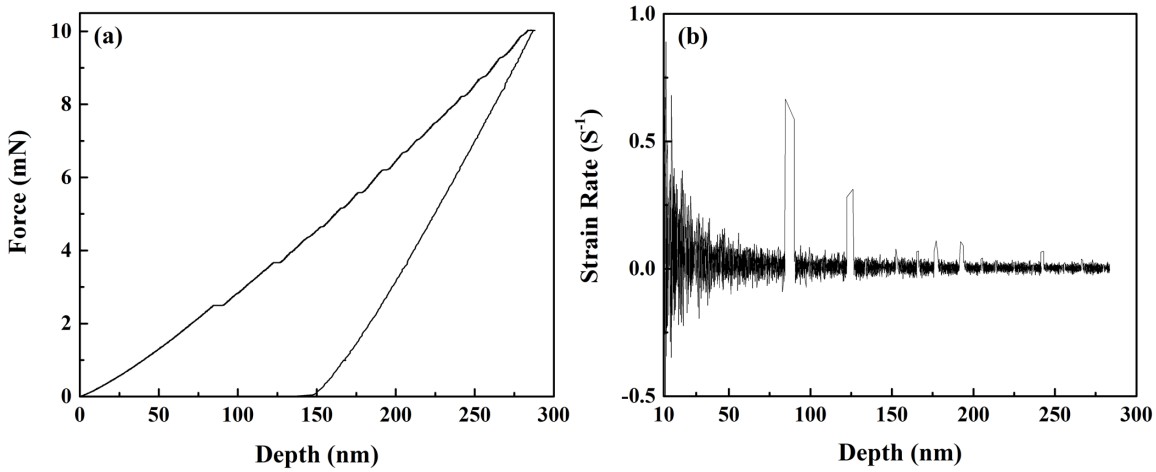

Figure 3.6: A typical (a) force vs. penetration depth curve and (b) the corresponding strain rates vs. penetration depth curve obtained for a $Ti_{40}Cu_{32}Pd_{14}Zr_{10}Sn_2Si_2$ specimen using a spherical indenter.

are performed using the same instrument and loading rate, differences in $h_{discrete}/h_p$ represent an intrinsic change in the plastic flow of the material, where a reduction in $h_{discrete}/h_p$ suggests a transition in plastic flow from discrete (inhomogeneous) to continuous (homogeneous). The transition towards more homogenous plastic flow in MGs can be attributed to simultaneous operation of multiple shear bands instead of a few dominant ones [112, 119]. Therefore, the $h_{discrete}/h_p$ values were used to compare the nature of plastic flow for the as-spun and irradiated specimens.

During nanoindentation with a constant loading rate, strain rate ($\dot{\epsilon}$) is a non-linear function of time (t) and is defined as [120–122]:

$$\dot{\epsilon} = \frac{1}{h}\frac{dh}{dt} \tag{III.11}$$

For a $Ti_{40}Cu_{32}Pd_{14}Zr_{10}Sn_2Si_2$ specimen, Fig. 3.6 shows the force vs. penetration depth curve obtained from indentations with a spherical indenter and the corresponding strain rate vs. penetration depth curve (for $10 < h < 300$ nm). For $h < 10$ nm, the strain rate is very large due to the singularity of Eq. III.11 at $h = 0$. The strain rate decreases as the indentation proceeds and eventually reaches a plateau. The strain rate vs. penetration depth curve is punctuated by multiple bursts where the strain rate increases above the noise and remains high for a few nanometers. Each strain rate burst in Fig. 3.6(b) represents a certain depth at which the indenter sinks quickly into the specimen and can be correlated to a corresponding displacement burst in the force vs. penetration depth curve shown in Fig. 3.6(a). Therefore, the strain rate vs. penetration depth curves were used, in addition

to the force vs. penetration depth curves, to facilitate the detection of displacement bursts during the analysis of spherical indentation results.

3.4.4 Post-Indentation Surface Topography

To better understand the deformation mechanisms at work, an examination of the area around the indentations performed with a Berkovich indenter was undertaken using an *in situ* scanning probe microscope (SPM) and/or an *ex situ* atomic force microscope (AFM).

CHAPTER IV

RESULTS AND DISCUSSION

4.1 Effects of Annealing [123]

Isothermal annealing was performed on as-spun $Ti_{40}Cu_{32}Pd_{14}Zr_{10}Sn_2Si_2$ specimens at 300 °C ($\sim 0.70T_g$) and 400 °C ($\sim 0.93T_g$), for 4 h. During annealing, MGs relax into their ideal glassy state, and extended annealing results in formation of the equilibrium crystalline state. However, at temperatures below the glass transition temperature, the ideal glassy and equilibrium crystalline states are unattainable within experimental time scales. For example, Kumar et al. [94] did not observe any signs of crystallization after annealing a Zr-based MG alloy at $0.9T_g$ for 165 h. Similarly, no crystallization was expected to take place in the current study because annealing was performed below the glass transition temperature. The mechanical response of the as-spun and annealed specimens was studied by nanoindentation experiments.

4.1.1 Mechanical Response

Nanoindentation experiments with a Berkovich indenter were performed on the as-spun and annealed $Ti_{40}Cu_{32}Pd_{14}Zr_{10}Sn_2Si_2$ specimens to study the effects of annealing on reduced elastic modulus and hardness. The loading sequence used for indentations consisted of loading to a maximum force of 10 mN at a loading rate of 0.33 mN/s, a 60 s hold at the maximum force to allow any time dependent plastic effects to diminish, 10 s unloading to 10% of the maximum force, a 60 s hold at 10% of the maximum force to measure thermal drift, and a 2 s final unloading. Typical force vs. penetration depth curves obtained from indentations with a Berkovich indenter on the as-spun and annealed specimens are shown in Fig. 4.1. The curves show loading, hold at maximum force, and unloading. Reduced elastic modulus and hardness of the specimens, obtained from the analysis

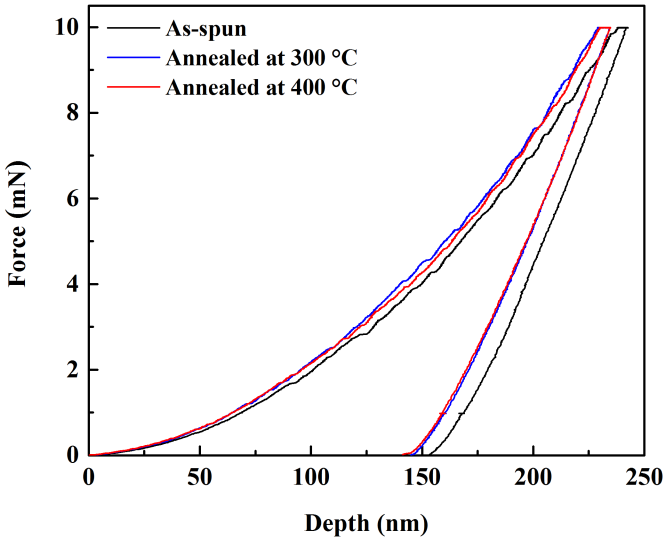

Figure 4.1: Force vs. penetration depth curves obtained from indentations with a Berkovich indenter on the as-spun and annealed $Ti_{40}Cu_{32}Pd_{14}Zr_{10}Sn_2Si_2$ specimens.

of the force vs. penetration depth curves, are shown in Fig. 4.2. Each data point is the average of 10 indentations and the error bars represent plus or minus one standard deviation. A reduced elastic modulus of 119 GPa and a hardness of 10.9 GPa were obtained for the as-spun specimen. No reports on the Poisson's ratio of the $Ti_{40}Cu_{32}Pd_{14}Zr_{10}Sn_2Si_2$ alloy is available. Fornell et al. [11] reported a Poisson's ratio of 0.36 for the $Ti_{40}Cu_{38}Pd_{12}Zr_{10}$ alloy. Using this value as an estimate for the Poisson's ratio of the as-spun specimen in the current study, the average value of reduced elastic modulus is equivalent to an elastic modulus of 116 GPa. This value is comparable with an elastic modulus of 119 GPa calculated from the reported stress-strain curves obtained from uniaxial compression on cylindrical specimens made from the same alloy [97]. No report on the hardness of the $Ti_{40}Cu_{32}Pd_{14}Zr_{10}Sn_2Si_2$ alloy is available. A comparison between the reduced elastic modulus of the as-spun and annealed specimens showed minimum changes after annealing. A large standard deviation was obtained for the average reduced elastic modulus of the specimen annealed at 300 °C. Repeating the nanoindentation experiments on this specimen resulted in a similar repeatability. A plausible explanation for this large deviation is improper mounting of the MG ribbon on the glass slide. For both specimens, annealing resulted in ∼20% increase in hardness. Similar observations have been reported, where the hardness of MGs increased after isothermal annealing [124, 125]. It is widely accepted that structural relaxations due to annealing at temperatures below the glass transition temperature lead to annihilation of free volume and a subsequent increase in density [124–127]. For example, it was reported that the density of a Zr-based MG increased by ∼0.1% upon

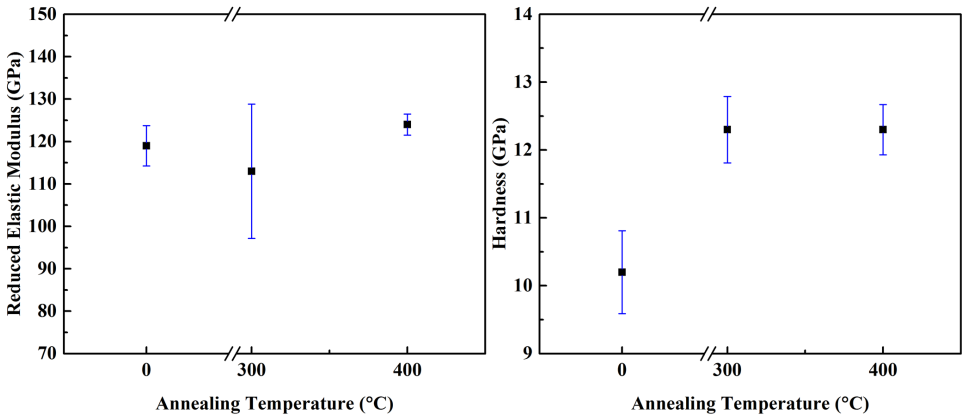

Figure 4.2: Reduced elastic modulus and hardness of the as-spun and annealed $Ti_{40}Cu_{32}Pd_{14}Zr_{10}Sn_2Si_2$ specimens.

relaxation. For comparison, complete crystallization of the same alloy increased the density by ∼0.8% [128]. Therefore, the increased hardness of the annealed specimens was attributed to the annihilation of free volume.

To study the onset of plastic deformation, another set of nanoindentation experiments was performed using a spherical indenter. The loading sequence used for these indentations was identical to that used for the Berkovich indentations except for a loading rate of 0.03 mN/s. Figure 4.3 shows the typical force vs. penetration depth curves obtained from indentations with a spherical indenter on the as-spun and annealed specimens. The curves have been offset for clarity and the initial displacement burst for each curve is marked with an arrow. A comparison between the serrated flow observed in Fig. 4.3 with that in Fig. 4.1 demonstrated that displacement bursts were more clearly defined when a spherical indenter and a slower loading rate were used. For the as-spun specimen, the force vs. penetration depth curve up to the initial displacement burst was fit to the Hertz solution for elastic contact of a non-rigid spherical indenter on a flat surface:

$$F = \frac{4}{3} E_r \sqrt{R_i h^3} \tag{IV.1}$$

where R_i is the radius of the indenter (∼1 μm) [112, 116, 129]. The agreement between the Hertz solution and the experimental curve suggested that the initial displacement burst represented the transition from purely elastic to plastic deformation (i.e., onset of plastic flow) [115, 118]. To further support this, nanoindentation experiments were performed on the as-spun specimen at forces lower than the initial displacement burst, where the loading curve was re-traced upon unloading suggesting an entirely elastic behavior.

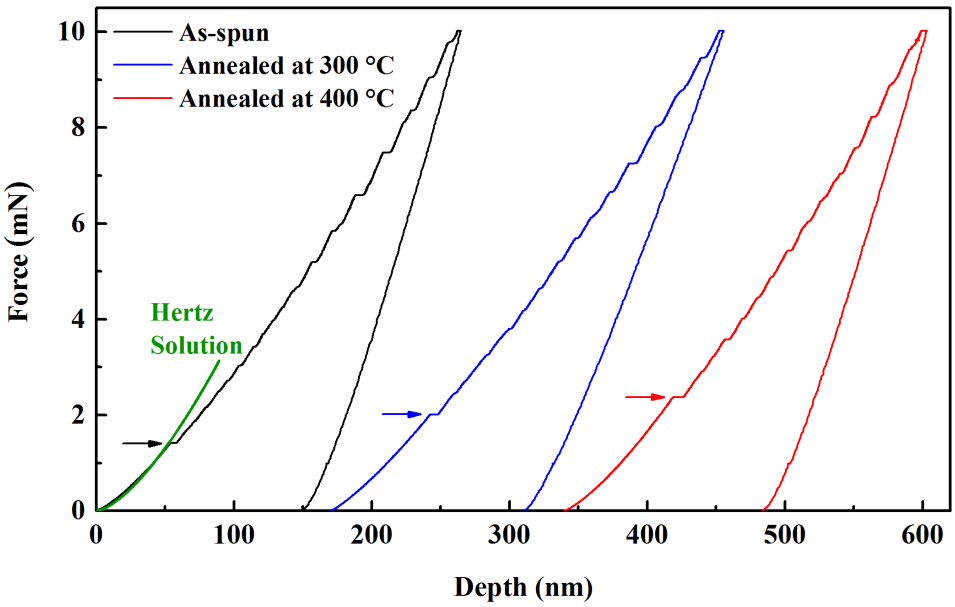

Figure 4.3: Force vs. penetration depth curves obtained from indentations with a spherical indenter on the as-spun and annealed $Ti_{40}Cu_{32}Pd_{14}Zr_{10}Sn_2Si_2$ specimens. Arrows mark the initial displacement burst for each curve. The prediction of the Hertz contact solution is also shown.

The force and displacement of the indenter corresponding to the initial displacement burst (F_d and Δh) for the as-spun and annealed specimens are summarized in Table 4.1. For 10 indentations, the average force values along with plus or minus one standard deviation and the minimum and maximum displacements corresponding to the initial displacement burst are reported. For the as-spun specimen, the initial displacement burst occurred at a force of 1481 μN and led to a displacement in the range of 1.9 - 4.4 nm. Annealing led to a systematic increase in the force at initial displacement burst and also a larger displacement of the indenter at the onset of plasticity. Similar observations have been reported for spherical indentations performed on a Zr-based MG, where annealing at $0.93T_g$ was seen to increase the force corresponding to the initial displacement burst [127]. In another study, annealing a Zr-based MG at $0.8T_g$ was reported to lead to the formation of more clearly defined displacement bursts compared to the as-spun specimen [124]. The annealing-induced increase in the force at initial displacement burst was attributed to the effect of free volume on the formation of STZs. The STZs are more likely to form in regions of high free volume and create a shear band along the critical shear stress direction [17,127]. Due to the larger amount of free volume available in the as-spun specimen, formation of STZs and thus initiation of shear bands occurred more readily compared to the annealed specimens. Annealing reduced the number of regions of high

Table 4.1: Force at initial displacement burst (F_d), displacement of the indenter during the initial displacement burst (Δh), and the PDE values for the as-spun and annealed $Ti_{40}Cu_{32}Pd_{14}Zr_{10}Sn_2Si_2$ specimens.

Specimen	F_d (μN)	Δh (nm)	PDE (10^{10} J/m^3)
As-spun	1481 ± 5%	1.9 - 4.4	1.08 ± 4%
Annealed at 300 °C	1966 ± 13%	1.9 - 5.7	1.13 ± 9%
Annealed at 400 °C	2340 ± 4%	3.9 - 7.2	1.18 ± 3%

free volume and thus made the formation of STZs more difficult. Therefore, initiation of shear bands was delayed [124, 127].

The values of force and displacement attributed to the initial displacement burst were used to calculate the PDE values for the as-spun and annealed specimens. The obtained PDE values are also reported in Table 4.1. For the as-spun specimen, a PDE value of 1.08×10^{10} J/m^3 was obtained. Annealing led to a slight increase in the PDE values, which can be interpreted as a reduction in the ductility of the specimens. Embrittlement of MGs due to annealing at temperatures below the glass transition temperature has been attributed to annihilation of free volume during structural relaxations [94, 95, 124, 126, 130, 131]. Due to the higher propensity for shear band initiation in the as-spun specimen, high stress concentration during deformation is mitigated by the relatively easy initiation and propagation of multiple smaller shear bands. On the other hand, shear band initiation is more difficult in the annealed specimens, which limits the plasticity and leads to localization of stress and lowers the ductility [124].

4.2 Effects of Ion Irradiation at Room Temperature [132]

Ion irradiation at 25 °C was performed on as-spun $Ti_{40}Cu_{32}Pd_{14}Zr_{10}Sn_2Si_2$ specimens with 4 MeV Fe^{2+} ions using a fluence of 1×10^{12}, 1×10^{13}, 1×10^{14}, and 1×10^{15} ions/cm^2. Figure 4.4 shows the depth profiles of the implanted Fe^{2+} ion concentration and irradiation damage in displacements per atom (dpa) for the specimen irradiated with a fluence of 1×10^{15} ions/cm^2, calculated using SRIM [98]. A default density of 7.2 g/cm^3 was used for the simulation. The concentration of implanted Fe^{2+} ions was negligible at depths below 0.5 μm and reached a maximum of ∼0.026 at.% around a depth of 1.5 μm. The simulation also predicted a maximum damage level of ∼1.8 dpa at a depth of ∼1.3 μm. The maximum concentration of implanted Fe^{2+} ions and damage level

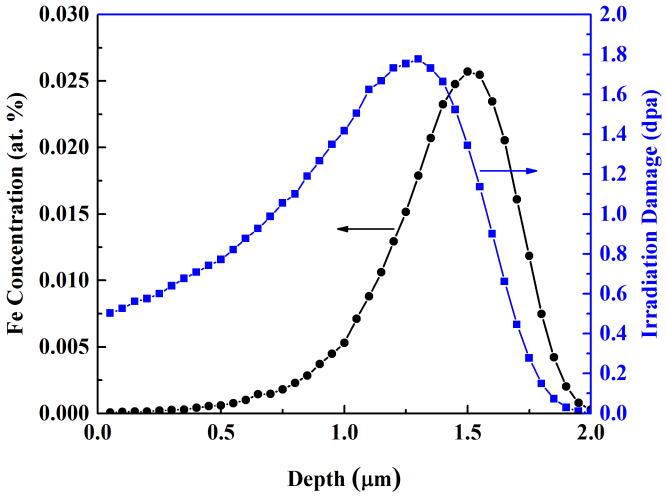

Figure 4.4: Depth profiles of implanted Fe^{2+} ion concentration and irradiation damage that resulted from irradiation with a fluence of 1×10^{15} ions/cm^2 in the as-spun $Ti_{40}Cu_{32}Pd_{14}Zr_{10}Sn_2Si_2$ specimen.

decreased linearly for specimens irradiated at lower fluences. Beyond the maxima, both the Fe^{2+} ion concentration and irradiation damage decreased and became negligible around a depth of 2 μm. The structure and mechanical response of the specimens were studied by XRD and nanoindentation.

4.2.1 Microstructural Evolution

Figure 4.5 shows the XRD patterns of the as-spun and irradiated specimens, where a broad diffraction pattern with no distinct crystalline peaks, characteristic of an amorphous phase, was observed in all the specimens. Finite element analysis of Myers et al. [86] demonstrated that irradiation-induced temperature rise in the core of the damage cascades can be high enough to locally melt the material. However, the quenching rate of the melted material is on the order of 10^{13} K/s, which is much faster than a typical cooling rate of $\sim 10^6$ K/s used for fabrication of MG ribbons [123]. Therefore, crystallization is inhibited regardless of the fluence used for irradiation.

4.2.2 Mechanical Response

Nanoindentation experiments with a Berkovich indenter were performed on the as-spun and irradiated specimens to measure their reduced elastic modulus and hardness. The loading sequence used for indentations consisted of loading to a maximum force of 10 mN at a loading rate of 0.33 mN/s, a 60 s hold at the maximum force to allow any time dependent plastic effects to diminish, 10 s unload-

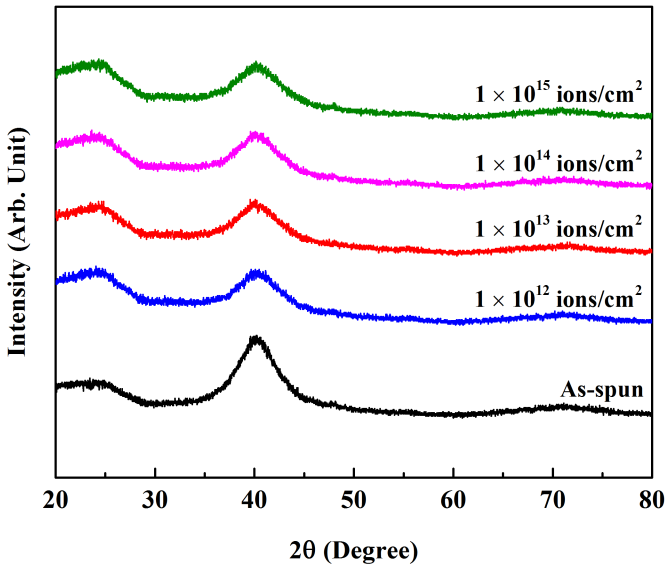

Figure 4.5: XRD patterns of the $Ti_{40}Cu_{32}Pd_{14}Zr_{10}Sn_2Si_2$ specimens before and after irradiation with Fe^{2+} ions at 25 °C using different fluences.

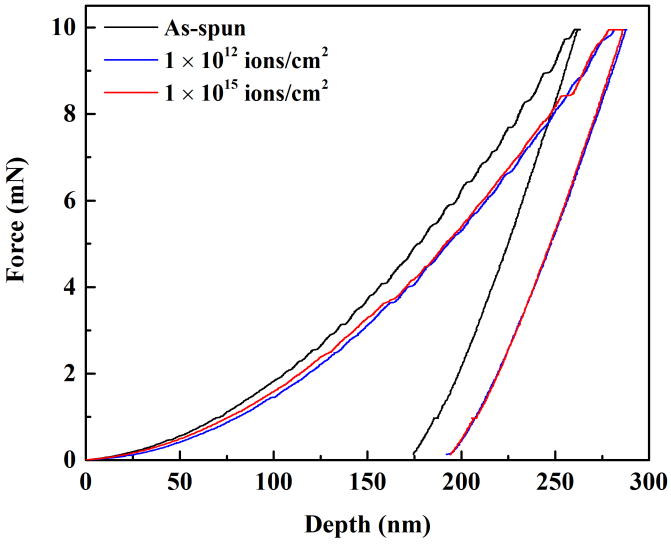

Figure 4.6: Force vs. penetration depth curves obtained from indentations with a Berkovich indenter on the $Ti_{40}Cu_{32}Pd_{14}Zr_{10}Sn_2Si_2$ specimens before and after irradiation with Fe^{2+} ions at 25 °C using different fluences.

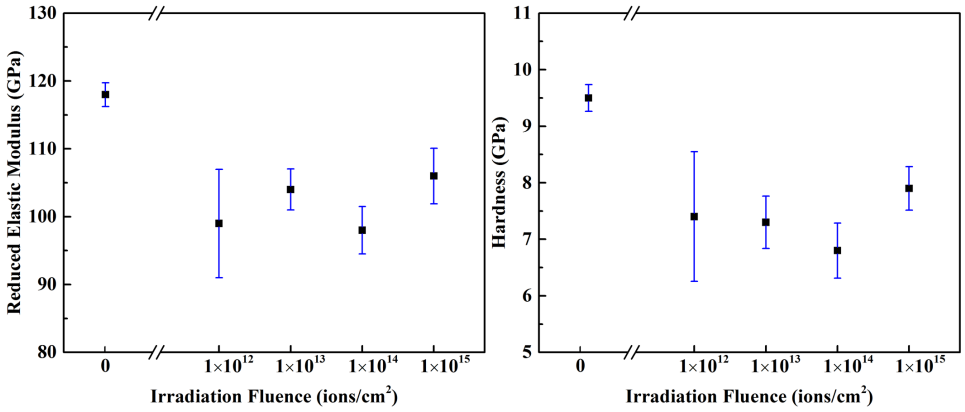

Figure 4.7: Reduced elastic modulus and hardness of the $Ti_{40}Cu_{32}Pd_{14}Zr_{10}Sn_2Si_2$ specimens before and after irradiation with Fe^{2+} ions at 25 °C using different fluences.

ing to 10% of the maximum force, a 60 s hold at 10% of the maximum force to measure thermal drift, and a 2 s final unloading. Figure 4.6 shows the typical force vs. penetration depth curves obtained for the as-spun specimen and those irradiated with a fluence of 1×10^{12} and 1×10^{15} ions/cm^2. The maximum penetration depth for the indentations (∼290 nm) was ∼15% of the projected range of the ions predicted by the SRIM simulations. This value is somewhat larger than the depth limit of 10% suggested for ensuring minimum influence from the material underneath the irradiated layer on nanoindentation results [133].

Figure 4.7 shows the reduced elastic modulus and hardness of the as-spun and irradiated specimens. Each data point is the average of 7 indentations and the error bars represent plus or minus one standard deviation. A reduced elastic modulus of 118 GPa and a hardness of 9.5 GPa were obtained for the as-spun specimen. These values are comparable to those reported in Section 4.1.1 for the same MG alloy. Ion irradiation at room temperature was seen to reduce both reduced elastic modulus and hardness. This is consistent with a study on the effects of ion irradiation of a Zr-based MG, where introduction of excess free volume resultant from irradiation was implicated as the cause for the reduction in elastic modulus [63]. A similar effect of excess free volume on hardness could also be expected.

To study the onset of plastic deformation, another set of nanoindentation experiments was performed with a spherical indenter. The loading sequence used for the spherical indentations consisted of loading to a maximum force of 10 mN at a loading rate of 0.05 mN/s, a 30 s hold at the maximum force to allow any time dependent plastic effects to diminish, 10 s unloading to 10% of the maximum force, a 30 s hold at 10% of the maximum force to measure thermal drift, and a 2 s final unloading.

Figure 4.8 shows the force vs. penetration depth curves obtained for the as-spun specimen and those irradiated with a fluence of 1×10^{12} and 1×10^{15} ions/cm^2. The curves have been offset for clarity and the initial displacement burst is marked by an arrow for each curve. For the as-spun specimen, a comparison between the force vs. penetration depth curve shown in Fig. 4.8 with that shown in Fig. 4.3 shows the displacement bursts were more clearly defined in the latter. The difference can be attributed to the slower loading rate used to obtain the force vs. penetration depth curves shown in Fig. 4.3 [112, 122]. According to Fig. 4.8, displacement bursts were observed for all the specimens, however they were more clearly defined for the as-spun specimen. The values obtained for the force and displacement at the initial displacement burst, and the PDE values for the as-spun and irradiated specimens are shown in Table 4.2. For 10 indentations, the average force values along with plus or minus one standard deviation and the minimum and maximum displacements corresponding to the initial displacement burst are reported. For the as-spun specimen, the first displacement burst occurred at an average force of 1014 μN. The irradiated specimens exhibited more variability in the force at which the first displacement burst occurred, however the average force values were significantly higher. The irradiated specimens were found to have slightly fewer displacement bursts and the length of the bursts was of similar length or shorter than those in the as-spun specimen. An average PDE value of 1.23×10^{10} J/m^3 was obtained for the as-spun specimen. The PDE value was seen to decrease with irradiation at 25 °C, which is consistent with an increase in ductility [118].

Table 4.2: Force at initial displacement burst (F_d), displacement of the indenter during the initial displacement burst (Δh), and the PDE values obtained for the $Ti_{40}Cu_{32}Pd_{14}Zr_{10}Sn_2Si_2$ specimens before and after irradiation with Fe^{2+} ions at 25 °C using different fluences.

Specimen	F_d (μN)	Δh (nm)	PDE (10^{10} J/m^3)
As-spun	1014 ± 3%	1.0 - 2.4	1.23 ± 4%
Irradiated with 1×10^{12} ions/cm^2	1056 ± 14%	0.8 - 1.4	1.15 ± 10%
Irradiated with 1×10^{13} ions/cm^2	2633 ± 28%	0.6 - 1.6	0.96 ± 7%
Irradiated with 1×10^{14} ions/cm^2	2218 ± 16%	0.5 - 1.3	0.91 ± 8%
Irradiated with 1×10^{15} ions/cm^2	2618 ± 17%	0.8 - 1.6	0.99 ± 5%

The effects of ion irradiation on deformation was further investigated by comparing the total amount of deformation that occurred during the displacement bursts ($h_{discrete}$) to residual pene-

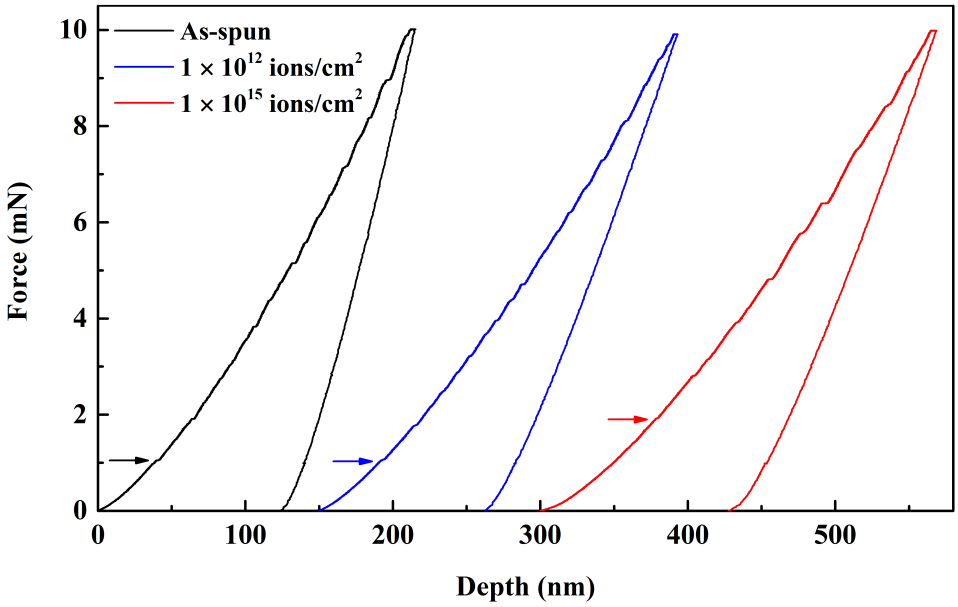

Figure 4.8: Force vs. penetration depth curves for spherical indentations performed on the $Ti_{40}Cu_{32}Pd_{14}Zr_{10}Sn_2Si_2$ specimens before and after irradiation with Fe^{2+} ion at 25 °C using different fluences. Arrows mark the initial displacement burst for each curve.

tration depth of the indenter after the removal of the test force (h_p) by calculating the ratio of the two values. For the as-spun specimen, the $h_{discrete}/h_p$ was found to be ~20%. After ion irradiation at 25 °C this ratio reduced to ≤12%, suggesting a transition in plastic flow from discrete (inhomogeneous) to continuous (homogeneous) [112, 119]. Hu et al. [134] studied a $Ti_{40}Zr_{25}Be_{30}Cr_5$ MG irradiated with C^{4+} and Cl^{4+} ions and found similar differences in the loading portion of the force vs. penetration depth curves. They attributed the differences to ion irradiation changing the formation and propagation of shear bands. It is plausible that a similar mechanism is involved for the Ti-based MG used in this study.

4.2.3 Post-Indentation AFM

Figure 4.9 shows the impressions made with a Berkovich indenter on the as-spun specimen and those irradiated with a fluence of 1×10^{13} and 1×10^{15} ions/cm^2. The scan area was 3×3 μm^2 and the height scale ranged from 220 to 420 nm. All specimens exhibited pile-up (i.e., material that is above the surrounding surface), however the nature of the pile-up was different for the as-spun specimen compared to the irradiated specimens. For the irradiated specimens, the pile-up was mostly confined to the edges of the indentation and did not extend much beyond the perimeter of the indent. For the as-spun specimen, the pile-up extended beyond the edges of the indentation in arcs around

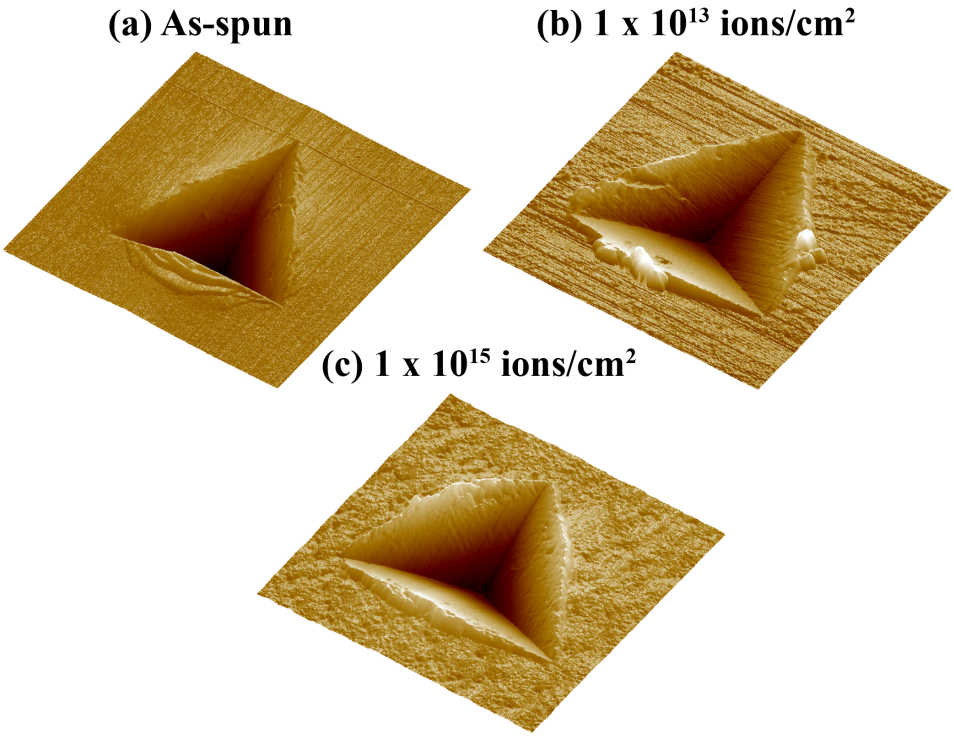

Figure 4.9: Atomic force microscopy images of residual impressions from indentations performed with a Berkovich indenter on the $Ti_{40}Cu_{32}Pd_{14}Zr_{10}Sn_2Si_2$ specimens before and after irradiation with Fe^{2+} ions at 25 °C using different fluences. All the scan areas are 3×3 μm^2 and the height scales are (a) 220 nm, (b) 420 nm, and (c) 280 nm.

the indentation. Furthermore, the piled-up material was mostly terrace-like with flat or slightly sloped top surfaces. Jiang and Atzmon [135] have seen similar features around deeper indentations, 1 μm depth at maximum force, in an Al-based MG, which they attributed to shear bands and the associated displacement bursts. This is consistent with the results of Figs. 4.8, where the irradiated specimens showed fewer displacement bursts than the as-spun specimen. It is also consistent with the irradiated specimens showing more homogeneous deformation.

An examination of the AFM image of the impression made on the as-spun specimen (Fig. 4.9(a)) showed that a majority of the shear band activity was confined to one edge of the impression, while the other two edges either showed sporadic shear band activity or none at all. This asymmetric shear band formation has been observed in our previous studies and those of others [124,135]. Therefore, it is unlikely that it has resulted from experimental artifacts such as, tapered surface of the specimen or misalignment of the indenter axis. It is believed that this asymmetry in deformation occurs because of the strain softening exhibited by MGs [124]. Formation of shear bands is associated with a net

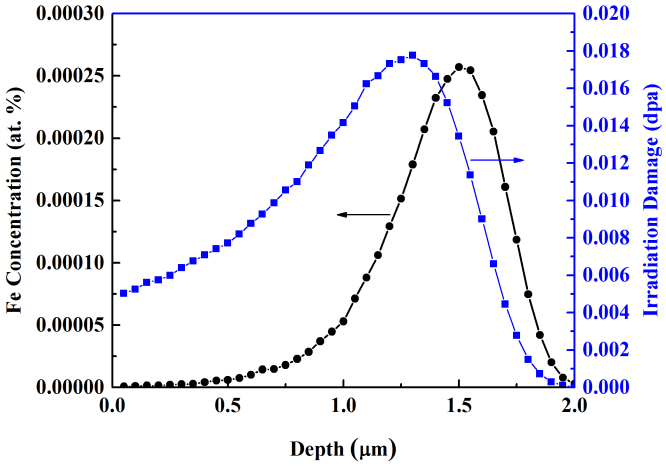

Figure 4.10: Depth profiles of implanted Fe^{2+} ion concentration and irradiation damage that resulted from irradiation with a fluence of 1×10^{13} ions/cm^2 in the as-spun $Ti_{40}Cu_{32}Pd_{14}Zr_{10}Sn_2Si_2$ specimen.

increase in free volume, which can induce strain softening [136, 137]. Therefore, once shear bands initiate on one side of the impression, they tends to localize in the vicinity of the same side due to strain softening.

4.3 Effects of Ion Irradiation at Elevated Temperatures - Below the Glass Transition Temperature [132]

To investigate the effects of concurrent annealing and irradiation, as-spun $Ti_{40}Cu_{32}Pd_{14}Zr_{10}Sn_2Si_2$ specimens were irradiated with 4 MeV Fe^{2+} ions at 25, 100, 200, and 300 °C using a fluence of 1×10^{13} ions/cm^2. Figure 4.10 shows the depth profiles of the implanted Fe^{2+} ion concentration and irradiation damage in dpa for the irradiated specimens, calculated using SRIM [98]. A default density of 7.2 g/cm^3 was used for the simulation. The concentration of implanted Fe^{2+} ions and damage level remained below ∼0.00026 at.% and ∼0.018 dpa, respectively within the projected range of the implanted ions. The structure and mechanical response of the specimens were studied by XRD and nanoindentation. The results presented for the as-spun specimen and the specimen irradiated at 25 °C are identical to those previously reported in Section 4.2.

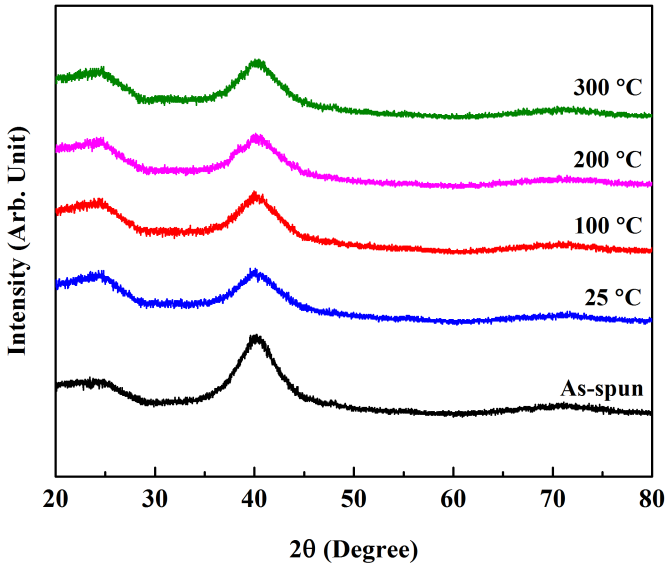

Figure 4.11: XRD patterns of the $Ti_{40}Cu_{32}Pd_{14}Zr_{10}Sn_2Si_2$ specimens before and after irradiation with Fe^{2+} ions at 25, 100, 200, and 300 °C using a fluence of 1×10^{13} ions/cm^2.

4.3.1 Microstructural Evolution

Figure 4.11 shows the XRD patterns of the as-spun and irradiated specimens, where no signs of crystallization is observed. This observation is consistent with the reports that below the glass transition temperature, crystallization is unlikely to occur within typical experimental time scales due to sluggish atomic movements [32, 94, 120, 138–142].

4.3.2 Mechanical Response

Figure 4.12 shows the typical force vs. penetration depth curves for the as-spun specimen and those irradiated at a temperature of 25 and 300 °C, obtained from indentations with a Berkovich indenter. The loading sequence used for indentations consisted of loading to a maximum force of 10 mN at a loading rate of 0.33 mN/s, a 60 s hold at the maximum force to allow any time dependent plastic effects to diminish, 10 s unloading to 10% of the maximum force, a 60 s hold at 10% of the maximum force to measure thermal drift, and a 2 s final unloading. The reduced elastic modulus and hardness values, obtained from the analysis of the Berkovich indentations, are shown in Fig. 4.13. Each data point is the average of 7 indentations and the error bars represent plus or minus one standard deviation. Ion irradiation at room temperature resulted in a reduction in reduced elastic modulus and hardness. However, both reduced elastic modulus and hardness increased monotonically with increasing the irradiation temperature. At higher irradiation temperatures investigated, the irradiated

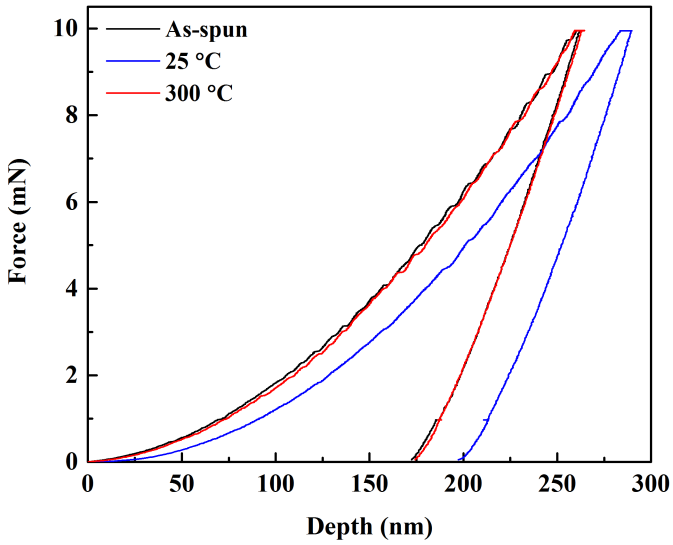

Figure 4.12: Force vs. penetration depth curves obtained from indentations with a Berkovich indenter on the $Ti_{40}Cu_{32}Pd_{14}Zr_{10}Sn_2Si_2$ specimens before and after irradiation with Fe^{2+} ions at 25 and 300 °C using a fluence of 1×10^{13} ions/cm^2.

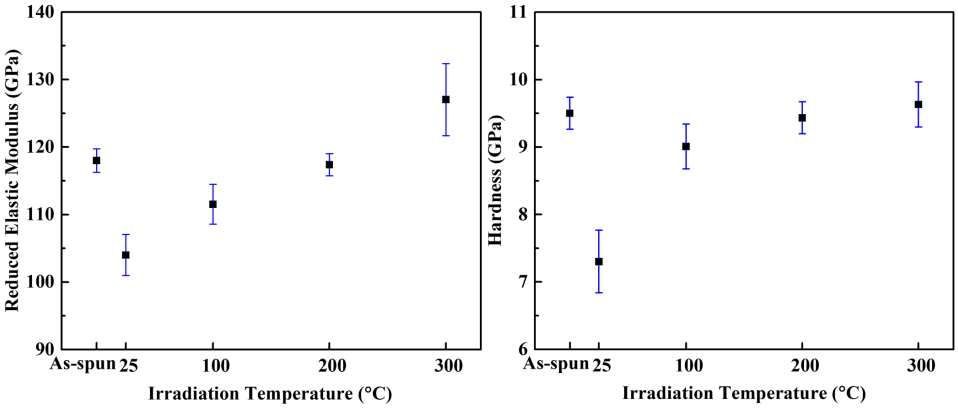

Figure 4.13: Reduced elastic modulus and hardness of the $Ti_{40}Cu_{32}Pd_{14}Zr_{10}Sn_2Si_2$ specimens before and after irradiation with Fe^{2+} ions at 25, 100, 200, and 300 °C using a fluence of 1×10^{13} ions/cm^2.

specimens were found to exhibit mechanical properties comparable to the as-spun specimen. While ion irradiation has been reported to lead to the introduction of excess free volume [63], heating a MG below its glass transition temperature is believed to result in annihilation of free volume [143]. As a result, annealing could reduce the effect of irradiation on reduced elastic modulus and hardness.

Table 4.3: Force at initial displacement burst (F_d), displacement of the indenter during the initial displacement burst (Δh), and the PDE values obtained for the $Ti_{40}Cu_{32}Pd_{14}Zr_{10}Sn_2Si_2$ specimens before and after irradiation with Fe^{2+} ions at 25, 100, 200, and 300 °C using a fluence of 1×10^{13} ions/cm^2.

Specimen	F_d (μN)	Δh (nm)	PDE (10^{10} J/m^3)
As-spun	1014 ± 3%	1.0 - 2.4	1.23 ± 4%
Irradiated at 25 °C	2633 ± 28%	0.6 - 1.6	0.96 ± 7%
Irradiated at 100 °C	871 ± 40%	0.5 - 1.2	0.91 ± 13%
Irradiated at 200 °C	1025 ± 34%	0.5 - 2.0	0.89 ± 5%
Irradiated at 300 °C	1820 ± 9%	1.7 - 5.4	1.14 ± 5%

To accentuate the displacement bursts visible in Fig.4.12, indentations were repeated on the as-spun and irradiated specimens with a spherical indenter. The loading sequence used for the spherical indentations consisted of loading to a maximum force of 10 mN at a loading rate of 0.05 mN/s, a 30 s hold at the maximum force to allow any time dependent plastic effects to diminish, 10 s unloading to 10% of the maximum force, a 30 s hold at 10% of the maximum force to measure thermal drift, and a 2 s final unloading. The values obtained for the force and displacement at the initial displacement burst, and the PDE values for the as-spun and irradiated specimens are shown in Table 4.3. For 10 indentations, the average force values along with plus or minus one standard deviation and the minimum and maximum displacements corresponding to the initial displacement burst are reported. The irradiated specimens exhibited more variability in the force at initial displacement burst as well as the PDE values. However, the average PDE values for the specimens irradiated at 25, 100, and 200 °C were lower than the as-spun specimen, which suggests an increase in ductility [118]. By further increasing the irradiation temperature to 300 °C, the PDE value increased and became comparable to that of the as-spun specimen suggesting a comparable ductility for these two specimens.

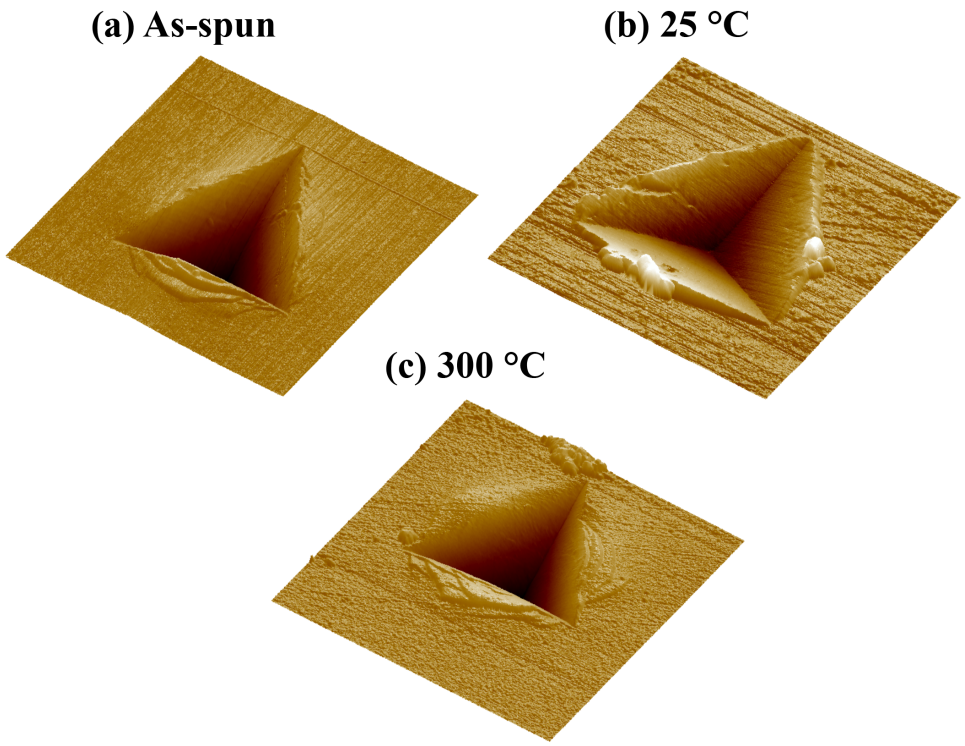

Figure 4.14: Atomic force microscopy images of residual impressions from indentations performed with a Berkovich indenter on the $Ti_{40}Cu_{32}Pd_{14}Zr_{10}Sn_2Si_2$ specimens before and after irradiation with Fe^{2+} ions at 25 and 300 °C using a fluence of 1×10^{13} ions/cm^2. All the scan areas are 3×3 μm^2 and the height scales are (a) 220 nm, (b) 420 nm, and (c) 210 nm.

4.3.3 Post-Indentation AFM

To better understand the deformation mechanisms at work, an examination of the area around the indentations performed with a Berkovich indenter was undertaken using AFM. Figure 4.14 shows the impressions made with a Berkovich indenter on the as-spun specimen and those irradiated at 25 and 300 °C. The scan area was 3×3 μm^2 and the height scale ranged from 210 to 420 nm. The nature of the pile-up seemed to be similar for the as-spun specimen and the specimen irradiated at 300 °C, where the pile-up extended beyond the edges of the indentation in terrace-like arcs. This observation, in addition to the comparable reduced elastic modulus, hardness, and ductility of the as-spun specimen and the specimen irradiated at 300 °C, suggests a similar deformation mechanism for these two specimens.

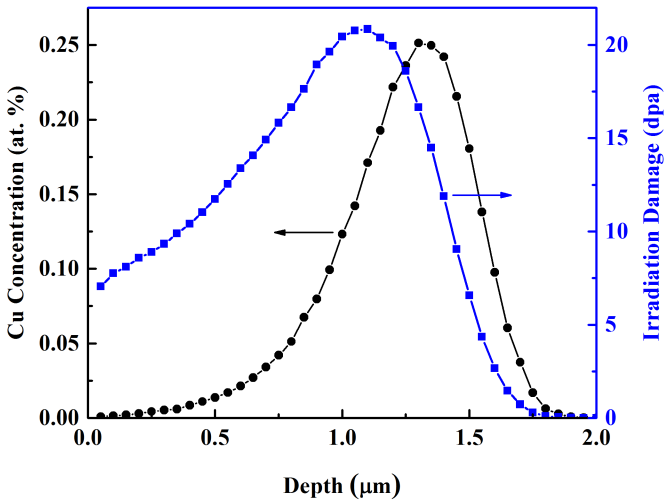

Figure 4.15: Depth profiles of implanted Cu^{2+} ion concentration and irradiation damage that resulted from irradiation with a fluence of 1×10^{16} ions/cm^2 in the as-spun $Ti_{40}Cu_{31}Pd_{14}Zr_{10}Sn_2Si_3$ specimen.

4.4 Effects of Ion Irradiation at Elevated Temperature - Below and Above the Glass Transition Temperature

For this study, as-spun $Ti_{40}Cu_{31}Pd_{14}Zr_{10}Sn_2Si_3$ specimens were irradiated using 3.5 MeV Cu^{2+} with a fluence of 1×10^{16} ions/cm^2 over a range of temperatures: (1) 100, 200, 250, 300, and 390 °C (below the glass transition temperature) and (2) at 480 (above the glass transition temperature, but below the crystallization temperature). Figure 4.15 shows the depth profiles of implanted Cu^{2+} ion concentration and irradiation damage in dpa for the irradiated specimens, calculated using SRIM [98]. A default density of 7.1 g/cm^3 was used for the simulation. The concentration of implanted Cu^{2+} ion was negligible at depths below 0.5 μm and reached a maximum of ~0.25 at.% around a depth of 1.3 μm. The simulation also predicted a maximum damage level of ~20 dpa at a depth of ~1.1 μm. Beyond the maxima, both Cu^{2+} ion concentration and irradiation damage decreased and became negligible around a depth of 1.7 μm. The structure of the specimens was studied by TEM. Nanoindentation experiments were performed on the specimen irradiated at 300 °C and the results are reported in Section 4.5.2.

4.4.1 Microstructural Evolution

Figure 4.16(a) shows the cross-sectional TEM micrograph and the corresponding selected area diffraction (SAD) pattern of the as-spun specimen. The micrograph exhibits a uniform contrast

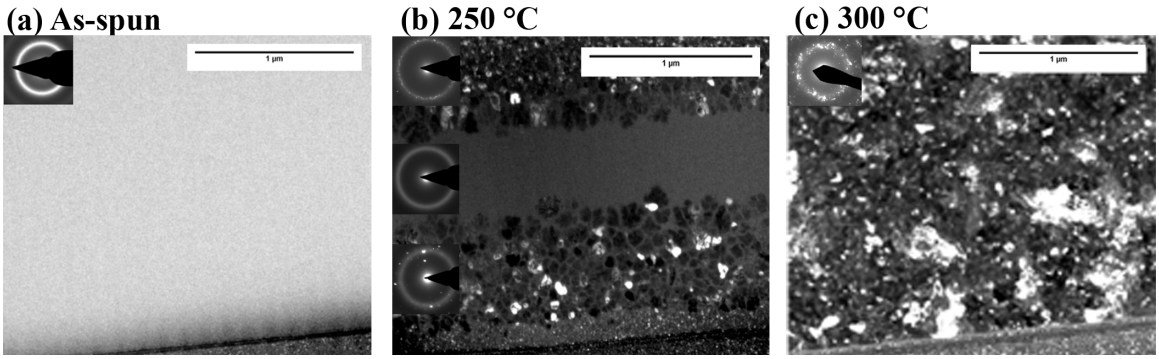

Figure 4.16: Cross-sectional TEM micrographs and corresponding SAD patterns of the $Ti_{40}Cu_{31}Pd_{14}Zr_{10}Sn_2Si_3$ specimens before and after irradiation with Cu^{2+} ions at 250 and 300 °C using a fluence of 1×10^{16} ions/cm^2. Surface of the specimen is at the bottom of the micrograph.

with no signs of crystallization or segregation. The SAD pattern also shows a diffuse halo ring without any detectable diffraction spots. The amorphous nature of the as-spun specimen indicates that the FIB milling process used for the preparation of cross-sectional TEM specimens did not lead to crystallization. The TEM micrographs and SAD patterns of the specimens irradiated at 100 and 200 °C also showed an amorphous structure with no signs of crystallization [99].

The TEM micrograph of the specimen irradiated at 250 °C is presented in Fig. 4.16(b). The micrograph shows a multilayer structure where an amorphous layer, spanning depths of 810 - 1320 nm, is sandwiched between crystallized layers. The SAD pattern collected from the amorphous layer shows no signs of crystallization, while those collected from the adjacent layers show a ring with diffraction spots, confirming crystallization. Overlaying the depth profile of irradiation damage (obtained using SRIM) on the TEM micrograph of this specimen, as shown in Fig. 4.17, demonstrates that the regions where the amorphous layer formed correspond to an irradiation damage of $\geq$17 dpa. This suggests ion irradiation could delay the onset of crystallization at or near the depth corresponding to the peak of irradiation damage. Additionally, except for an $\sim$170 nm thick layer immediately beneath the surface, the crystals formed within the ion range are larger than those beyond the range of the implanted ions. Energy dispersive spectroscopy (EDS) measurements along the thickness of the specimen demonstrated C and O contamination, as well as lower Cu concentrations in the $\sim$170 nm thick layer immediately beneath the surface. The EDS results also showed variations in the chemical compositions of different crystals within the ion range [99], suggesting the formation of more than one crystalline phase.

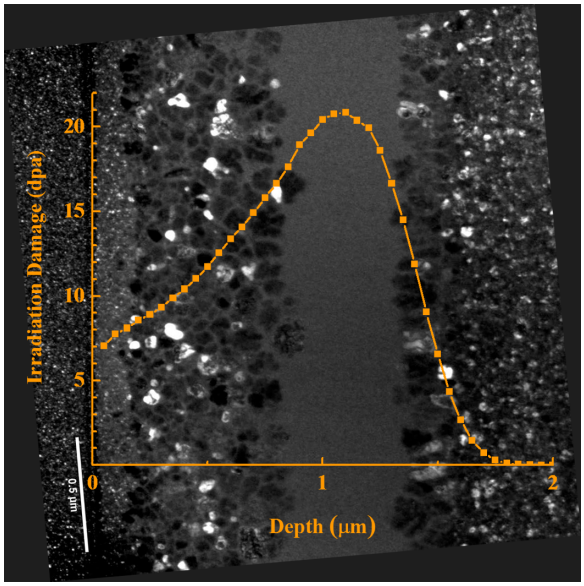

Figure 4.17: Cross-sectional TEM micrograph of the $Ti_{40}Cu_{31}Pd_{14}Zr_{10}Sn_2Si_3$ specimen irradiated with Cu^{2+} ions at 250 °C using a fluence of 1×10^{16} ions/cm^2 and the depth profile of irradiation damage. Surface of the specimen is at the left of the micrograph.

Figure 4.16(c) shows the cross-sectional TEM micrograph and the corresponding SAD pattern of the specimen irradiated at 300 °C. The micrograph indicates complete crystallization of the near-surface region with nanocrystalline domains that varied in size from tens to hundreds of nanometers. The SAD pattern shows multiple diffraction spots, which further confirms crystallization. Our TEM observations confirmed that this specimen is crystallized to a depth of ∼10 μm [99]. This specimen will henceforth be referred to as the fully crystallized specimen. Similar observations were also made for the specimens irradiated at 390 and 480 °C [99]. Several studies have reported on ion irradiation-induced crystallization of MGs [84–89]. Although details of the crystallization may be different in each study, enhanced atomic mobility is believed to be the general crystallization mechanism. During ion irradiation, formation of excess free volume in the core of the damage cascades leads to enhanced atomic mobility. Therefore, crystallization is possible where damage cascades are formed (i.e., within the ion range). However, extensive TEM studies of the fully crystallized specimen demonstrated that the crystallized region extended from the surface to depths beyond the ion range of 1.7 μm; therefore, ion irradiation alone was not the mechanism responsible for crystallization. At temperatures below the glass transition temperature, long-range atomic diffusion and thus crystallization are unlikely to occur within typical experimental time scales [32,94,120,138–142]; therefore, annealing the specimen at 300 °C ($\sim 0.7T_g$) is unlikely to result in crystallization. A

plausible explanation for the crystallization of the specimen is ion beam heating. Irradiation with energetic ions can induce localized heating in the target. Depending on the beam power density and target thermal properties, the magnitude of ion beam heating can vary from a few to hundreds of °C [91, 144–148]. In the present study, the specimens were glued from both ends to a filament-heated stage. A thermocouple was mechanically attached to the stage and its temperature readings were used as feedback in the control of the filament current in order to automatically control the stage temperature. Throughout the irradiations, the thermocouple recorded temperature fluctuations of $\leq$10 °C. However, when beam heating occurs the thermocouple will not measure the increase in specimen temperature since it is not mounted directly on the surface of the specimen [144]. As a result, the temperature of the specimen was higher than the desired temperature of 300 °C, which resulted in mass crystallization. Ion beam heating will be discussed in more details in Section 4.6.1.

4.5 Effects of Ion Irradiation at Elevated Temperature Followed by Ion Irradiation at Room Temperature

As seen in Section 4.4, ion irradiation above a critical temperature leads to complete crystallization in the near-surface region to depths beyond the range of the implanted ions. This study investigates the possibility of creating a partially crystallized structure by subjecting such a fully crystallized structure to a second step irradiation at room temperature. In an attempt to create partially crystallized structures, as-spun $Ti_{40}Cu_{31}Pd_{14}Zr_{10}$ Sn_2Si_3 specimens were irradiated with 3.5 MeV Cu^{2+} ions at 300 °C using a fluence of 1×10^{16} ions/cm^2 to induce crystallization. Subsequently, the crystallized specimens were irradiated again with 3.5 MeV Cu^{2+} ions at 25 °C using a fluence of 1×10^{14}, 1×10^{15}, and 1×10^{16} ions/cm^2. The structure and mechanical response of the specimens were studied by TEM and nanoindentation.

4.5.1 Microstructural Evolution

Figure 4.18 shows the cross-sectional TEM micrographs and the corresponding SAD patterns of the as-spun and fully crystallized specimens and those subjected to a subsequent irradiation at 25 °C. The micrographs shown in Figs. 4.18(a) and (b) are identical to those shown in Fig. 4.16. Irradiation of the fully crystallized specimen with a fluence of 1×10^{14} and 1×10^{15} ions/cm^2 results in re-amorphization in the near-surface region. The re-amorphized region extends from the surface to a depth of $\sim$1.6 μm, which is comparable to the ion range. The SAD patterns collected from depths

smaller than 1.6 μm show only a diffuse halo ring, while those collected from depths larger than 1.6 μm show a ring with diffraction spots. By increasing the irradiation fluence to 1×10^{16} ions/cm^2, the fully crystallized specimen transforms into a partially crystallized structure in the near-surface region. The TEM micrograph of the partially crystallized specimen (Fig. 4.18(e)) shows the presence of nanocrystals 10 - 80 nm in diameter embedded in an amorphous matrix. Ion irradiation-induced amorphization has been reported in various materials [91, 105, 149] and is typically described by two general models: defect accumulation and direct-impact. Based on the defect accumulation model, amorphization is possible when the rate of defect generation exceeds that of defect annihilation. When the overall density of defects reaches a threshold, the crystalline structure transforms into an amorphous structure [103, 150, 151]. According to this model, the concentration and mobility of point defects play an essential role in amorphization. Increasing the irradiation fluence creates a higher damage level and therefore should facilitate re-amorphization [102–104, 150]. However, our experimental observations were not consistent with the predictions of this model, since after increasing the irradiation fluence from 1×10^{14} to 1×10^{16} ions/cm^2 complete re-amorphization in the near-surface region was not observed. According to the direct-impact model, amorphization is a result of localized melting and rapid quenching of the melted material in the core of the damage cascades. Finite element analysis of MGs irradiated with energetic ions have demonstrated that cooling rates of the melted material in the core of a damage cascade are on the order of 10^{13} K/s [86]. This is much faster than a typical cooling rate of 10^6 K/s used for the fabrication of MG ribbons [123]. As a result, direct amorphization takes place in the core of a damage cascade. As the irradiation fluence increases, the individual damage cascades overlap [90, 91]. It is postulated that overlapping of the damage cascades results in accumulated heating of the melted material and thus reduces its temperature gradient with the surrounding material. The prolonged heating and slower cooling rate may facilitate crystallization in the region of overlapped damage cascades. The predictions based on the direct impact model appear to be in agreement with our experimental observations, where complete amorphization was inhibited by increasing the irradiation fluence from 1×10^{14} to 1×10^{16} ions/cm^2. Further investigation is required to confirm this.

4.5.2 Mechanical Response

Nanoindentation experiments with a Berkovich indenter were performed on the the as-spun and fully crystallized specimens and those subjected to a subsequent irradiation at 25 °C to measure their reduced elastic modulus and hardness. The loading sequence used for indentations consisted

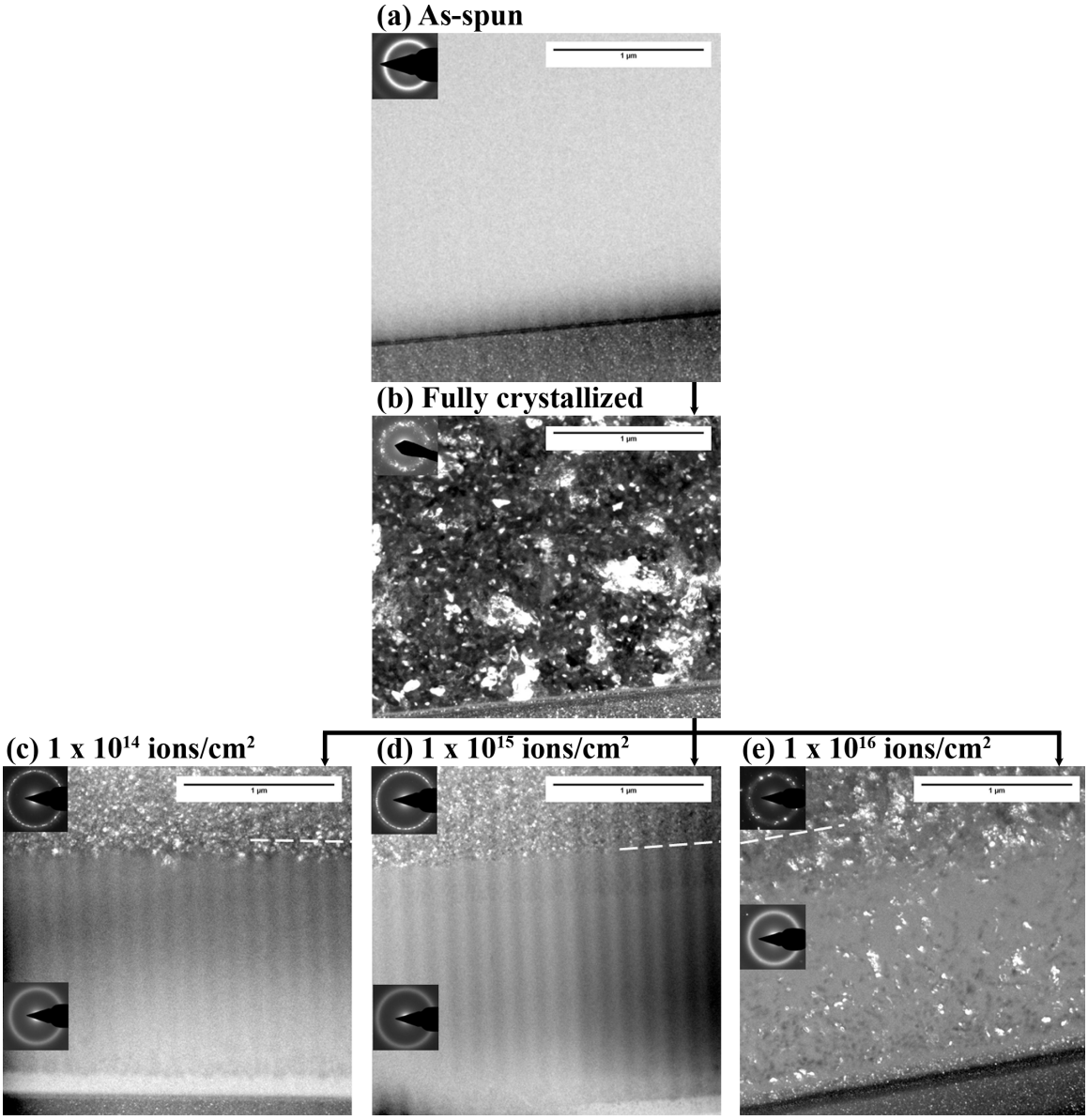

Figure 4.18: Cross-sectional TEM micrographs and corresponding SAD patterns of the $Ti_{40}Cu_{31}Pd_{14}Zr_{10}Sn_2Si_3$ specimens before and after irradiation with Cu^{2+} ions. Surface of the specimen is at the bottom of the micrograph. The range of implanted ions is marked by a dashed line for the specimens irradiated at 25 °C.

of loading to a maximum force of 4 mN at a loading rate of 0.13 mN/s, a 60 s hold at the maximum force to allow any time dependent plastic effects to diminish, 10 s unloading to 10% of the maximum force, a 60 s hold at 10% of the maximum force to measure thermal drift, and a 2 s final unloading. The solid curves shown in Fig. 4.19 are the typical force vs. penetration depth curves obtained for the as-spun specimen and those irradiated at 25 °C. The force vs. penetration depth curve for the fully crystallized specimen is not shown since it did not exhibit shear band activity. Multiple displacement bursts (serrations) were observed in the loading portion of the force vs. penetration depth curves. Displacement bursts are observed for all the specimens shown in Fig. 4.19, however they are greater in number and more clearly defined for the as-spun specimen. The effects of ion irradiation on shear band activity was further investigated by considering the total amount of deformation that occurred during the displacement bursts. Plotted with each original force vs. penetration depth curve in Fig. 4.19 is a dashed curve with the displacement bursts removed, which shifts the curve to the left. The sum of the displacement bursts, which is the total plastic deformation caused by shear bands ($h_{discrete}$), was compared to the residual penetration depth of the indenter after the removal of the test force (h_p) by calculating the ratio of the two values. This ratio, expressed as a percentage, is shown in Fig. 4.19. For the as-spun specimen, the $h_{discrete}/h_p$ was ∼27%. Ion irradiation at 25 °C reduced this value to ∼7%. This is an indication of a transition in plastic flow from discrete (inhomogeneous) in the as-spun specimen to relatively continuous (homogeneous) in the specimens irradiated at 25 °C [112, 119, 121].

The relatively homogenous plastic deformation of the specimens irradiated with a fluence of 1×10^{14} and 1×10^{15} ions/cm^2, which were fully amorphous within the ion range, can be explained by considering the influence of free volume on shear band activity where regions of higher free volume can more readily accommodate local shear [17]. Because the cooling rate during re-amorphization is higher than that during melt spinning, it is possible for the re-amorphized structures to have a greater amount of free volume compared to the as-spun specimen [152, 153]. Consequently, the number of shear bands that operate simultaneously is also higher in the re-amorphized structures. When a large number of shear bands operate simultaneously, the contribution of each one to the total plastic deformation is small. Therefore, displacement bursts and slip steps become less pronounced and macroscopic plastic flow is more homogenous [120, 121, 135, 135]. Similar observations were reported in Section 4.2.2 where $Ti_{40}Cu_{32}Pd_{14}Zr_{10}Sn_2Si_2$ specimens irradiated at 25 °C showed a tendency towards more homogeneous plastic deformation. For the specimen irradiated with a fluence of 1×10^{16} ions/cm^2, which was partially crystallized within the ion range, the effects of secondary-phase particles on shear band activity should also be considered. For a composite consisting of

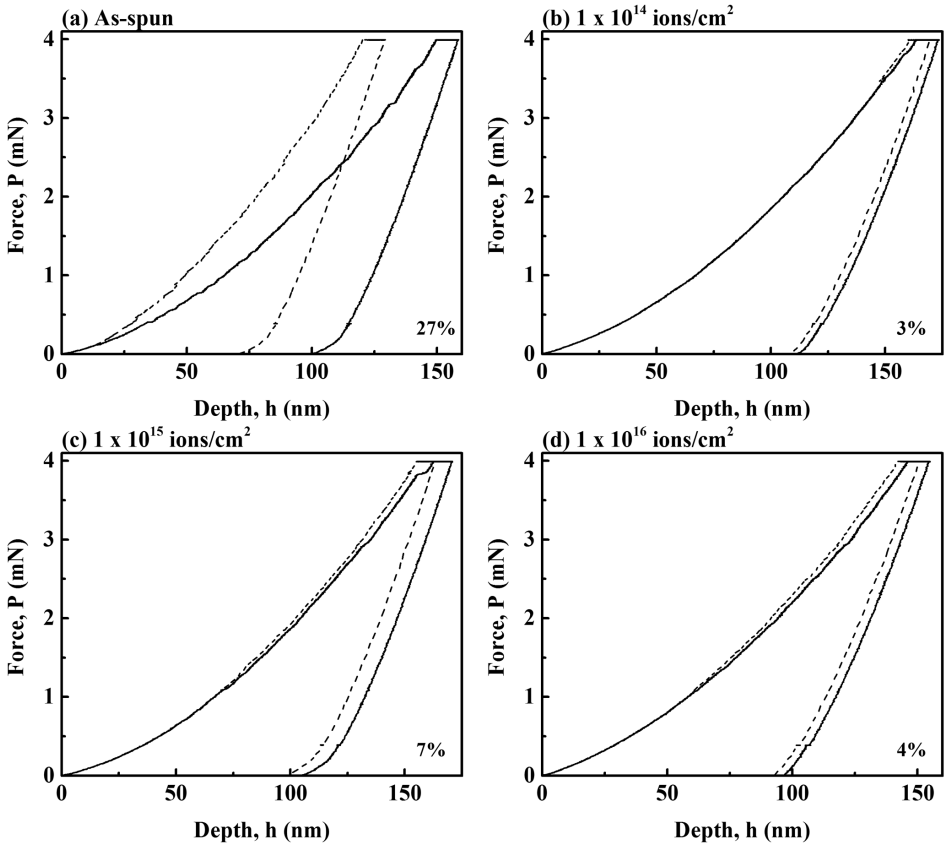

Figure 4.19: Original force vs. penetration depth curves (shown in solid) and the same curves with the displacement bursts removed (shown in dashed line) for the as-spun $Ti_{40}Cu_{31}Pd_{14}Zr_{10}Sn_2Si_3$ specimen and those irradiated with Cu^{2+} ions at 25 °C using different fluences.

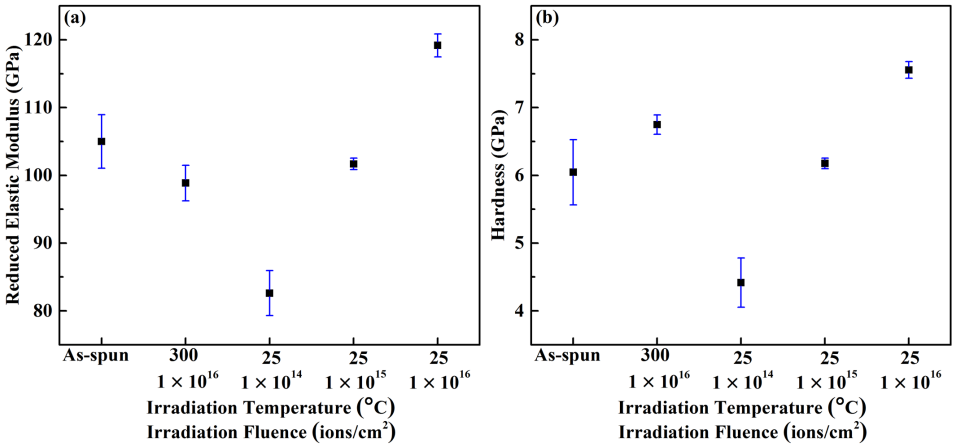

Figure 4.20: Reduced elastic modulus and hardness of the $Ti_{40}Cu_{31}Pd_{14}Zr_{10}Sn_2Si_3$ specimens before and after irradiation with Cu^{2+} ions.

secondary-phase particles embedded in an amorphous MG matrix, differences between the elastic modulus, hardness, and thermal expansion coefficient of the particles and matrix could result in misfit strains, induce stress concentrations, and promote shear band formation [17, 35, 120]. This is a plausible explanation for the transition towards more homogenous plastic flow in the partially crystallized specimen. Our observations suggest that formation of secondary-phase particles as a result of ion irradiation with a fluence of 1×10^{16} ions/cm^2 can facilitate the distribution of applied strain over a large number of shear bands, instead of a few dominant ones.

The reduced elastic modulus and hardness of the specimens were calculated from nanoindentation experiments. Post-indentation AFM images of selected Berkovich indentations showed formation of pile-up around the edges of the impressions. These AFM images will be further discusses in Section 4.5.3. When pile-up is present, accurate measurements of the projected area cannot be obtained from the force vs. penetration depth curves by the commonly used Oliver and Pharr procedure [113]. Rather, indentations can be imaged to examine the extent of pile-up and establish the true projected area [114, 154]. Therefore, immediately after unloading, each indentation was scanned using the diamond indenter as a scanning probe tip. The true projected area was measured from the post-indentation SPM images using ImageJ software [155] following the method introduced by Sullivan and Prorok [156]. It is acknowledged that there may be some subjectivity in the method used for evaluating the true projected area. However, differences between the mechanical response of the as-spun and irradiated specimens can be attributed to the effects of irradiation.

Figure 4.20 shows the reduced elastic modulus and hardness of the as-spun and irradiated specimens, where each data point is the average of 10 indentations and the error bars represent plus or

minus one standard deviation. The maximum penetration depth for the indentations was ∼160 nm, which is ∼10% of the ion range. This ensured that the obtained reduced elastic modulus and hardness values represent the mechanical properties of the irradiated layer with minimum influence from the underlying material [133]. For the as-spun specimen, a reduced elastic modulus of 105 GPa and a hardness of 6.0 GPa were obtained. Accounting for pile-up in the analysis of the nanoindentation data resulted in reduced elastic modulus and hardness values that are smaller than those reported in Sections 4.1.1 and 4.2.2 for the as-spun $Ti_{40}Cu_{32}Pd_{14}Zr_{10}Sn_2Si_2$ MG alloy. Irradiation at 300 °C, which resulted in mass crystallization, led to in an ∼6% reduction in reduced elastic modulus, but an ∼11% increase in hardness. Studies on fully crystallized MG specimens created by annealing have reported an increased reduced elastic modulus and hardness due to free volume annihilation and a subsequent increase in density [32, 138, 140]. The underlying reasons for the decrease in the reduced elastic modulus of the fully crystallized specimen are unclear. Irradiation at 25 °C with a fluence of 1×10^{14} ions/cm^2 resulted in ∼21% reduction in reduced elastic modulus and ∼27% reduction in hardness compared to the as-spun specimen. A plausible explanation for the decrease in both reduced elastic modulus and hardness is an increased free volume content resultant from rapid cooling during re-amorphization [152, 157]. Increasing the irradiation fluence resulted in a monotonic increase in both reduced elastic modulus and hardness. For the partially crystallized specimen irradiated with a fluence of 1×10^{16} ions/cm^2, a reduced elastic modulus of 119.0 GPa and a hardness of 7.6 GPa were obtained. The increased reduced elastic modulus of the partially crystallized specimen can be attributed to the higher density and shorter average interatomic spacing of the crystalline phase compared to the amorphous phase [17, 85, 125]. According to Lund and Schuh [158], the interaction of shear bands with nanocrystals depends on the size of the nanocrystals relative to the shear band thickness. Nanocrystals that are larger than the shear band thickness have the potential to disrupt the shear bands even if they exist in small volume fractions [159–161]. According to the TEM studies, the nanocrystals in the partially crystallized specimen were 10 - 80 nm in diameter. This is in comparison to a typical shear band thickness of 10 - 20 nm suggested for MG ribbons [162, 163], which demonstrates that disruption of shear bands by nanocrystals is plausible in the partially crystallized specimen. Therefore, increased hardness of the partially crystallized specimen can be attributed to suppression of shear band propagation by nanocrystals.

To compare the ductility of the as-spun specimen with that of the partially crystallized specimen, another set of nanoindentation experiments was performed using a spherical indenter. The loading sequence used for these indentations were identical to that used for the Berkovich indentations except for a loading rate of 0.03 mN/s. For 10 indentations, an average PDE value of $(1.09 \pm 0.03) \times$

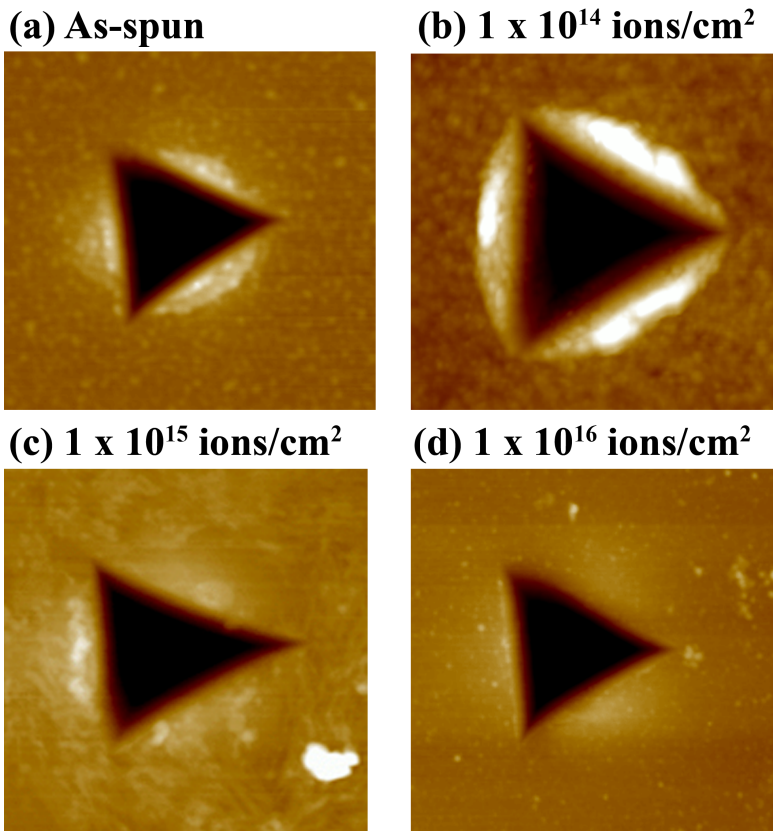

Figure 4.21: Top view atomic force microscopy images of residual impressions from indentations performed with a Berkovich indenter on the $Ti_{40}Cu_{31}Pd_{14}Zr_{10}Sn_2Si_3$ specimens before and after irradiation with Cu^{2+} ions at 25 °C. All the scan areas are 2×2 μm^2 and the height scales are 100 nm.

10^{10} J/m^3 was obtained for the as-spun specimen. The PDE value of the partially crystallized specimen was fount to be $(1.21 \pm 0.21) \times 10^{10}$ J/m^3. The larger standard deviation of the partially crystallized specimen, which was attributed to the inhomogeneous distribution of nanocrystals within the amorphous matrix, made it difficult to make a comparison between the ductility of the two specimens.

4.5.3 Post-Indentation AFM

Figure 4.21 shows AFM images of the impressions made with a Berkovich indenter on the as-spun specimen and those irradiated at 25 °C. The scan area is 2×2 μm^2 and the height scale is 100 nm. All specimens exhibit pile-up, however the nature of pile-up changes after irradiation. For the as-spun specimen, slip steps are observed, where pile-up extended beyond the edges of the indentation in

relatively flat arcs around the impressions. Slip steps were not observed for the specimens irradiated at 25 °C and pile-up is mostly confined to the edges of the impressions. By increasing the irradiation fluence from 1×10^{14} to 1×10^{16} ions/cm^2, the height of pile up decreased from ∼50 nm to less than 10 nm. Slip steps have been observed in MGs deformed in constrained modes of loading and are associated with shear band formation [135,164,165]. The absence of slip steps for the specimens irradiated at 25 °C is consistent with the observations from Fig. 4.19, where irradiation led to more homogenous plastic deformation.

4.6 Additional Studies on the Effects of Ion Irradiation at Elevated Temperature

Based on our findings in Section 4.4, the microstructure of the specimens irradiated at elevated temperature was affected by ion beam heating. To resolve this issue, additional irradiations were performed at elevated temperature where the average beam current was kept below 125 nA. Ion beam heating is known to be directly proportional to the applied beam current [166]; therefore, using a relatively low beam currents is expected to minimize the magnitude of beam heating. In this study, as-spun $Ti_{40}Cu_{29}Pd_{14}Zr_{10}Sn_2Si_5$ specimens were irradiated using 3.5 MeV Cu^{2+} ions with a fluence of 1×10^{16} ions/cm^2 over a range of temperatures: (1) at 325, 385, 400, and 440 °C (below the glass transition temperature), (2) at 450 °C (equal to the glass transition temperature), and (3) at 460 and 480 °C (above the glass transition temperature, but below the crystallization temperature). The ion beam had a rectangular shape of 12×6.5 mm^2 and an average intensity of 5×10^{11} ions/cm^{2}s. Figure 4.22 shows the depth profiles of implanted Cu^{2+} ion concentration and irradiation damage in dpa for the irradiated specimens, calculated using SRIM [98]. A default density of 7.0 g/cm^3 was used for the simulation. The concentration of implanted Cu^{2+} ion was negligible at depths below 0.5 μm and reached a maximum of ∼0.25 at.% around a depth of 1.4 μm. The simulation also predicted a maximum damage level of ∼21 dpa at a depth of ∼1.1 μm. Beyond the maxima, both Cu^{2+} ion concentration and irradiation damage decreased and became negligible around a depth of 1.7 μm. The structure and mechanical response of the specimens were studied by TEM, XRD, and nanoindentation.

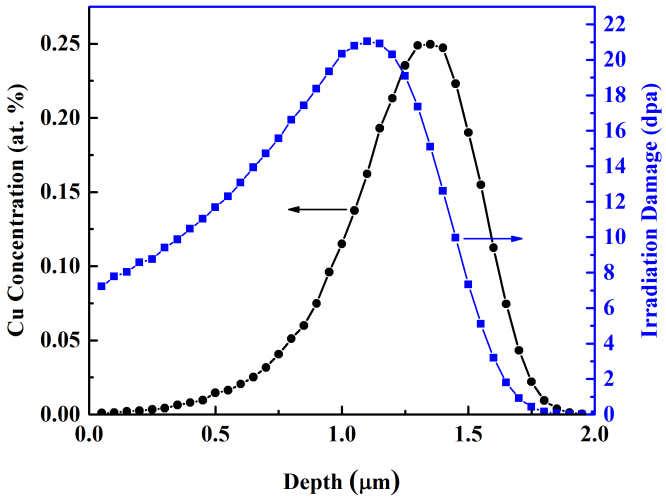

Figure 4.22: Depth profiles of implanted Cu^{2+} ion concentration and irradiation damage that resulted from irradiation with a fluence of 1×10^{16} ions/cm^2 in the as-spun $Ti_{40}Cu_{29}Pd_{14}Zr_{10}Sn_2Si_5$ specimen.

4.6.1 Microstructural Evolution

Figure 4.23 shows the cross-sectional TEM micrographs and corresponding SAD patterns of the as-spun specimen and those irradiated at 450, 460, and 480 °C. The TEM micrograph of the as-spun specimen (Fig. 4.23(a)) exhibits a uniform contrast with no signs of crystallization or segregation. The SAD pattern also shows a diffuse halo ring without any detectable diffraction spots. The TEM micrographs and SAD patterns of the specimens irradiated at 325, 385, 400, and 440 °C were similar to those of the as-spun specimen and showed no signs of crystallization. These observations are consistent with our previous studies reported in Section 4.3 and those of others [32, 94, 120, 138–142] that at temperatures below the glass transition temperature, long-range atomic diffusion and thus crystallization are not likely to occur within experimental time scales [32, 94, 120, 138–142].

Figure 4.23(b) shows the cross-sectional TEM micrograph and corresponding SAD patterns of the specimen irradiated at the glass transition temperature of 450 °C. While the specimen is amorphous within the range of the implanted ions (1.7 μm), crystallization is observed beyond the ion range. The SAD pattern collected from depths smaller than 1.7 μm shows only a diffuse halo ring, while that collected from depths larger than 1.7 μm shows a ring with diffraction spots. Higher magnification TEM micrographs of this specimen, presented in Fig. 4.24, show the presence of nanocrystals that are 5 - 20 nm in diameter beyond the range of the implanted ions.

As seen in Fig. 4.23(c), by increasing the irradiation temperature to 460 °C the thickness of the

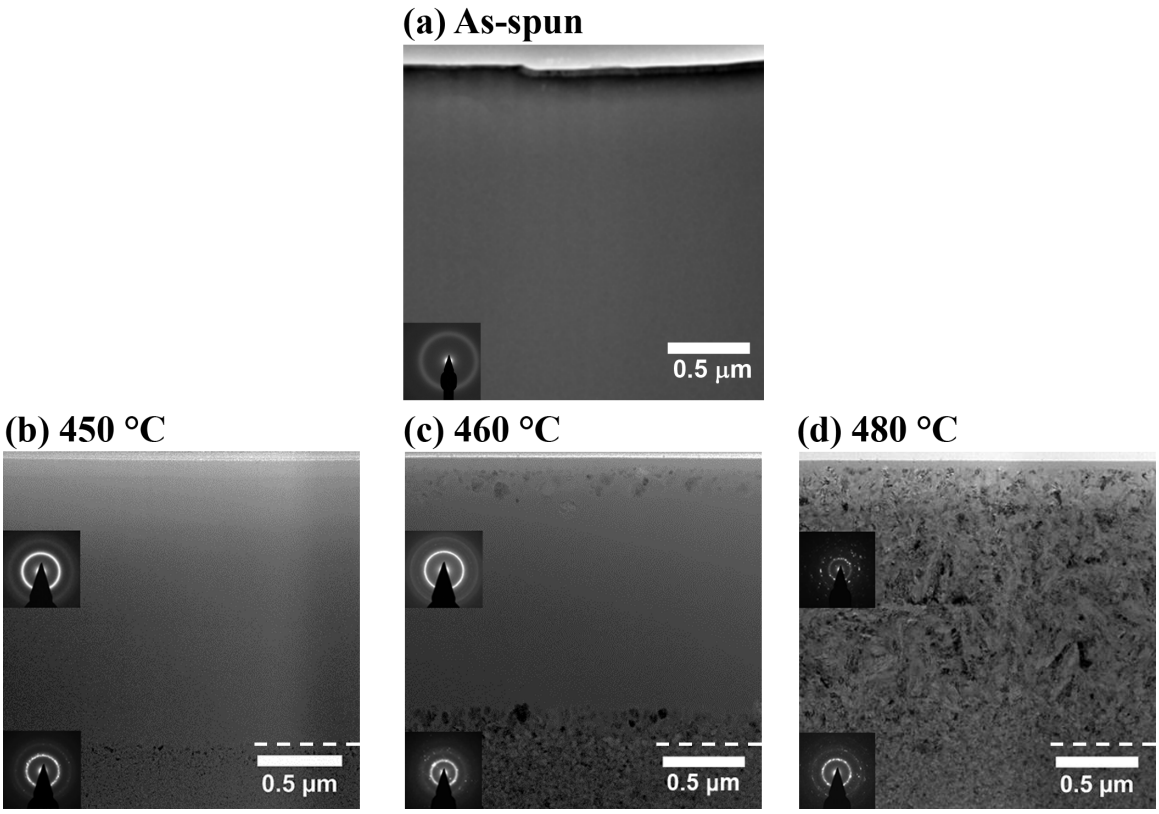

Figure 4.23: Cross-sectional TEM micrographs and corresponding SAD patterns of the $Ti_{40}Cu_{29}Pd_{14}Zr_{10}Sn_2Si_5$ specimens before and after irradiation with Cu^{2+} ions at 450, 460, and 480 °C using a fluence of 1×10^{16} ions/cm^2. Surface of the specimen is at the top of the micrograph. The range of implanted ions is marked by a dashed line for the irradiated specimens.

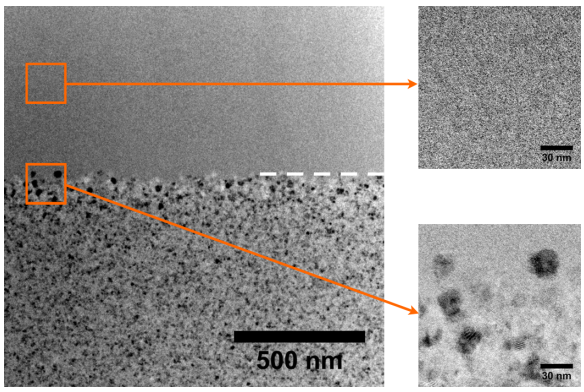

Figure 4.24: TEM micrographs of the $Ti_{40}Cu_{29}Pd_{14}Zr_{10}Sn_2Si_5$ specimen irradiated with Cu^{2+} ions at 450 °C. The dashed line approximately marks the range of the implanted ions.

amorphous layer decreases and a crystalline layer forms in the near-surface region. Further increase in irradiation temperature to 480 °C (Fig. 4.23(d)) results in crystallization of the specimen within and beyond the ion range. Figure 4.25 shows additional TEM micrographs of the fully crystallized specimen, which confirm mass crystallization. The crystals formed at depths smaller than 1.7 μm appear to be larger than those formed at deeper depths.

Figure 4.26 shows the XRD patterns of the as-spun and irradiated specimens. Consistent with the TEM observations, only a broad peak corresponding to an amorphous phase can be observed for the as-spun specimen and those irradiated at 325, 385, 400, and 450 °C. For the specimen irradiated at 460 °C, a sharp peak superimposed on the broad amorphous peak can be observed. After increasing the irradiation temperature to 480 °C, the broad amorphous peak is no longer observed and several sharp peaks appear. For the specimen irradiated at 480 °C, an XRD pattern with improved signal to noise ratio was obtained by increasing data collection time by an order of magnitude. The obtained XRD pattern is shown in Fig. 4.27 where peaks corresponding to face centered cubic (fcc) Cu, hexagonal $TiPd_3$, rhombohedral Zr_3Pd_4, and hexagonal Pd_3Zr crystalline phases are observed. This observation is again consistent with the TEM micrographs of this specimen (Figs. 4.23(d) and 4.25), which showed complete crystallization.

Similar to the findings reported in Section 4.4, our microstructural studies demonstrate that there is a critical temperature below which the specimen remains completely amorphous. When irradiation is performed at or near the critical temperature, areas that are beyond the ion range (i.e., not affected by ion irradiation) undergo crystallization, but those within the ion range remain entirely or partially amorphous. In other words, ion irradiation favors amorphization and delays the onset of

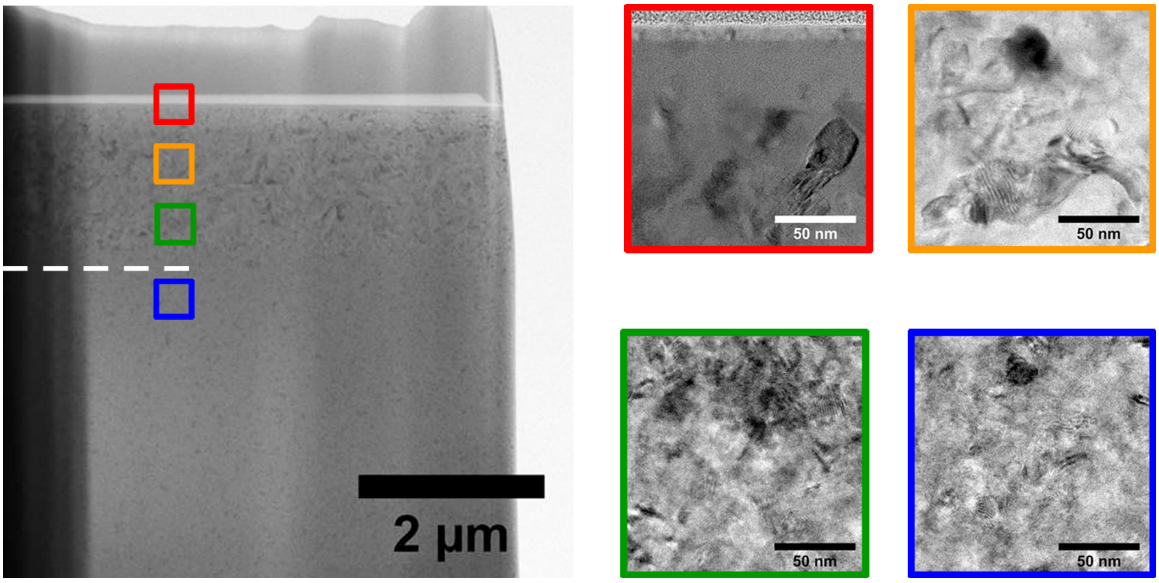

Figure 4.25: TEM micrographs of the $Ti_{40}Cu_{29}Pd_{14}Zr_{10}Sn_2Si_5$ specimen irradiated with Cu^{2+} ions at 480 °C. The dashed line marks the range of the implanted ions.

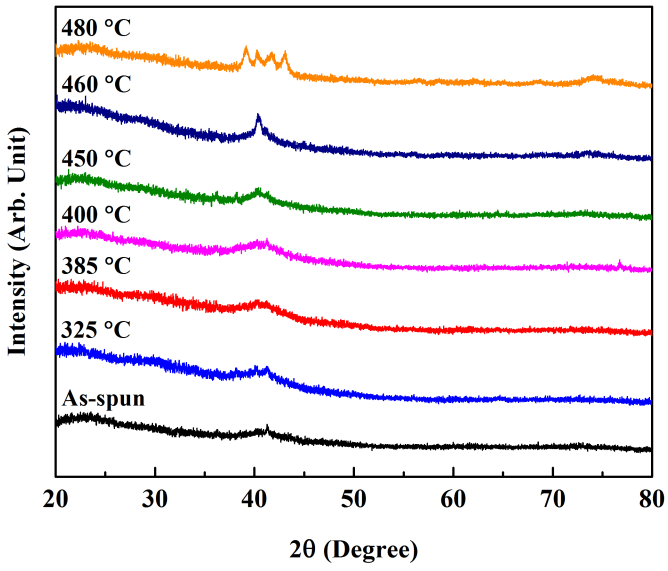

Figure 4.26: XRD patterns of the $Ti_{40}Cu_{29}Pd_{14}Zr_{10}Sn_2Si_5$ specimens before and after irradiation with Cu^{2+} ions using a fluence of 1×10^{16} ions/cm^2.

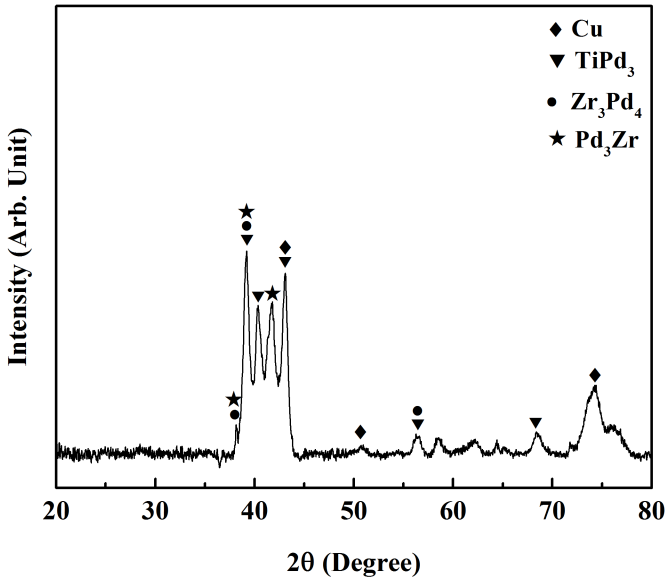

Figure 4.27: Higher resolution XRD pattern of the $Ti_{40}Cu_{29}Pd_{14}Zr_{10}Sn_2Si_5$ specimen irradiated with Cu^{2+} ions at 480 °C using a fluence of 1×10^{16} ions/cm^2.

crystallization. At temperatures higher than the critical temperature, annealing becomes dominant and complete crystallization takes place. Despite these similarities, the critical temperature in the present study ($\sim T_g$) was found to be considerably higher than that reported in Section 4.4 ($\sim 0.7T_g$)). A plausible explanation for this discrepancy is ion beam heating as discussed below.

Crespillo et al. [144] provided an analytical solution for the maximum temperature rise (ΔT_{max}) that resulted when an ion beam with a square cross section was incident on a semi-infinite target:

$$\Delta T_{max} < 0.561 \frac{\phi E l}{K} \tag{IV.2}$$

where ϕ and E are the beam intensity and energy, l is the width of the ion beam, and K is the thermal conductivity of the target. This analytical solution does not account for heat loss and assumes that the ion energy is deposited entirely as heat. To the best of our knowledge, no reports on the thermal conductivity of the $Ti_{40}Cu_{29}Pd_{14}Zr_{10}Sn_2Si_5$ MG alloy is available. Wang et al. [167] reported a thermal conductivity of 9.15 W/mK for a $Ti_{40}Zr_{25}Be_{20}Cu_{12}Ni_3$ MG alloy at 360 °C. Using this value as an estimate for the thermal conductivity of the as-spun specimen in the present study and assuming that the rectangular ion beam of 12×6.5 mm^2 is equivalent to a square beam of 8.8×8.8 mm^2, the maximum temperature rise was found to be <2 °C. This confirms that when beam heating is minimized, irradiation with 3.5 MeV Cu^{2+} ions using a fluence of 1×10^{16} ions/cm^2 does not lead to crystallization of the $Ti_{40}Cu_{29}Pd_{14}Zr_{10}Sn_2Si_5$ specimens. We are unable to provide a

quantitative evaluation of beam heating for the irradiations performed in Section 4.4 since the beam characteristics were not properly recorded. However, based on the findings of the present study, the temperature rise due to beam heating should have been at least 140 °C to raise the temperature to the glass transition and lead to mass crystallization in the specimen.

4.6.2 Mechanical Response

Nanoindentation experiments with a Berkovich indenter were performed on the the as-spun and irradiated specimens to measure their reduced elastic modulus and hardness. The loading sequence used for indentations consisted of loading to a maximum force of 4 mN at a loading rate of 0.13 mN/s, a 60 s hold at the maximum force to allow any time dependent plastic effects to diminish, 10 s unloading to 10% of the maximum force, a 60 s hold at 10% of the maximum force to measure thermal drift, and a 2 s final unloading. Figure 4.28 shows the typical force vs. penetration depth curves obtained for the as-spun and irradiated specimens. All force vs. penetration depth curves are plotted using the same y-axis scale. Therefore, shifts in the position of the curves can be interpreted as changes in hardness where higher hardness values shift the curve towards smaller indentation depths. A comparison between the force vs. penetration depth curves of the as-spun and irradiated specimens suggests a reduction in hardness after irradiation at 325, 385, or 400 °C, but an increase in hardness after irradiation at 450, 460, or 480 °C. Small displacement bursts are observed in the loading portion of the force vs. penetration depth curves of all the specimens, except the one irradiated at 480 °C. The absence of displacement bursts is believed to be due to a lack of shear band activity in this completely crystallized specimen.

Immediately after each indentation, the diamond indenter was used as a scanning probe tip to study the Berkovich impressions. Figure 4.29 shows post-indentation SPM images of the as-spun and irradiated specimens. As seen in Figs. 4.29(a) - (d), pile-up is observed for the as-spun specimen and those irradiated at 325, 385, or 400 °C. An average pile-up height of ∼15 nm is obtained for the as-spun specimen. After irradiation at 325, 385, or 400 °C, the average pile-up height increases to ∼30 nm. By contrast, after irradiation at 450, 460, and 480 °C no pile-up is observed (Figs. 4.29(e) - (g)). The post-indentation SPM images were used to obtain the true projected area following the Sullivan and Prorok method [156] using ImageJ software [155]. The obtained values of the true projected area were then used to measure the reduced elastic modulus and hardness of the specimens.

Figure 4.30 shows the reduced elastic modulus and hardness of the as-spun and irradiated spec-

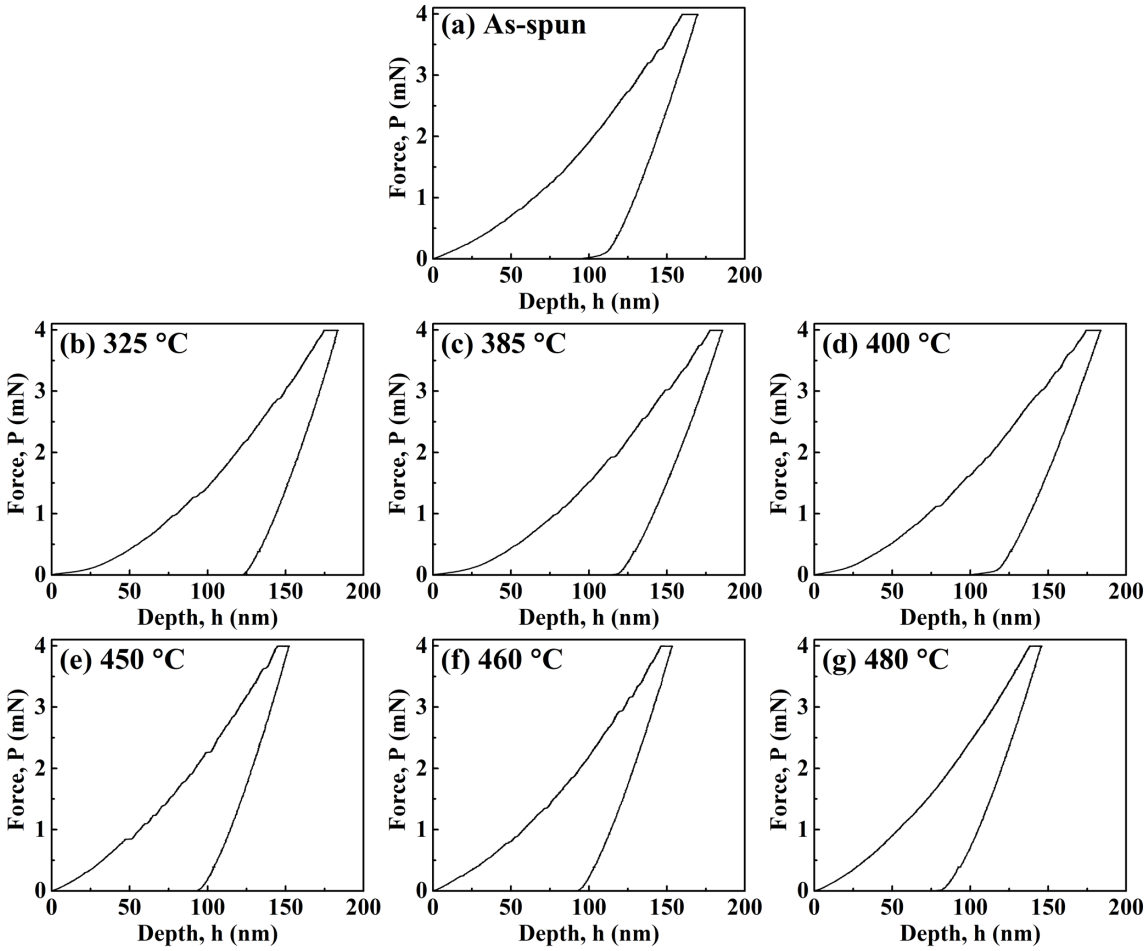

Figure 4.28: Force vs. penetration depth curves obtained from indentations with a Berkovich indenter on the $Ti_{40}Cu_{29}Pd_{14}Zr_{10}Sn_2Si_5$ specimens before and after irradiation with Cu^{2+} ions at different temperatures.

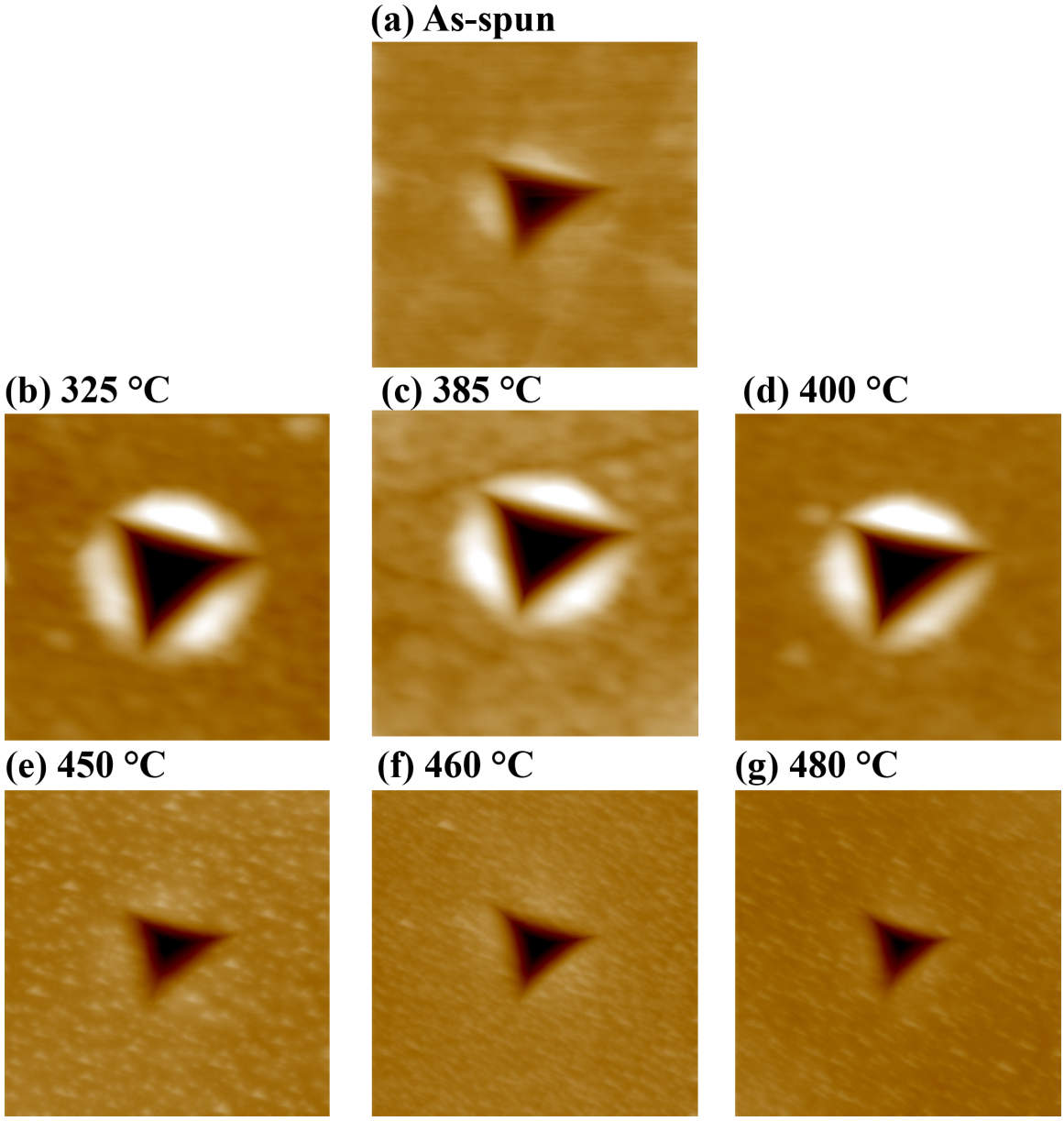

Figure 4.29: Top view scanning probe microscopy images of residual impressions from indentations performed with a Berkovich indenter on the $Ti_{40}Cu_{29}Pd_{14}Zr_{10}Sn_2Si_5$ specimens before and after irradiation with Cu^{2+} ions at different temperatures. All the scan areas ares are 3×3 μm^2 and the height scales are 100 nm.

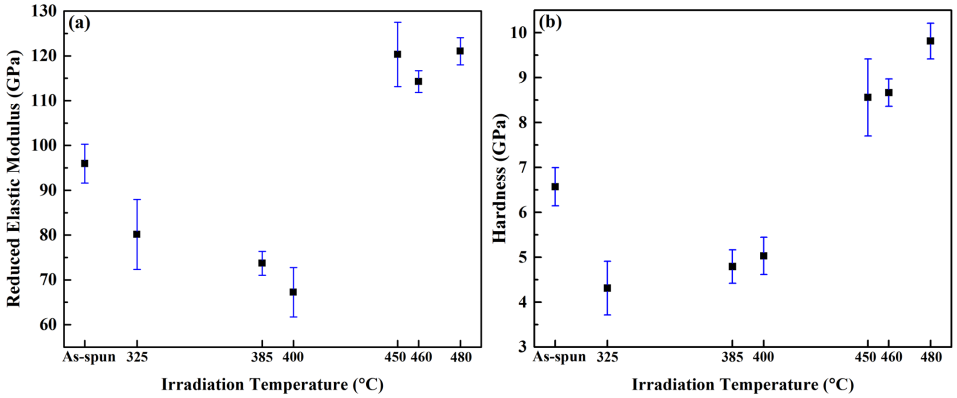

Figure 4.30: Reduced elastic modulus and hardness of the $Ti_{40}Cu_{29}Pd_{14}Zr_{10}Sn_2Si_5$ specimens before and after irradiation with Cu^{2+} ions at different temperatures.

imens, where each data point is the average of at least 10 indentations and the error bars represent plus or minus one standard deviation. As seen in Fig. 4.28, the maximum penetration depth for the indentations was $\leq$190 nm, which ensures minimum influence from the material beyond the implanted ion range of 1.7 μm on the reduced elastic modulus and hardness results [133]. For the as-spun specimen, a reduced elastic modulus of 96 GPa and a hardness of 6.6 GPa were obtained. Irradiation at 325, 385, or 400 °C resulted in a reduction in reduced elastic modulus and hardness compared to the as-spun specimen. This is consistent with the observations from Fig. 4.28 where the force vs. penetration depth curves of the specimens irradiated at 325, 385, or 400 °C shifted to larger indentation depths compared to the as-spun specimen. By increasing the irradiation temperature to the glass transition temperature of 450 °C, reduced elastic modulus and hardness increased to 120 and 8.6 GPa, respectively. Increasing the irradiation temperature to 480 °C , which resulted in complete crystallization, did not have a significant influence on the reduced elastic modulus, but increased the hardness to 9.8 GPa. The reduced elastic modulus and hardness of the fully crystallized specimen are respectively $\sim$26% and $\sim$50% higher than those of the as-spun specimen. This is consistent with the reports on fully crystallized MG specimens created by annealing where increased elastic modulus and hardness have been attributed to free volume annihilation and a subsequent increase in density [32, 138, 140].

To study the onset of plastic deformation, another set of nanoindentation experiments were performed on the specimens where a spherical indenter was used for the indentations. The loading sequence used for these indentations consisted of loading to a maximum force of 4 mN at a loading rate of 0.03 mN/s, a 60 s hold at the maximum force to allow any time dependent plastic effects to diminish, 10 s unloading to 10% of the maximum force, a 60 s hold at 10% of the maximum force

Table 4.4: Force at initial displacement burst (F_d), displacement of the indenter during the initial displacement burst (Δh), and the PDE values obtained for the $Ti_{40}Cu_{29}Pd_{14}Zr_{10}Sn_2Si_5$ specimens before and after irradiation with Cu^{2+} ions at different temperatures.

Specimen	F_d (μN)	Δh (nm)	PDE (10^{10} J/m^3)
As-spun	1752 ± 9%	1.3 - 3.6	1.15 ± 5%
Irradiated at 325 °C	1363 ± 14%	0.6 - 1.3	0.75 ± 4%
Irradiated at 385 °C	1791 ± 9%	1.1 - 3.8	0.90 ± 11%
Irradiated at 400 °C	1838 ± 10%	1.1 - 2.7	0.87 ± 5%
Irradiated at 450 °C	1990 ± 6%	1.5 - 5.6	1.20 ± 3%
Irradiated at 460 °C	1084 ± 5%	0.5 - 1.7	0.97 ± 7%

to measure thermal drift, and a 2 s final unloading. Figure 4.31 shows the force vs. penetration depth curves obtained for the as-spun and irradiated specimens where the initial displacement burst is marked with an arrow. Consistent with the observations from Fig. 4.28, displacement bursts are observed for all specimens except the one irradiated at 480 °C. The values obtained for the force and displacement at the initial displacement burst, and the PDE values for the as-spun specimen and those irradiated at 325, 385, 400, 450, and 460 °C are shown in Table 4.4. For 10 indentations, the average force values along with plus or minus one standard deviation and the minimum and maximum displacements corresponding to the initial displacement burst are reported. An average PDE value of 1.15×10^{10} J/m^3 was obtained for the as-spun specimen. The PDE value was seen to decrease after irradiation at 325, 385, and 400 °C, which suggests an increase in ductility [118]. After increasing the irradiation temperature to 450 °C, the PDE value increased and became comparable to that of the as-spun specimen suggesting a comparable ductility for these two specimens. A plausible explanation for the initial decrease in the PDE values followed by a subsequent increase at higher irradiation temperature is the competing effects of ion irradiation and annealing on free volume: while ion irradiation introduces excess free volume [63], annealing leads to the annihilation of free volume [143]. The PDE value of the specimen irradiated at 460 °C was found to be an exception to this trend since it was considerably lower than that of the as-spun specimen. However, it is likely that the nanoindentation results of this specimen have been affected by the crystalline layer that is present in the near-surface region (see Fig. 4.23(c)).

To evaluate the fracture toughness of the specimens, another set of nanoindentation experiments was performed using a cube corner indenter. For a cube corner indenter, the angle between the axis of symmetry and a face is smaller than that of a Berkovich indenter (35.3° compared to 65.3°). Therefore, at any given load, the cube corner indenter displaces more material than the Berkovich indenter, and generates greater stresses and strains in the surrounding material. Considering that the initiation and propagation of indentation cracks are promoted by larger stresses and strains, using a cuber corner indenter could result in radial cracking [168], which allows for the calculation of fracture toughness based on the maximum indentation force and crack length [168–171]. Cube corner indentations were performed at the the maximum force allowable by the instrument (10 mN). However, no sings of cracks were observed in the post-indentation SPM images of the cuber corner impressions. The absence of cracks could be an indication that the cracking threshold is higher than 10 mN. In this case, fracture toughness of the specimens cannot be evaluated by the Hysitron nanoindenter used in the present study. Another possibility is that although cracks were formed during indentation, they were closed after unloading [172]. This can be verified by performing acoustic emission (AE) nanoindentation experiments via studying the elastic waves emitted during possible crack formation.

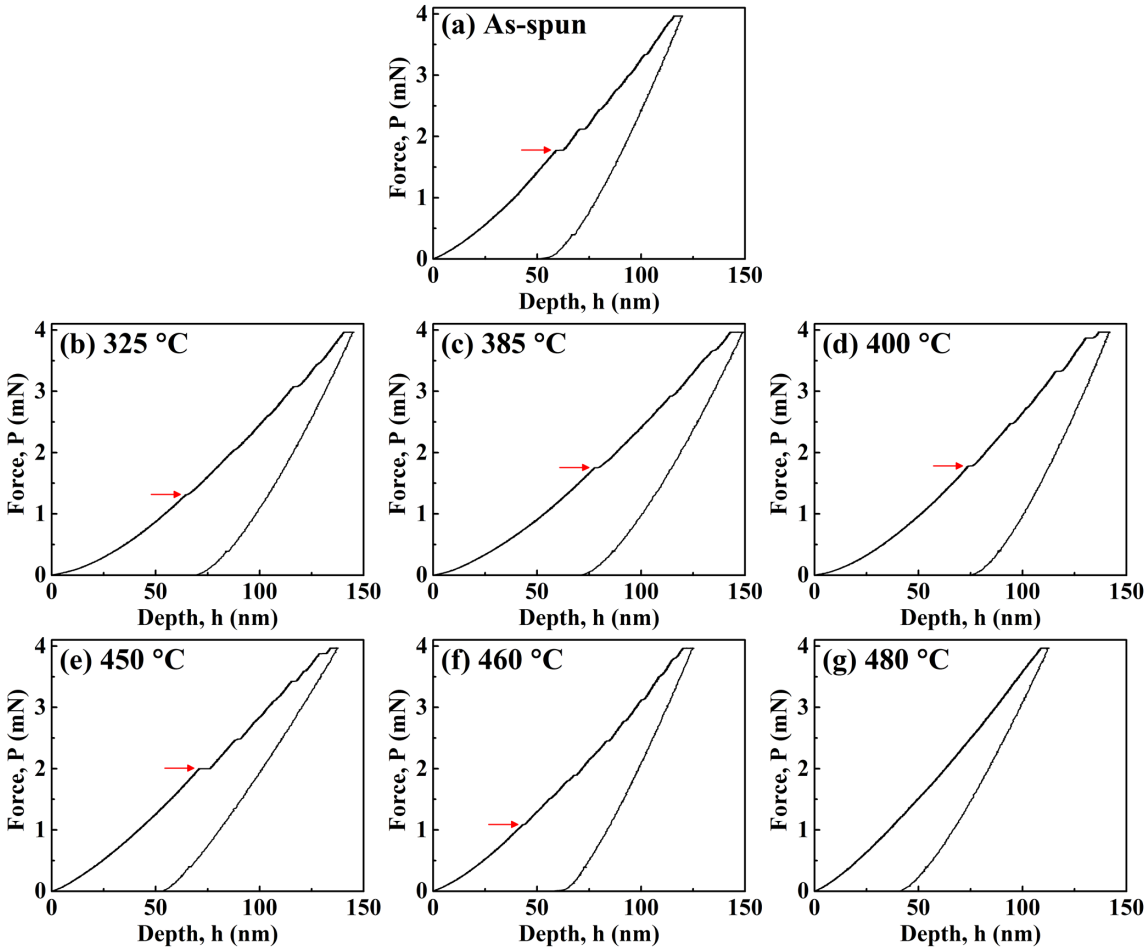

Figure 4.31: Force vs. penetration depth curves obtained from indentations with a spherical indenter on the $Ti_{40}Cu_{29}Pd_{14}Zr_{10}Sn_2Si_5$ specimens before and after irradiation with Cu^{2+} ions at different temperatures. Arrows mark the initial displacement burst for each curve.

CHAPTER V

CONCLUSIONS AND FUTURE WORK

5.1 Conclusions

1. $Ti_{40}Cu_{32}Pd_{14}Zr_{10}Sn_2Si_2$ specimens retained their amorphous structure after both annealing at temperatures below the glass transition temperature and irradiation with 4 MeV Fe^{2+} ions at room temperature (regardless of the fluence used). Annealing at temperatures below the glass transition temperature, which has been reported to lead to the annihilation of free volume, resulted in an increase in hardness and higher plastic deformation energy (PDE) values. Conversely, irradiation at room temperature, which has been reported to introduce free volume, was seen to result in a reduction of the reduced elastic modulus, hardness, and PDE values, and also shift the deformation towards less shear localization and more homogenous plastic flow.

2. $Ti_{40}Cu_{32}Pd_{14}Zr_{10}Sn_2Si_2$ and $Ti_{40}Cu_{29}Pd_{14}Zr_{10}Sn_2Si_5$ specimens remained amorphous after concurrent irradiation and annealing below the glass transition temperature. Annealing below the glass transition temperature was seen to reduce the effects of room temperature irradiation on the reduced elastic modulus and hardness as well as on the relative proportion of inhomogeneous to homogeneous deformation.

3. For the $Ti_{40}Cu_{29}Pd_{14}Zr_{10}Sn_2Si_5$ specimens subjected to concurrent annealing and irradiation with 3.5 MeV Cu^{2+} ions using a fluence of 1×10^{16} ions/cm^2, first signs of crystallization was observed in the specimen that was irradiated at the glass transition temperature. This

specimen was crystallized beyond the range of the implanted ions, but remained amorphous within the ion range. At 30 °C above the glass transition temperature, complete crystallization, within and beyond the ion range, was observed. XRD measurements demonstrated that the resulted crystalline phases are a combination of intermetallic compounds ($TiPd_3$, Zr_3Pd_4, and Pd_3Zr) and face centered cubic Cu. In contrast, $Ti_{40}Cu_{31}Pd_{14}Zr_{10}Sn_2Si_3$ specimens irradiated using the same ion species, energy, and fluence were completely crystallized at 140 °C below the glass transition temperature. Crystallization of this specimen was a result of irradiation-induced ion beam heating. Undesired beam heating can be minimized by lowering the ion beam current.

4. Irradiation of a fully crystallized $Ti_{40}Cu_{31}Pd_{14}Zr_{10}Sn_2Si_3$ specimen with 3.5 MeV Cu^{2+} ions at 25 °C using a fluence of 1×10^{14} or 1×10^{15} ions/cm^2 resulted in re-amorphization in the near-surface region. The thickness of the re-amorphized region was comparable to the range of the implanted ions.

5. A $Ti_{40}Cu_{31}Pd_{14}Zr_{10}Sn_2Si_3$ MG-matrix composite consisting of 10 - 80 nm diameter nanocrystals embedded in an amorphous matrix was fabricated by 3.5 MeV Cu^{2+} ion irradiation at 300 °C using a fluence of 1×10^{16} ions/cm^2 followed by a second step irradiation at 25 °C using the same ion species, energy, and fluence. Formation of nanocrystals in the composite was seen to result in an increase in reduced elastic modulus and hardness, and to shift the deformation mechanism towards less shear localization and more homogenous plastic flow compared to the as-spun specimen. These observations are consistent with the reports that formation of nanocrystals can promote initiation of a large number of shear bands and inhibit shear band propagation.

6. Irradiation of $Ti_{40}Cu_{34-x}Pd_{14}Zr_{10}Sn_2Si_x$ (x = 2, 3, and 5) specimens with 4 MeV Fe^{2+} or 3.5 MeV Cu^{2+} ions appeared to favor amorphization and even delayed the onset of crystallization when irradiation was performed at the glass transition temperature.

5.2 Potential Future Studies

- It remains unclear whether a partially crystallized MG specimen can be obtained by ion irradiation at elevated temperature followed by ion irradiation at 25 °C when ion beam heating is prevented. The fully crystallized $Ti_{40}Cu_{29}Pd_{14}Zr_{10}Sn_2Si_5$ specimen obtained by ion irradiation at 480 °C should be irradiated again at room temperature over a range of fluences to

address this question.

- Although irradiation-induced crystallization has been reported in MGs at room temperature, no signs of crystallization was observed in the $Ti_{40}Cu_{34-x}Pd_{14}Zr_{10}Sn_2Si_x$ (x = 2, 3, and 5) specimens that were irradiated in this study. Investigating the effects of ion species and energies on structural evolutions caused by irradiation can help identify whether direct irradiation-induced crystallization is achievable in this alloy.

- Direct characterization of free volume, using techniques such as positron annihilation spectroscopy (PAS), can be useful in understanding the correlations between the irradiation-induced changes in free volume and mechanical behavior of the specimens.

- Performing uniaxial compression experiments on micropillars, produced by focused ion beam (FIB) milling, followed by studying the deformation in the micropillars using a scanning electron microscope (SEM) can provide additional information about the deformation behavior and shear band activity in the as-spun and irradiated MG specimens.

- Nanolaminate composites consisting of alternating layers of amorphous and crystallized MG have been fabricated by depositing parallel layers of Pt on the surface of a fully crystallized $Ti_{40}Cu_{29}Pd_{14}Zr_{10}$ Sn_2Si_5 specimen followed by ion irradiation at 25 °C. Studying the mechanical response of these nanolaminates helps identify the effects of amorphous/crystalline interfaces on the deformation behavior of MGs.

REFERENCES

[1] L. Huang, Z. Cao, H.M. Meyer, P.K. Liaw, E. Garlea, J.R. Dunlap, T. Zhang, and W. Heb. Responses of bone-forming cells on pre-immersed Zr-based bulk metallic glasses: Effects of composition and roughness. *Acta Biomaterialia*, 7:395–405, 2011.

[2] B.G. Yoo, J.Y. Kim, Y.J. Kim, I.C. Choi, S. Shim, T.Y. Tsui, H. Bei, U. Ramamurty., and J.I. Jang. Increased time-dependent room temperature plasticity in metallic glass nanopillars and its size-dependency. *International Journal of Plasticity*, 37:108–118, 2012.

[3] S. Kumar, J. Kim, H. Kim, and C. Lee. Phase dependence of Fe-based bulk metallic glasses on properties of thermal spray coatings. *Journal of Alloys and Compounds*, 475:L9–L12, 2009.

[4] Z.Y. Zhang, Y. Wu, J. Zhou, H. Wang, X.J. Liu, and Z.P. Lu. Strong work-hardening behavior in a Ti − based bulk metallic glass composite. *Scripta Materialia*, 69:73–76, 2013.

[5] J.W. Qiao, J.T. Zhang, F. Jiang, Y. Zhang, P.K. Liaw, Y. Ren, and G.L. Chen. Development of plastic Ti − based bulk-metallic-glass-matrix composites by controlling the microstructures. *Materials Science and Engineering A*, 527:7752–7756, 2010.

[6] H.-J. Jun, K.S. Lee, C.P. Kim, and Y.W. Chang. Ductility enhancement of a Ti − based bulk metallic glass through annealing treatment below the glass transition temperature. *Intermetallics*, 20:47–54, 2012.

[7] M. Jafary-Zadeh, G. Praveen Kumar, P.S. Branicio, M. Seifi, J.J. Lewandowski, and F. Cui. A critical review on metallic glasses as structural materials for cardiovascular stent applications. *Journal of Functional Biomaterials*, 9:19, 2018.

[8] P. Gong, L. Deng, J. Jin, S. Wang, X. Wang, and K. Yao. Review on the research and development of Ti − Based bulk metallic glasses. *Metals*, 6:264, 2016.

[9] H.F. Li and Y.F. Zheng. Recent advances in bulk metallic glasses for biomedical applications. *Acta Biomaterialia*, 36:1–20, 2016.

[10] S. Yang, D. Li, X.S. Wang, J.W. Guo, S.F. Zhang, and L. He. Mechanical behavior and wear performance of a Ti − based bulk metallic glass composite containing dendritic and intermetallic phases. *Materials Science and Engineering A*, 672:135–142, 2016.

[11] J. Fornell, N. Van Steenberge, A. Varea, E. Rossinyol, E. Pellicer, S. Suriach, M.D. Bar, and J. Sort. Enhanced mechanical properties and in vitro corrosion behavior of amorphous and devitrified $Ti_{40}Zr_{10}Cu_{38}Pd_{12}$ metallic glass. *Journal of the Mechanical Behavior of Biomedical Materials*, 4:1709–1717, 2011.

[12] F.X. Qin, X.M. Wang, G.Q. Xie, and A. Inoue. Distinct plastic strain of Ni − free TiZrCuPdNb bulk metallic glasses with potential for biomedical applications. *Intermetallics*, 16:1026–1030, 2008.

[13] M.K. Miller and P. Liaw. *Bulk metallic glasses: An overview*. Springer Science and Business Media, 2008.

[14] D.C. Hofmann, J.Y. Suh, A. Wiest, G. Duan, M.L. Lind, M.D. Demetriou, and W.L. Johnson. Designing metallic glass matrix composites with high toughness and tensile ductility. *Nature*, 451:1085–1089, 2008.

[15] F.X. Liu, Y.F. Gao, and P.K. Liaw. Rate-dependent deformation behavior of Zr-based metallic-glass coatings examined by nanoindentation. *Metallurgical and Materials Transaction A*, 39A:1862–1867, 2008.

[16] L. Liu and K.C. Chan. Plastic deformation of Zr-based bulk metallic glasses under nanoindentation. *Materials Letters*, 59:3090–3094, 2008.

[17] C.A. Schuh, T.C. Hufnagel, and U. Ramamurty. Mechanical behavior of amorphous alloys. *Acta Materialia*, 55:4067–4109, 2007.

[18] Y.L. Tang, T.W. Zhang, X.H. Shi, J.W. Qiao , Z.H. Wang, H.F. Zhou, and Y.C. Wu. Design novel Ti − based metallic glass matrix composites with excellent dynamic plasticity. *Journal of Alloys and Compounds*, 773:844–852, 2019.

[19] J.L. Dong, Z. Wang, L.N. Han, Y.L. Tang, J.W. Qiao, X.H. Shi, Z.H. Wang, and Y.C. Wu. Novel $in-situ$ Ti − based dendrite/nanostructured matrix composites with excellent mechanical performances upon dynamic compression. *Journal of Alloys and Compounds*, 781:716–722, 2019.

[20] Y.S. Wang, F. Tian, B.B. Qiao, S.M. Ma, X.T. Wang, X.M. Wang, and A.D. Lan. Mechanical property and serration behavior of $Ti-$based metallic glassy composites reinforced by an $in-situ$ dendritic phase. *Materials Science and Engineering A*, 743:301–308, 2019.

[21] L. Zhang, R.L. Narayan, H.M. Fu, U. Ramamurty, W.R. Li, Y.D. Li, and H.F. Zhang. Tuning the microstructure and metastability of $\beta-$Ti for simultaneous enhancement of strength and ductility of $Ti-$based bulk metallic glass composites. *Acta Materialia*, 168:24–36, 2019.

[22] Y.Y. Liu, J.J. Li, Z. Wang, X.H. Shi, J.W. Qiao, and Y.C. Wu. Prediction of tensile yielding in metallic glass matrix composites. *Intermetallics*, 108:72–76, 2019.

[23] L. Li, J. Li, Y. He, W.Y. Wang, H. Kou, and J. Wang. Tensile properties and deformation micromechanism of $Ti-$based metallic glass composite containing impurity elements. *Journal of Alloys and Compounds*, 784:220–230, 2019.

[24] Q. Li, S.S. Liu, X.H. Wang, T. Yang, C. Dong, J.T. Hu, and Y.Q. Jiang. Mechanical and corrosion properties of $Ti-Ni-Cu-Zr$ metallic glass matrix composites. *Journal of Alloys and Compounds*, 727:1344–1350, 2017.

[25] J. Fan, J.W. Qiao, Z.H. Wang, W. Rao, and G.Z. Kang. Twinning-induced plasticity (TWIP) and work hardening in $Ti-$based metallic glass matrix composites. *Scientific Reports*, 7:1877, 2017.

[26] R.F. Wu, Z.M. Jiao, Y.S. Wang, Z. Wang, Z.H. Wang, S.G. Ma, and J.W. Qiao. Excellent plasticity of a new $Ti-$based metallic glass matrix composite upon dynamic loading. *Materials Science and Engineering A*, 677:376–38, 2016.

[27] J. Bai, J.S. Li, J. Wang, J. Cui, L.Y. Li, H.C. Kou, and P.K. Liaw. Strain-rate-dependent deformation behavior in a $Ti-$based bulk metallic glass composite upon dynamic deformation. *Journal of Alloys and Compounds*, 639:131–138, 2015.

[28] M.Y. Chu, Z.M. Jiao, R.F. Wu, Z.H. Wang, H.J. Yang, Y.S. Wang, and J.W. Qiao. Quasi-static and dynamic deformation behaviors of an $in-situ$ $Ti-$based metallic glass matrix composite. *Journal of Alloys and Compounds*, 640:305–310, 2015.

[29] D.Q. Ma, W.T. Jiao, Y.F. Zhang, B.A. Wang, J. Li, X.Y. Zhang, M.Z. Ma, and R.P. Liu. Strong work-hardening behavior induced by the solid solution strengthening of dendrites in $TiZr-$based bulk metallic glass matrix composites. *Journal of Alloys and Compounds*, 624:9–16, 2015.

[30] J. Cui, J.S. Li, J. Wang, and H.C. Kou. Microstructure evolution of a Ti − Based bulk metallic glass composite during deformation. *Journal of Materials Engineering and Performance*, 24:748–753, 2015.

[31] G. He, J. Eckert, W. Lser, and L. Schultz. Novel Ti − base nanostructure-dendrite composite with enhanced plasticity. *Nature Materials*, 2:33, 2003.

[32] B.B. Medeiros, M.M. Medeiros, J. Fornell, J. Sort, M.D. Barc, and A.M. Jorge Junior. Nanoindentation response of Cu − Ti based metallic glasses: Comparison between as-cast, relaxed and devitrified states. *Journal of Non-Crystalline Solids*, 425:103–109, 2015.

[33] R. Raghavan, V.V. Shastry, A. Kumar, T. Jayakumar, and U. Ramamurty. Toughness of as-cast and partially crystallized composites of a bulk metallic glass. *Intermetallics*, 17:835–839, 2009.

[34] L. Zhang, S. Pauly, Z.W. Zhu, T. Gemming, H.M. Fu, J. Eckert, and H.F. Zhang. Ion milling-induced micrometer-sized heterogeneities and partial crystallization in a TiZrCuFeBe bulk metallic glass. *Intermetallics*, 73:5–11, 2016.

[35] E. Menendez, A. Hynowska, J. Fornell, S. Suriach, J. Montserrat, K. Temst, A. Vantomme, M.D. Bar, E. Garca-Lecina, E. Pellicer, and J. Sort. Influence of the irradiation temperature on the surface structure and physical/chemical properties of Ar ion-irradiated bulk metallic glasses. *Journal of Alloys and Compounds*, 610:118–125, 2014.

[36] A. Brenner, D.E. Couch, and E.K. Williams. Electrodeposition of alloys of phosphorus with nickel or cobalt. *Journal of Research of the National Bureau of Standards*, 44:109, 1950.

[37] W. Buckel. Elektronenbeugungs-aufnahmen von dnnen metallschichten bei tiefen temperaturen. *Zeitschrift fur Physik*, 138:136–150, 1954.

[38] W. Klement Jun., R.H. Willens, and P. Duwez. Non-crystalline structure in solidified gold-silicon alloys. *Nature*, 187:869–870, 1960.

[39] J. Basu and S. Ranganathan. Bulk metallic glasses: A new class of engineering materials. *Sadhana*, 28:783–798, 2003.

[40] H.S. Chen and D. Turnbull. Formation, stability and structure of palladium-silicon based alloy glasses. *Acta Metallurgica*, 17:1021–1031, 1969.

[41] H.S. Chen. Thermodynamic considerations on the formation and stability of metallic glasses. *Acta Metallurgica*, 22:1505–1511, 1974.

[42] A.J. Drehman, A.L. Greer, and D. Turnbull. Bulk formation of a metallic glass: $Pd_{40}Ni_{40}P_{20}$. *Applied Physics Letters*, 41:716, 1982.

[43] H.W. Kui, A.L. Greer, and D. Turnbull. Formation of bulk metallic glass by fluxing. *Applied Physics Letters*, 45:615, 1984.

[44] A. Peker and W.L. Johnson. A highly processable metallic glass: $Zr_{41.2}Ti_{13.8}Cu_{12.5}Ni_{10.0}Be_{22.5}$. *Applied Physics Letters*, 63:2342, 1993.

[45] A. Inoue, N. Nishiyama, and H. Kimura. Preparation and thermal stability of bulk amorphous $Pd_{40}Cu_{30}Ni_{10}P_{20}$ alloy cylinder of 72 mm in diameter. *Materials Transactions*, 38:179–183, 1997.

[46] N. Nishiyama, K. Takenaka, H. Miura, N. Saidoh, Y. Zeng, and A. Inoue. The world's biggest glassy alloy ever made. *Intermetallics*, 30:19–24, 2012.

[47] H. Xu, Y. Lu, Z. Liu, and G. Wang. Laser 3D printing of $Zr-$based bulk metallic glass. *Journal of Manufacturing Processes*, 39:102–105, 2019.

[48] N. Li, J. Zhang, W. Xing, D. Ouyang, and L. Liu. 3D printing of $Fe-$based bulk metallic glass composites with combined high strength and fracture toughness. *Materials and Design*, 143:285–296, 2018.

[49] Y. Shen, Y. Li, C. Chen, and H.-L. Tsai. 3D printing of large, complex metallic glass structures. *Materials and Design*, 117:213–222, 2017.

[50] A. Inoue, I. Yoshii, H. Kimura, K. Okumura, and J. Kurosaki. Enhanced shot peening effect for steels by using $Fe-$based glassy alloy shots. *Materials Transactions*, 44:2391–2395, 2003.

[51] M.F. Ashby and A.L. Greer. Metallic glasses as structural materials. *Scripta Materialia*, 54:321–326, 2006.

[52] N. Nishiyama, K. Amiya, and A. Inoue. Recent progress of bulk metallic glasses for strain-sensing devices. *Materials Science and Engineering*, 449-451:79–83, 2007.

[53] M. Ishida, H. Takeda, D. Watanabe, K. Amiya, N. Nishiyama, K. Kita, Y. Saotome, and A. Inoue. Fillability and imprintability of high-strength $Ni-$based bulk metallic glass prepared by the precision die-casting technique. *Materials Transactions*, 45:1239–1244, 2004.

[54] D.C. Hofmann, R. Polit-Casillas, S.N. Roberts, J.P. Borgonia, R.P. Dillon, E. Hilgemann, J. Kolodziejska, L. Montemayor, J.O. Suh, A. Hoff, K. Carpenter, A. Parness, W.L. Johnson, A. Kennett, and B. Wilcox. Castable bulk metallic glass strain wave gears: Towards decreasing the cost of high-performance robotics. *Scientific Reports*, 6:37773, 2016.

[55] D.C. Hofmann, L.M. Andersen, J. Kolodziejska, S.N. Roberts, J.P. Borgonia, W.L. Johnson, K.S. Vecchio, and A. Kennett. Optimizing bulk metallic glasses for robust, highly wearresistant gears. *Advanced Engineering Materials*, 19:1600541, 2017.

[56] D.C. Hofmann, G.L. Davis, G.S. Agnes, and A.A. Shapiro. *US Patent #9,507,061 B2: Amorphous metals and composites as mirrors and mirror assemblies.* 2016.

[57] J.F. Loffler. Bulk metallic glasses. *Intermetallics*, 11:529–540, 2003.

[58] S. Michalik, J. Michalikova, M. Pavlovic, P. Sovak, H.-P. Liermann, and M. Miglierini. Structural modifications of swift-ion-bombarded metallic glasses studied by high-energy $X-$ray synchrotron radiation. *Acta Materialia*, 80:309–316, 2014.

[59] D. Turnbull and M.H. Cohen. Free-volume model of the amorphous phase: Glass transition. *The Journal of Chemical Physics*, 34:120, 1961.

[60] M.H. Cohen and D. Turnbull. Molecular transport in liquids and glasses. *The Journal of Chemical Physics*, 31:1164, 1959.

[61] D. Turnbull and M.H. Cohen. On the free-volume model of the liquid-glass transition. *The Journal of Chemical Physics*, 52:3038, 1970.

[62] M.M. Trexler and N.N. Thadhani. Mechanical properties of bulk metallic glasses. *Progress in Materials Science*, 55:759–839, 2010.

[63] R. Raghavan, B. Kombaiah, M. Dobeli, R. Erni, U. Ramamurty, and J. Michler. Nanoindentation response of an ion irradiated $Zr-$based bulk metallic glass. *Materials Science and Engineering A*, 532:407–413, 2012.

[64] L. Zhiyuan. *Micromechanical behavior investigation of metallic glasses.* Ph.D. Dissertation, The Hong Kong Polytechnic University, 2012.

[65] J.D. Bernal and J. Mason. Packing of spheres: Co-ordination of randomly packed spheres. *Nature*, 188:910–911, 1960.

[66] F. Spaepen and D. Turnbull. Metallic glasses. *Annual Review of Physical Chemistry*, 35:241–263, 1984.

[67] P.H. Gaskell. A new structural model for transition metal-metalloid glasses. *Nature*, 276:484–485, 1978.

[68] P.H. Gaskell. A new structural model for amorphous transition metal silicides, borides, phosphides and carbides. *Journal of Non-Crystalline Solids*, 32:207–224, 1979.

[69] D.B. Miracle. A structural model for metallic glasses. *Nature Materials*, 3:697–702, 2004.

[70] H. Jia, G. Wang, S. Chen, Y. Gao, W. Li, and P.K. Liaw. Fatigue and fracture behavior of bulk metallic glasses and their composites. *Progress in Materials Science*, 98:168–248, 2018.

[71] A.S. Argon and H.Y. Kuo. Plastic flow in a disordered bubble raft (an analog of a metallic glass). *Materials Science and Engineering*, 39:101–109, 1979.

[72] F. Spaepen. A microscopic mechanism for steady state inhomogeneous flow in metallic glasses. *Acta Metallurgica*, 25:407–415, 1977.

[73] A.S. Argon. Plastic deformation in metallic glasses. *Acta Metallurgica*, 27:47–58, 1979.

[74] B. Yang, C.T. Liu, and T.G. Nieh. Unified equation for the strength of bulk metallic glasses. *Applied Physics Letters*, 88:221911, 2006.

[75] T.H. Courtney. *Mechanical behavior of materials*. McGraw-Hill, 1990.

[76] T. Mukai, T.G. Nieh, Y. Kawamura, A. Inoue, and K. Higashi. Effect of strain rate on compressive behavior of a $Pd_{40}Ni_{40}P_{20}$ bulk metallic glass. *Intermetallics*, 10:1071–1077, 2002.

[77] Z.F. Zhang, J. Eckert, and L. Schultz. Difference in compressive and tensile fracture mechanisms of $Zr_{59}Cu_{20}Al_{10}Ni_8Ti_3$ bulk metallic glass. *Acta Materialia*, 51:1167–1179, 2003.

[78] P.E. Donovan. A yield criterion for $Pd_{40}Ni_{40}P_{20}$ metallic glass. *Acta Metallurgica*, 37:445–456, 1989.

[79] C.A. Schuh and A.C. Lund. Atomistic basis for the plastic yield criterion of metallic glass. *Nature Materials*, 2:449, 2003.

[80] B. Yang and C.T. Liu. Localized heating and fracture criterion for bulk metallic glasses. *Journal of Materials Research*, 21:915–922, 2006.

[81] F. Szuecs, C.P. Kim, and W.L. Johnson. Mechanical properties of $Zr_{56.2}Ti_{13.8}Nb_{5.0}$ $Cu_{6.9}Ni_{5.6}Be_{12.5}$ ductile phase reinforced bulk metallic glass composite. *Acta Materialia*, 49:1507–1513, 2001.

[82] C. Fan, C. Li, and A. Inoue. Deformation behavior of Zr-based bulk nanocrystalline amorphous alloys. *Physical Review B*, 61:R3761–R3763, 2000.

[83] M.L. Lee, Y. Li, and C.A. Schuh. Effect of a controlled volume fraction of dendritic phases on tensile and compressive ductility in La-based metallic glass matrix composites. *Acta Materialia*, 52:4121–4131, 2004.

[84] G. Xie, L. Shao, D.V. Louzguine-Luzgin, and A. Inoue. He ion irradiation induced nanocrystallization in $Cu_{50}Zr_{45}Ti_5$ glassy alloy. *Surface and Coatings Technology*, 206:829–833, 2011.

[85] W.D. Luo, B. Yanga, and G.L. Chen. Effect of Ar^+ ion irradiation on the microstructure and properties of $Zr - Cu - Fe - Al$ bulk metallic glass. *Scripta Materialia*, 64:625–628, 2011.

[86] M. Myers, E.G. Fu, M. Myers, H. Wang, G. Xie, X. Wang, W.K. Chu, and L. Shao. An experimental and modeling study on the role of damage cascade formation in nanocrystalization of ion-irradiated $Ni_{52.5}Nb_{10}Zr_{15}Ti_{15}Pt_{7.5}$ metallic glass. *Scripta Materialia*, 63:1045–1048, 2010.

[87] J. Carter, E.G. Fu, M. Martin, G. Xie, X. Zhang, Y.Q. Wang, D. Wijesundera, X.M. Wang, W.K. Chu, S.M. McDeavitt, and L. Shao. Ion irradiation induced nanocrystal formation in amorphous $Zr_{55}Cu_{30}Al_{10}Ni_5$ alloy. *Nuclear Instruments and Methods in Physics Research Section B: Beam Interactions with Materials and Atoms*, 267:2827–2831, 2009.

[88] X. Zhang, X. Mei, Q. Zhang, X. Li, Y. Wang, and Y. Wang. Study of irradiation damage induced by He^{2+} ion irradiation in $Ni_{62}Ta_{38}$ metallic glass and W metal. *Nuclear Instruments and Methods in Physics Research Section B: Beam Interactions with Materials and Atoms*, 406:548–554, 2017.

[89] X. Zhang, X. Mei, Q. Zhang, X. Li, J. Qiang, and Y. Wang. Damage induced by helium ion irradiation in $Fe -$ based metallic glass. *Journal of Nuclear Materials*, 490:216–225, 2017.

[90] M. Nastasi, J.W. Mayer, and J.K. Hirvonen. *Ion-solid interactions: Fundamentals and applications*. Cambridge University Press, 1996.

[91] C.A. Volkert and A.M. Minor. Focused ion beam microscopy and micromachining. *MRS Bulletin*, 32:389–399, 2007.

[92] M.T. Myers, S. Charnvanichborikarn, C.C. Wei, Z.P. Luo, G.Q. Xie, S.O. Kucheyev, D.A. Lucca, and L. Shao. Phase transition, segregation and nanopore formation in high-energy heavy-ion-irradiated metallic glass. *Scripta Materialia*, 67:887–890, 2012.

[93] Z. Liu. *Micromechanical behavior investigation of metallic glasses*. Ph.D. Dissertation, The Hong Kong Polytechnic University, 2012.

[94] G. Kumar, D. Rector, R.D. Conner, and J. Schroers. Embrittlement of $Zr-$ based bulk metallic glasses. *Acta Materialia*, 57:3572–3583, 2009.

[95] T.W. Wu and F. Spaepen. The relation between enbrittlement and structural relaxation of an amorphous metal. *Philosophical Magazine B*, 61:739–750, 1990.

[96] W. Dmowski, C. Fan, M.L. Morrison, P.K. Liaw, and T. Egami. Structural changes in bulk metallic glass after annealing below the glass-transition temperature. *Materials Science and Engineering A*, 471:125–129, 2007.

[97] S. Zhu, G. Xie, F. Qin, and X. Wang. Effects of minor Si addition on glass formation and thermal stability of Ni free $Ti-$ based bulk metallic glass. *Materials Science Forum*, 750:36–39, 2013.

[98] J.F. Ziegler and J.P. Biersack. *The stopping and range of ions in solids*. Pergamon Press, 1985.

[99] L.M. Price. *A study of the crystallization and amorphization mechanics of metallic glasses under ion bombardment*. Ph.D. Dissertation, Texas A and M University, 2016.

[100] T. Nagase, T. Hosokawa, and Y. Umakoshi. Solid state amorphization and crystallization in $Zr_{66.7}Pd_{33.3}$ metallic glass. *Intermetallics*, 14:1027–1032, 2006.

[101] A. Nino, T. Nagase, and Y. Umakoshi. Electron irradiation induced crystallization and amorphization in $Fe_{77}Nd_{4.5}B_{18.5}$ metallic glass. *Materials Science and Engineering A*, 449:1115–1118, 2007.

[102] S. Mechler, C. Abromeit, N. Wanderka, M.P. Macht, T. Zumkley, G. Schumacher, and S. Klaumnzer. Phase transformation quasicrystalline $-$ amorphous in $Zr-Ti-Ni-Cu$ by swift heavy ions. *Nuclear Instruments and Methods in Physics Research Section B: Beam Interactions with Materials and Atoms*, 245:133–136, 2006.

[103] P. Moine and C. Jaouen. Ion beam induced amorphization in the intermetallic compounds NiTi and NiAl. *Journal of Alloys and Compounds*, 194:373–380, 1993.

[104] H. Mori and H. Fujita. Temperature dependence of electron-irradiation induced amorphization of NiTi alloys. *Japanese Journal of Applied Physics*, 21:L494–L496, 1982.

[105] H. Kojima, Y. Kaneno, M. Ochi, S. Semboshi, F. Hori, Y. Saitoh, N. Ishikawa, Y. Okamoto, and A. Iwase. Ion species/energy dependence of irradiation-induced lattice structure transformation and surface hardness of Ni_3Nb and Ni_3Ta intermetallic compounds. *Materials Transactions*, 58:739–748, 2017.

[106] T. Nagase, Y. Umakoshi, and N. Sumida. Effect of electron irradiation on the phase stability of $Fe-9Zr-3B$ alloy. *Materials Science and Engineering A*, 323:218–225, 2002.

[107] T. Nagase, Y. Umakoshi, and N. Sumida. Formation of nanocrystalline structure during electron irradiation induced crystallization in amorphous $Fe-Zr-B$ alloys. *Science and Technology of Advanced Materials*, 3:119–128, 2002.

[108] K. OConnell and J.R. Regalbuto. High sensitivity silicon slit detectors for 1 nm powder XRD size detection limit. *Catalysis Letters*, 145:777–783, 2015.

[109] J.A. Newman, P.D. Schmitt, S.J. Toth, F. Deng, S. Zhang, and G.J. Simpson. Parts per million powder $X-$ ray diffraction. *Analytical Chemistry*, 87:10950–10955, 2015.

[110] S. Kalpakjian and S.R. Schmid. *Manufacturing processes for engineering materials.* Pearson Education, Inc., 2008.

[111] G.E. Dieter. *Mechanical metallurgy.* McGraw-Hill, 1986.

[112] C.A. Schuh and T.G. Nieh. A survey of instrumented indentation studies on metallic glasses. *Journal of Materials Research*, 19:46–57, 2004.

[113] W.C. Oliver and G.M. Pharr. An improved technique for determining hardness and elastic modulus using load and displacement sensing indentation experiments. *Journal of Materials Research*, 7:1564–1583, 1992.

[114] J. Hay. Introduction to instrumented indentation testing. *Experimental Techniques*, 33:66–72, 2009.

[115] L. Wang, Z.P. Lu, and T.G. Nieh. Onset of yielding and shear band nucleation in an $Au-$ based bulk metallic glass. *Scripta Materialia*, 65:759–762, 2011.

[116] H. Bei, Z.P. Lu, and E.P. George. Theoretical strength and the onset of plasticity in bulk metallic glasses investigated by nanoindentation with a spherical indenter. *Physical Review Letters*, 93:125504, 2004.

[117] Y. Huang, Y.L. Chiu, J. Shen, J.J.J. Chen, and J. Sun. Nanoindentation study of Ti − based metallic glasses. *Journal of Alloys and Compounds*, 479:121–128, 2009.

[118] K. Wang, M.W. Chen, D. Pan, T. Fujita, W. Zhang, X.M. Wang, and A. Inoue. Plastic deformation energy of bulk metallic glasses. *Materials Science and Engineering B*, 148:101–104, 2008.

[119] C.A. Schuh, A.S. Argon, T.G. Nieh, and J. Wadsworth. The transition from localized to homogeneous plasticity during nanoindentation of an amorphous metal. *Philosophical Magazine*, 83:2585–2597, 2003.

[120] V. Venkatesh and K. Mondal. Effect of cast temperature, size and annealing condition on the serrated flow during nano-indentation of Zr − based bulk metallic glasses. *Journal of Alloys and Compounds*, 692:745–757, 2017.

[121] C.A. Schuh and T.G. Nieh. A nanoindentation study of serrated flow in bulk metallic glasses. *Acta Materialia*, 51:87–99, 2003.

[122] C.A. Schuh and T.G. Nieh. Rate dependence of serrated flow during nanoindentation of a bulk metallic glass. *Journal of Materials Research*, 17:1651–1654, 2002.

[123] A. Zare, M.J. Klopfstein, D.A. Lucca, L. Price, L. Shao L, and G.Q. Xie. Nanoindentation studies of the effects of ion irradiation on the near surface mechanical response of annealed $Ti_{40}Cu_{32}Pd_{14}Zr_{10}Sn_2Si_2$ metallic glass ribbons. *Journal of Tribology*, 138:041403, 2016.

[124] P. Murali and U. Ramamurty. Embrittlement of a bulk metallic glass due to sub − T_g annealing. *Acta Materialia*, 53:1467–1478, 2005.

[125] J. Gu, M. Song, S. Ni, S. Guo, and Y. He. Effects of annealing on the hardness and elastic modulus of a $Cu_{36}Zr_{48}Al_8Ag_8$ bulk metallic glass. *Materials and Design*, 47:706–710, 2013.

[126] B.G. Yoo, K.W. Park, J.C. Lee, U. Ramamurty, and J.I. Jang. Role of free volume in strain softening of as-cast and annealed bulk metallic glass. *Journal of Materials Research*, 24:1405–1416, 2009.

[127] I.C. Choi, Y. Zhao, Y.J. Kim, B.G. Yoo, J.Y. Suh, U. Ramamurty, and J.I. Jang. Indentation size effect and shear transformation zone size in a bulk metallic glass in two different structural states. *Acta Materialia*, 60:6862–6868, 2012.

[128] C. Nagel, K. Rtzke, E. Schmidtke, J. Wolff, U. Geyer, and F. Faupel. Free-volume changes in the bulk metallic glass $Zr_{46.7}Ti_{8.3}Cu_{7.5}Ni_{10}Be_{27.5}$ and the undercooled liquid. *Physical Review B*, 57:10224, 1998.

[129] C.E. Packard and C.A. Schuh. Initiation of shear bands near a stress concentration in metallic glass. *Acta Materialia*, 55:5348–5358, 2007.

[130] U. Ramamurty, S. Jana, Y. Kawamura, and K. Chattopadhyay. Hardness and plastic deformation in a bulk metallic glass. *Acta Materialia*, 53:705–717, 2005.

[131] U. Ramamurty, M.L. Lee, J. Basu, and Y. Li. Embrittlement of a bulk metallic glass due to low-temperature annealing. *Scripta Materialia*, 47:107–111, 2002.

[132] D.A. Lucca, A. Zare, M.J. Klopfstein, L. Shao, and G.Q. Xie. Investigation of the mechanical behavior of ion irradiated Ni − free Ti − based metallic glass by nanoindentation. *CIRP Annals - Manufacturing Technology*, 63:533–536, 2014.

[133] ISO 14577-1 (2002). Metallic materials − Instrumented indentation test for hardness and materials parameters − Part 1: Test method. ISO, Geneva, Switzerland, 2002.

[134] Z. Hu, Z. Zhao, Y. Hu, J. Xing, T. Lu, and B. Wei. Effect of ion irradiation on mechanical behaviors of $Ti_{40}Zr_{25}Be_{30}Cr_5$ bulk metallic glass. *Materials Research*, 15:713–717, 2012.

[135] W.H. Jiang and M. Atzmon. Rate dependence of serrated flow in a metallic glass. *Journal of Materials Research*, 18:755–757, 2003.

[136] J. Li, F. Spaepen, and T.C. Hufnagel. Nanometre-scale defects in shear bands in a metallic glass. *Philosophical Magazine*, 82:2623–2630, 2002.

[137] W.J. Wright, T.C. Hufnagel, and W.D. Nix. Free volume coalescence and void formation in shear bands in metallic glass. *Journal of Applied Physics*, 93:1432, 2003.

[138] M. Apreutesei, A. Billard, and P. Steyer. Crystallization and hardening of Zr − 40 at.% Cu thin film metallic glass: Effects of isothermal annealing. *Materials and Design*, 86:555–563, 2015.

[139] Y. Huang, Z. Ning, Z. Shen, W. Liang, H. Sun, and J. Sun. Bending behavior of as-cast and annealed ZrCuNiAl bulk metallic glass. *Journal of Materials Science and Technology*, 33:1153–1158, 2017.

[140] J. Fornell, S. Gonzlez, E. Rossinyol, S. Suriach, M.D. Bar, D.V. Louzguine-Luzgin, J.H. Perepezko, J. Sort, and A. Inoue. Enhanced mechanical properties due to structural changes induced by devitrification in $Fe-Co-B-Si-Nb$ bulk metallic glass. *Acta Materialia*, 58:6256–6266, 2010.

[141] J.G. Wang, B.W. Choi, T.G. Nieh, and C.T. Liu. Crystallization and nanoindentation behavior of a bulk $Zr-Al-Ti-Cu-Ni$ amorphous alloy. *Journal of Materials Research*, 15:798–807, 2000.

[142] L. Charleux, S. Gravier, M. Verdier, M. Fivel, and J.J. Blandin. Amorphous and partially crystallized metallic glasses: An indentation study. *Materials Science and Engineering A*, 483-484:652–655, 2008.

[143] R. Raghavan, K. Boopathy, R. Ghisleni, M.A. Pouchon, U. Ramamurty, and J. Michler. Ion irradiation enhances the mechanical performance of metallic glasses. *Scripta Materialia*, 62:462–465, 2010.

[144] M.L. Crespillo, J.T. Graham, Y. Zhang, and W.J. Weber. Temperature measurements during high flux ion beam irradiations. *Review of Scientific Instruments*, 87:024902, 2016.

[145] G. Dearnaley, J.H. Freeman, R.S. Nelson, J. Stephen, and W. Bauer. Ion implantation of metals. *Electroplating and Metal Finishing*, 29:6–8, 1976.

[146] M.J. Kim and R.W. Carpenter. TEM specimen heating during ion beam thinning: Microstructural instability. *Ultramicroscopy*, 21:327–334, 1987.

[147] T. Ishitani and H. Kaga. Calculation of local temperature rise in focused-ion-beam sample preparation. *Microscopy*, 44:331–336, 1995.

[148] J. Kempf, M. Nonnenmaeher, and H.H. Wagner. Electron and ion beam induced heating effects in solids measured by laser interferometry. *Applied Physics A*, 56:385–390, 1993.

[149] A.T. Motta. Amorphization of intermetallic compounds under irradiation - A review. *Journal of Nuclear Materials*, 244:227–250, 1997.

[150] S.X. Wang, L.M. Wang, and R.C. Ewing. Irradiation-induced amorphization: Effects of temperature, ion mass, cascade size, and dose rate. *Physical Review B*, 63:024105, 2000.

[151] S. Nagata, S. Higashi, B. Tsuchiya, K. Toh, T. Shikama, K. Takahiro, K. Ozaki, K. Kawatusra, S. Yamamoto, and A. Inouye. Ion irradiation effects on amorphization and thermal crystallization in $Zr-Al-Ni-Cu$ alloys. *Nuclear Instruments and Methods in Physics Research Section B: Beam Interactions with Materials and Atoms*, 257:420–423, 2007.

[152] M. Song, Y.Y. Sun, Y.H. He, and S.F. Guo. Structure related hardness and elastic modulus of bulk metallic glass. *Journal of Applied Physics*, 111:053518, 2012.

[153] Y. Liu, H. Bei, C.T. Liu, and E.P. George. Cooling-rate induced softening in a $Zr_{50}Cu_{50}$ bulk metallic glass. *Applied Physics Letters*, 90:071909, 2007.

[154] W.C. Oliver and G.M. Pharr. Measurement of hardness and elastic modulus by instrumented indentation: Advances in understanding and refinements to methodology. *Journal of Materials Research*, 19:3–20, 2004.

[155] C.A. Schneider, W.S. Rasband, and K.W. Eliceiri. NIH image to ImageJ: 25 years of image analysis. *Nature Methods*, 9:671, 2012.

[156] M. Sullivan and B.C. Prorok. Evaluating indent pile-up with metallic films on ceramic-like substrates. *Journal of Materials Research*, 30:2046–2054, 2015.

[157] B.X. Liu, W.S. Lai, and Q. Zhang. Irradiation induced amorphization in metallic multilayers and calculation of glass-forming ability from atomistic potential in the binary metal systems. *Materials Science and Engineering*, 29:1–48, 2000.

[158] A.C. Lund and C.A. Schuh. Critical length scales for the deformation of amorphous metals containing nanocrystals. *Philosophical Magazine Letters*, 87:603–611, 2007.

[159] A.L. Greer and I.T. Walker. Transformations in primary crystallites in $(Fe, Ni)-$ based metallic glasses. *Materials Science Forum*, 386:77–88, 2002.

[160] B.C. Wei, T.H. Zhang, W.H. Li, Y.F. Sun, Y. Yu, and Y.R. Wang. Serrated plastic flow during nanoindentation in $Nd-$ based bulk metallic glasses. *Intermetallics*, 12:1239–1243, 2004.

[161] A. Castellero, S.J. Lloyd, S.V. Madge, Z. Kovacs, J.F. Loffler, M. Baricco, and A.L. Greer. Shear-band propagation in fully amorphous and partially crystallized Mg − based alloys studied by nanoindentation and transmission electron microscopy. *Journal of Alloys and Compounds*, 434:48–51, 2007.

[162] Y. Zhang and A.L. Greer. Thickness of shear bands in metallic glasses. *Applied Physics Letters*, 89:071907, 2006.

[163] A.L. Greer, Y.Q. Cheng, and E. Ma. Shear bands in metallic glasses. *Materials Science and Engineering R*, 74:71–132, 2013.

[164] R.D. Conner, W.L. Johnson, N.E. Paton, and W.D. Nix. Shear bands and cracking of metallic glass plates in bending. *Journal of Applied Physics*, 94:904–911, 2003.

[165] W.H. Jiang, F.X. Liu, D.C. Qiao, H. Choo, and P.K. Liaw. Plastic flow in dynamic compression of a Zr − based bulk metallic glass. *Journal of Materials Research*, 21:1570–1575, 2006.

[166] J. Melngailis. Focused ion beam technology and applications. *Journal of Vacuum Science and Technology B: Microelectronics Processing and Phenomen*, 5:4469–495, 1987.

[167] G. Wang, Y.J. Huang, D. Makhanlall, and J. Shen. Friction joining of $Ti_{40}Zr_{25}Ni_3Cu_{12}Be_{20}$ bulk metallic glass. *Journal of Materials Processing Technology*, 212:1850–1855, 2012.

[168] G.M. Pharr. Measurement of mechanical properties by ultra-low load indentation. *Materials Science and Engineering A*, 253:151–159, 1998.

[169] A.A. Volinsky, J.B. Vella, and W.W. Gerberich. Fracture toughness, adhesion and mechanical properties of low − K dielectric thin films measured by nanoindentation. *Thin Solid Films*, 429:201–210, 2003.

[170] K.I. Schiffmann. Determination of fracture toughness of bulk materials and thin films by nanoindentation: Comparison of different models. *Philosophical Magazine*, 91:1163–1178, 2011.

[171] D. Casellas, J. Caro, S. Molas, J.M. Prado, and I. Valls. Fracture toughness of carbides in tool steels evaluated by nanoindentation. *Acta Materialia*, 55:4277–4286, 2007.

[172] R. Rabe, J.-M. Breguet, P. Schwallera, S. Stauss, F.-J. Haug, J. Patscheider, and J. Michler. Observation of fracture and plastic deformation during indentation and scratching inside the scanning electron microscope. *Thin Solid Films*, 469-470:206–213, 2004.

VITA

Arezoo Zare

Candidate for the Degree of

Doctor of Philosophy

Dissertation: EFFECTS OF ION IRRADIATION ON THE MICROSTRUCTURE AND MECHANICAL PROPERTIES OF TITANIUM-BASED METALLIC GLASSES

Major Field: Mechanical and Aerospace Engineering

Biographical:

Education:

Completed the requirements for the Doctor of Philosophy in Mechanical and Aerospace Engineering at Oklahoma State University, Stillwater, Oklahoma in July, 2019.

Completed the requirements for the Master of Science in Materials Engineering at Sharif University of Technology, Tehran, Iran in 2009.

Completed the requirements for the Bachelor of Science in Materials Engineering at Imam Khomeini International University, Ghazvin, Iran in 2005.

Experience:

Research/Teaching Assistant, Oklahoma State University, 2011 to Present.

Lecturer, Takestan Azad University, 2009 to 2011.

Research Assistant, Sharif University of Technology, 2006 to 2009.